



UNIVERSITÀ POLITECNICA DELLE MARCHE

FACOLTÀ DI INGEGNERIA

Corso di Laurea magistrale in Ingegneria Meccanica

**CARATTERIZZAZIONE CON METODI INVERSI DI MODELLI
ANISOTROPI DI PLASTICITÀ ATTRAVERSO PROVE DI TRAZIONE
E DIGITAL IMAGE CORRELATION**

**INVERSE IDENTIFICATION OF ANISOTROPIC YIELD FUNCTIONS
FOR SHEET METAL THROUGH TENSILE TESTING AND DIGITAL
IMAGE CORRELATION**

Relatore:

Prof. Marco Rossi

Correlatore:

Dr. Ing. Sam Coppieters

Laureando:

Andrea Martelli

A.A. 2019 / 2020

SUNTO

Oggetto di questa tesi è un progetto al quale ho lavorato durante un periodo di mobilità di cinque mesi presso il “Dipartimento di Metallurgia ed Ingegneria dei Materiali” dell’università KULeuven, in Belgio, finanziato dal progetto Erasmus+, e riguarda la «Caratterizzazione con metodi inversi di modelli anisotropi di plasticità attraverso prove di trazione e Digital Image Correlation».

La corretta identificazione del comportamento meccanico di lamiere metalliche è importante in molte applicazioni industriali, come l'automotive, principalmente per simulazioni numeriche agli elementi finiti.

Le lamiere metalliche sono prodotte attraverso laminazione a freddo, un processo che induce anisotropia influenzando il comportamento del materiale nei successivi processi di formatura.

Il problema è assicurare che il modello costitutivo utilizzato per modellare il materiale in simulazioni FEM sia in grado di descriverne il comportamento in maniera accurata. L’idea di questo lavoro è usare un modello semplice, quale l'Hill'48-r, basato sui parametri di Lankford ottenuti attraverso prove monoassiali, per simulare un particolare stato di tensione piana su un acciaio da lamiera. Hill'48-r è una funzione quadratica che lega le componenti di tensione, normalizzate rispetto alla tensione equivalente: sulla curva si trovano i punti che plasticizzano, all'interno invece i punti in campo elastico.

L'approccio tradizionale prevede il ricorso a test meccanici classici, come la prova di trazione monoassiale o di taglio puro, ottenendo distribuzioni di deformazione omogenee sul campione. Queste prove forniscono dati su tensioni e deformazioni per specifici stati tensionali, per cui sono necessari molteplici test per identificare tutti i parametri del materiale.

L'approccio alternativo consiste nel condurre test che forniscano distribuzioni di deformazione eterogenee, multiassiali, attraverso uno studio sulla topologia del campione. I vantaggi sono la riduzione del numero di test necessari, la miglior qualità e la miglior predizione dei parametri del materiale.

Il metodo utilizzato per l'identificazione si chiama FEMU e consiste nel confrontare i campi di deformazione ottenuti per via sperimentale con quelli ottenuti per via numerica (utilizzando il modello Hill). L'identificazione dei parametri si ottiene

minimizzando, attraverso l'algoritmo di Levenberg-Marquardt, una cost function definita dalla discrepanza tra risultati sperimentali e risultati numerici.

Il campione utilizzato per il test di trazione è caratterizzato dalla presenza di intagli che introducono eterogeneità nel campo di deformazione.

Il modello costitutivo del materiale implementato in Abaqus è definito dalle seguenti leggi:

- Criterio di resistenza, che esprime la relazione tra le componenti di tensione quando si verifica la plasticità: Hill'48 basato sui coefficienti di Lankford in condizioni di tensione piana;
- Regola di flusso plastico, che esprime la relazione tra tensione ed incremento di deformazione: relazione di ortogonalità;
- Legge d'incrudimento, che descrive l'evoluzione della superficie di plasticità iniziale per via della deformazione plastica: Swift.

Oltre ad un modello FEM è utilizzata la DIC, una tecnica di misurazione senza contatto che consiste nella stima di coordinate e spostamenti mediante la correlazione di una sequenza di immagini digitali della superficie del campione nell'area d'interesse, opportunamente preparata creando un pattern di macchie nere su una base bianca.

Esistono due metodi di condurre un esperimento:

- Esperimento reale (Actual Experiment, AE): il campione è deformato attraverso una macchina di trazione e durante il test vengono catturate immagini della superficie del campione nell'area d'interesse. I parametri del materiale sono ignoti;
- Esperimento virtuale (Virtual Experiment, VE): in laboratorio viene catturata un'immagine della superficie indeformata del campione che viene numericamente deformata applicando i file output di Abaqus, relativi a coordinate e spostamenti alla fine del test. I risultati del VE sono dunque ottenuti partendo da parametri del materiale noti.

È stato introdotto un indicatore quantitativo di eterogeneità, formulato considerando il range, l'eterogeneità ed il livello di deformazione ottenuti nel test. È stato condotto uno studio sull'ottimizzazione della topologia del campione cercando il valore del raggio dell'intaglio che massimizzasse l'indicatore. Il raggio ottimale è 3.5 mm, poi sono stati scelti altri due raggi, 1.5 mm e 7 mm, con valori di eterogeneità sufficientemente più

bassi. Come atteso, il 3.5 dà la miglior identificazione, dunque da qui in poi lo studio è stato concentrato su questo valore del raggio.

È stata condotta una prima identificazione con valori default dati dal software per poi valutare l'influenza di diversi parametri. È risultato che i parametri influenti sono i DIC settings, il pattern, l'orientazione del materiale.

Successivamente sono stati condotti esperimenti reali su campioni con raggi 1.5 mm, 3.5 mm e 7mm. Sono state configurate due camere, una frontale ed una angolata, per condurre la Stereo DIC, catturando immagini alla frequenza di 1 Hz. Il modulo Performance Analysis ha suggerito i valori dei settings DIC che dessero il miglior segnale e la minor risoluzione sulla base del pattern applicato.

Per il raggio 7 mm, VE e AE hanno dato risultati non validi e per niente confrontabili con quelli di riferimento, probabilmente perchè Abaqus ha problemi nel simulare l'instabilità di carico o la localizzazione. Per il raggio 1.5 mm, VE e AE hanno dato risultati validi e coerenti anche se lontani da quelli del modello teorico, per via del basso livello di eterogeneità raggiunto. Per il raggio 3.5 mm i risultati sono ottimi, soprattutto se si utilizzano 2 Load Steps o se si ricorre ad un VE.

Da un'analisi degli stati tensionali e di deformazione, si nota che i punti sono localizzati nella regione prossima agli stati di trazione monoassiale e di deformazione piana.

Si possono dunque trarre le seguenti conclusioni:

- Maggiore è il livello di eterogeneità, migliore è l'identificazione;
- L'identificazione è sensibile al numero di Load Steps ed alle impostazioni DIC, le quali sono strettamente dipendenti dal speckle pattern;
- Si evidenzia una coerenza tra i risultati da VE e AE, per cui è possibile condurre esperimenti realistici per via numerica in alternativa agli esperimenti reali condotti in laboratorio, risparmiando in termini di tempi e costi.
- Per questo specifico test, il modello Hill'48-r descrive accuratamente il comportamento del materiale in prossimità degli stati di tensione monoassiale e di deformazione piana.

Sulla base di queste considerazioni, ulteriori studi potranno essere condotti in futuro, ricorrendo a test su campioni con forme diverse e più complesse.

List of figures

Figure 1.1 - Element subjected to uniaxial tension and principal directions	3
Figure 1.2 - Principal stresses and strains in uniaxial tension (a) and general plane stress sheet (b) process	5
Figure 1.3 - Von Mises yield surface in the stress space	7
Figure 1.4 - Orthotropy axes of the rolled sheet metals: rolling direction (RD), transversal direction (TD) and normal direction (ND)	8
Figure 1.5 - Tensile specimen prelevated at the angle ϑ (measured from the rolling direction).....	8
Figure 1.6 - Example of Hill48 loci for different strain levels.....	11
Figure 1.7 - Yield surface.....	13
Figure 1.8 - Strain increment components for different stress states around the von Mises yield locus.....	13
Figure 1.9 - Strain diagram shows the different deformation modes corresponding to different strain ratios. (A) Equibiaxial stretching. (B) Deformation in plane strain. (C) Uniaxial extension. (D) Pure shear. (E) Uniaxial compression.	14
Figure 1.10 - Uniform deformation of part of a continuous sheet in a plane stress proportional process	15
Figure 1.11 - Uniaxial stress-strain curve along the rolling direction (RD). The SWIFT curve is formulated by minimizing the variance with the experimental TRUE curve.	17

Figure 2.1 - Principle of the FEMU method	19
Figure 2.2 – Cost function varying with a defined parameter	20
Figure 2.3 - Calibration target.....	21
Figure 2.4 - Specimen with manually applied speckle pattern in the AOI	22
Figure 2.5 - Image of the AOI grabbed with a frontal DIC camera.....	23
Figure 2.6 - Subset, area/region-of-interest (AOI/ROI), speckle pattern.....	23
Figure 2.7 - A subset in the reference image is tracked in the deformed image and the displacement vector of the integration point is retrieved	24
Figure 2.8 - Procedure for strain derivation	27
Figure 2.9 - Working principle for the Gauss-Newton method for one dimensional case. The solid black line represents the real cost function $C(p)$, the red dashed line represents the Taylor series approximation $Ck(p)$	30
Figure 2.10 - Comparisons of the centred, forward and backward finite differentiation approximation schemes	33
Figure 2.11 - Principle of the combined Gauss-Newton and Levenberg-Marquardt algorithms.....	34
Figure 2.12 - Flowchart of material identification using AE.....	35
Figure 2.13 – Digital images of the AOI using Stereo-DIC	36
Figure 2.14 - Flowchart of material identification using AE.....	36
Figure 2.15 - Numerical deformation and correlation	37

Figure 2.16 – Displacement fields and strain fields from VE.....	37
Figure 2.17 - Coordinate transformation in MatchID and strain fields computation approach in FEMid.....	38
Figure 3.1 - FE model with material orientation and dimensions of the AOI. Dimension of the radius of the notches: 3.5 mm.....	39
Figure 3.2 - Heterogeneous strain distribution in the AOI. Dimension of the radius of the notches: 3.5 mm	40
Figure 3.3 - Stress distribution in the AOI using the Hill'48. Dimension of the radius of the notches: 3.5 mm.....	41
Figure 3.4 - Strain state for a specimen with 3.5 mm radius	42
Figure 3.5 – Strain field in the AOI	47
Figure 3.6 - Distribution of ε_{MAXp} as function of the radius of the notches.....	48
Figure 3.7 - Distribution of $Av_{\varepsilon p}$ as a function of the radius	48
Figure 3.8 – Strain fields for radii a) 1.5 mm, b) 3.5mm, c) 7 mm.....	49
Figure 3.9 - Distribution of $(\varepsilon_2/\varepsilon_1)_R$ as a function of the radius	49
Figure 3.10 - Distribution of $Std(\varepsilon_p)$ as a function of the radius	50
Figure 3.11 - Distribution of $Std(\varepsilon_2/\varepsilon_1)$ as a function of the radius.....	50
Figure 3.12 – Trend of I_T as a function of the radius	51

Figure 3.13 - Histograms showing the number of elements subjected to the same value of plastic strain with radius of the notch (a) 1.5 mm, (b) 3.5 mm, (c) 7 mm.....	52
Figure 3.14 - Histograms showing the number of elements subjected to the same strain state with radius of the notch of (a) 1.5 mm, (b) 3.5 mm, (c) 7 mm.....	53
Figure 3.15 - Strain states of a specimen with a radius of the notch of (a) 1.5 mm, (b) 3.5 mm and (c) 7 mm	54
Figure 3.16 - Strain states of a specimen with a radius of the notch of (a) 1.5 mm, (b) 3.5 mm and (c) 7 mm	55
Figure 3.17 - Flow chart of the topology optimizer functioning for minimum static compliance design.....	57
Figure 4.1 - FE model: shape of the specimen, AOI, mesh, material orientation, boundary conditions (clamping and load).....	64
Figure 4.2 – Specimens with three different radii: 1.5 mm, 3.5 mm, 7 mm	64
Figure 4.3 – Digital image of the AOI with a 5 pixels average speckle size.....	65
Figure 4.4 – Hill’48 loci: model (black), identified (blue)	66
Figure 4.5 – Hill loci with four different VSG values	67
Figure 4.6 – Hill loci without noise and with noise included in the numerical deformation	68
Figure 4.7 - Hill loci using 1 LS or 4 LS	68
Figure 4.8 – Hill loci from 2D-DIC and 3D-DIC	69
Figure 4.9 - Digital images of the AOI with a 5 and a 3 pixels average speckle size	69

Figure 4.10 – Hill loci using different speckle patterns	70
Figure 4.11 – Hill loci with different material orientation.....	71
Figure 4.12 – Preparation of the specimens: creation of the speckle pattern.....	72
Figure 4.13 – Camera set-up: front and angled cameras.....	72
Figure 4.14 - Experimental set-up: DIC system and signals received	73
Figure 4.15 - Tensile load-time curves	73
Figure 4.16 – Specimens at the end of the tests: different strain distribution are noticeable for the three radii. a) 1.5 mm b) 3.5 mm c) 7 mm.	74
Figure 4.17 - Creation of the speckle pattern on the AOI.....	76
Figure 4.18 - Displacement and strain fields of the specimen obtained using DIC...	77
Figure 4.19 - Experimental and numerical strain fields for the 1.5 mm radius (AE)	78
Figure 4.20 – Hill loci for the 1.5 mm radius (AE and VE)	78
Figure 4.21 - Experimental and numerical strain fields for the 7 mm radius (AE) ...	79
Figure 4.22 - Experimental and numerical strain fields for the 3.5 mm radius (AE)	80
Figure 4.23 – Hill loci for the 3.5 mm radius (AE_2LS).....	80
Figure 4.24 - Experimental and numerical strain fields for the 3.5 mm radius (VE)	80
Figure 4.25 - Hill loci for the 3.5 mm radius (VE)	81
Figure 4.26 – Stress loci for the 1.5 mm radius	82

Figure 4.27 - Stress loci for the 3.5 mm radius..... 83

Figure 4.28 - Stress loci for the 7 mm radius..... 83

List of tables

Table 1 - Chemical composition test material.....	16
Table 2 - Lankford parameters retrieved from classical tests	17
Table 3 - Swift's hardening law fitted in a range from $e_{q^{pl}} = 0,01$ up to $e_{q^{pl}} = 0,25$...	17
Table 4 - Relative weighting factors for 50-50, 65-35 and 35-65 importance for strain range/heterogeneity and strain level for I_T calculation	46
Table 5 - Absolute weighting factors for I_T calculation.....	46
Table 6 – Inversely identified r-values for the three radii.....	65
Table 7 - Calibration parameters related to camera 0 and camera 1	75
Table 8 - Relative positions between camera 0 and camera 1	75
Table 9 – Performance Analysis	77
Table 10 - Optimal DIC settings from the PA	77
Table 11 - Identified r-values for the 1.5 mm radius: AE and VE.....	78
Table 12 - Identified r-values for the 7 mm radius: AE and VE.....	79
Table 13 - Identified r-values for the 3.5 mm radius: AE and VE.....	79

List of abbreviations

AOI	Area Of Interest
AE	Actual Experiment
BESO	Evolutionary Structural Optimization Method
CEGM	Constitutive Equation Gap Method
DIC	Digital Image Correlation
DOF	Depth Of Field
EGM	Equilibrium Gap Method
FE	Finite Element
FEA	Finite Element Analysis
FEMU	Finite Element Model Updating
LSM	Level Set Method
NSSD	Normalized Sum of Squared Differences
PA	Performance Analysis
PVW	Principle of Virtual Work
QOIs	Quantities Of Interest
RD	Rolling Direction

RGM	Reciprocity Gap Method
ROI	Region-Of-Interest
SBVFs	Sensitivity-Based Virtual Fields
SIMP	Solid Isotropic Material with Penalization
SSD	Sum of Squared Differences
TD	Transverse Direction
TO	Topology Optimization
VE	Virtual Experiment
ZNSSD	Zero Normalized Sum of Squared Differences

List of symbols

l	length
w	width
t	thickness
dl	length increment
dw	width increment
dt	thickness increment
$d\varepsilon_1, d\varepsilon_2, d\varepsilon_3$	principal strains increment
$\varepsilon_1, \varepsilon_2, \varepsilon_3$	principal strains
$\sigma_1, \sigma_2, \sigma_3$	principal stresses
β	strain ratio
α	stress ratio
r	Lankford parameter
r_n	normal anisotropy
Δr	planar anisotropy
F, G, H, L, M, N	Hill48 coefficients
X	yield stress along x direction

Y	yield stress along y direction
Z	yield stress along z direction
r_0	Lankford parameter in the rolling direction
r_{45}	Lankford parameter along the 45° direction
r_{90}	Lankford parameter in the transverse direction
σ_{11}	local stress along the rolling direction
σ_{22}	local stress along the transverse direction
$\sigma_{12}, \sigma_{13}, \sigma_{23}$	shear stresses
σ_0	yield stress along the rolling direction
σ_{90}	yield stress along the transverse direction
K	strength coefficient
n	strain hardening exponent
ε_0	initial deformation
ε_{eq}^{pl}	equivalent plastic strain
X', X''	second order tensors
$L_{11}', L_{12}', L_{21}', L_{22}', L_{66}'$	coefficients of the Yld2000–2d linear transformation

g	plastic potential
F, f	yield function
T_1, T_2	principal tensions
u	displacement along x direction
v	displacement along y direction
f	grey level in the undeformed configuration
g	grey level in the deformed configuration
S	sensitivity matrix
S_{ij}	sensitivity coefficients
ε_i^{exp}	column vector of experimentally measured strains
ε_i^{num}	column vector of numerically measured strains
F_i^{exp}	column vector of experimentally measured tensile forces
F_i^{num}	column vector of numerically computed tensile forces
C	cost function in FEMU
p	material parameters in VFM

W_{ij}^r	weight diagonal matrix
ξ_c	convergence value related to the cost function
ξ_p	convergence value related to the material parameters
v_i	element volume
v_T	total volume of the specimen
$\mu_{\varepsilon_2/\varepsilon_1}$	average value of strain states
μ_{ε_p}	average value of plastic strains
ε_{max}^p	maximum plastic deformation
Av_{ε_p}	average plastic deformation
$Std(\varepsilon^P)$	standard deviation of equivalent plastic strains
$Std(\varepsilon_2/\varepsilon_1)$	standard deviation of strain states
$(\varepsilon_2/\varepsilon_1)_R$	maximum strain state range
w_r	relative weighting factors
w_a	absolute weighting factors
I_T	heterogeneity/strain range and strain level indicator
R	radius

k	element stiffness matrix
K	global stiffness matrix
ρ_e	element relative density
$\{F\}$	vector of nodal loads
$\{U\}$	vector of nodal displacements
$[B]$	displacement differentiation matrix
m	positive move-limit
η	damping coefficient
λ	Lagrangian multiplier
B_e	updating parameter
$[d]$	matrix of relative densities
$[D]$	elastic stress-strain matrix
$[D_p]$	plastic stress-strain matrix
ε_x	strain along x direction
ε_y	strain along y direction
γ_{xy}	shear strain
V	voltage

σ	Cauchy stress tensor
u^*	virtual displacement
$\partial u^*/\partial x$	virtual strain
F	deformation gradient
T	first Piola-Kirchhoff stress tensor
n	normal vector in the deformed configuration
N	normal vector in the reference configuration
B_T	body in the current configuration
B_0	body in the reference configuration
∂B_T	boundary in the current configuration
∂B_0	boundary in the reference configuration
ε_L	Hencky strain
W_{int}	virtual internal work
W_{ext}	virtual external work
χ	material parameters in VFM
Δt	time interval
\mathcal{S}	surface of the area of the j-th point

Table of contents

List of figures	iv
List of tables	x
List of abbreviations.....	xi
List of symbols.....	xiii
Introduction	1
Metal plasticity	3
1.1 Sheet deformation processes	3
1.2 Yield criteria.....	5
1.2.1 Huber-Mises-Hencky Yield Criterion for isotropic materials	6
1.2.2 Anisotropy of sheet metals.....	7
1.3 Flow rule	12
1.4 Load instability	14
1.5 DC04	16
General framework of FEMU	18
2.1 Basic principles of inverse modelling.....	18
2.2 Digital Image Correlation technique.....	20
2.3 Cost function	27
2.4 Actual Experiment and Virtual Experiment.....	35
2.4.1 Actual Experiment	35
2.4.2 Virtual Experiment.....	36
Design of heterogeneous experiments	39
3.1 Evaluation of heterogeneity	39
3.1.1 Stress state.....	39
3.1.2 Strain state.....	41

3.2 Definition of an indicator for heterogeneity assessment.....	43
3.2.1 Definition of I_T	43
3.2.2 Application of I_T to specimen with notches	46
3.3 Topology Optimization	55
3.3.1 Definition and applications	55
3.3.2 Topology Optimization applied to IT indicator	58
3.3.3 I_T indicator applied to the specimen with notches	61
Inverse identification of anisotropic yield functions using a tensile test and DIC.....	63
4.1 FE Model.....	63
4.3 Material identification using a AE	71
4.3.1 Digital Image Correlation	75
4.3.2 Results	78
4.4 Stress states	81
Conclusions	84
Bibliography.....	85

Introduction

The subject of this thesis is a project on which I worked during a mobility period of five months at the "Department of Metallurgy and Materials Engineering" of the KULeuven University, in Belgium, funded by the Erasmus + project, and concerns the "Inverse identification of anisotropic yield functions for sheet metal through tensile testing and Digital Image Correlation".

Correct identification of the mechanical behavior of metal sheets is important in many industrial applications, such as automotive, mainly for numerical finite element simulations.

Metal sheets are produced through cold rolling, a process that induces anisotropy, influencing the behavior of the material in subsequent forming processes.

The problem is to ensure that the material constitutive model used in FEM simulations is able to describe its behavior accurately.

In this work the idea is to use a simple model, such as Hill'48-r, based on Lankford parameters obtained through uniaxial tests, to simulate a particular plane stress state on a sheet steel. Hill'48-r is a quadratic function that links the tension components, normalized with respect to the equivalent tension: on the curve there are the plasticized points, while the internal region corresponds to the elastic domain.

The traditional approach for material characterization involves the use of classical mechanical tests, such as uniaxial or pure shear tensile test, obtaining homogeneous strain distributions on the sample. These give stress and strain data for specific stress states, so multiple tests are required to identify all the material parameters.

The alternative approach is to conduct tests that provide heterogeneous, multiaxial strain distributions involving the whole set of constitutive parameters. The advantages are the reduction of the number of tests required, a better quality and a better prediction of the material parameters.

The method used for identification is called FEMU and consists in comparing the experimental strain fields with the numerical strain fields (obtained using the Hill model). The identification of the parameters is obtained by minimizing, through the Levenberg-Marquardt algorithm, a cost function defined by the discrepancy between experimental and numerical results.

A tensile test on a specific specimen is used to inversely identify the material parameters. Abaqus and the Digital Image Correlation (DIC) technique are used to simulate the test and to measure the displacement fields, respectively. DIC is a non-contact measurement technique that consists in the estimation of coordinates and displacements by correlating a sequence of digital images of the sample surface in the area of interest, properly prepared by creating a pattern of black speckles on a white base.

The chapters composing this work are briefly summarized as follows:

- Chapter 1 proposes an insight in metal plasticity, and the elements required to describe the material plastic behavior are discussed: yield criterion, flow rule, hardening law.
- In Chapter 2 the fundamental elements necessary for FEMU are reported. The background of the Digital Image Correlation technique is presented and the cost function for inverse identification, describing the discrepancy between the experimental and the numerical data and based on the Gauss-Newton and Levenberg-Marquardt algorithms, is mathematically analyzed. Finally, the difference between Actual Experiment (AE) and Virtual Experiment (VE) is explained.
- Chapter 3 describes the specimen used in the test, characterized by notches that introduce a level of heterogeneity visible through the graphs of the stress and strain states. The general principles of Topology Optimization are defined, and a quantitative indicator of heterogeneity is introduced, applied to the specimen in question, in order to identify its trend as the radius of the notches varies.
- Chapter 4 analyzes, through a Virtual Experiment on the optimal shape, the influence of a series of parameters, in particular the DIC settings, the speckle pattern and the orientation of the material, on the identification. Finally, Actual Experiments were conducted in the laboratory on specimens with three previously selected radii to evaluate the effects on the identification of the material.

Chapter 1

Metal plasticity

1.1 Sheet deformation processes

The most important criteria in selecting a material are related to its properties, such as strength, density, stiffness and corrosion resistance. For sheet material, the capability to be shaped in a given process, called formability, is one of the main characteristics to be considered. In order to assess formability, it is necessary to describe the material behavior in a precise way, through mathematical forms, which can be derived from mechanical tests. In sheet metal forming, there are mainly two regimes of interest: elastic and plastic behavior. Forming a sheet leads to a permanent plastic flow, which usually causes quite large strains. On the other hand, the elastic strains are very small, and therefore, often neglected. However, they can have an important effect when forming loads are removed, leading to elastic shape changes, or ‘springback’.

A common feature of many sheet forming processes is that the stress perpendicular to the surface of the sheet metal is small, compared with the stresses in the plane of the sheet, i.e., membrane stresses. If the normal stress is assumed equal to zero, the process occurs in a plane stress condition [1].

The tensile test is, as a matter of fact, a plane stress process up to the point of maximum force. An element subjected to uniaxial tension is below considered (Figure 1.1). Up to maximum load, the deformation is uniform. There is no shear hence, the directions 1, 2 and 3, which are respectively the directions along the axis, across the width and through the thickness, are principal directions.

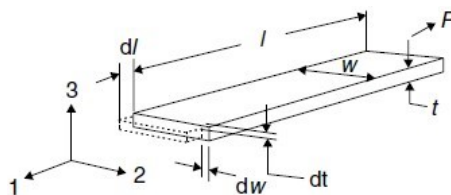


Figure 1.1 - Element subjected to uniaxial tension and principal directions

During any small part of the process, the principal strain increment along the tensile axis is:

$$d\varepsilon_1 = \frac{dl}{l} \quad (1.1.a)$$

Similarly, along the width and thickness directions the strain increments are respectively:

$$d\varepsilon_2 = \frac{dw}{w} \quad \text{and} \quad d\varepsilon_3 = \frac{dt}{t} \quad (1.1b)$$

Plastic deformation occurs at constant volume, so the differential of the volume will be zero, i.e.:

$$dV = d(lwt) = dl \times wt + dw \times lt + dt \times lw = 0 \quad (1.2)$$

and, dividing by lwt :

$$\frac{dl}{l} + \frac{dw}{w} + \frac{dt}{t} = 0 \quad (1.3)$$

i.e.

$$d_1 + d_2 + d_3 = 0 \quad (1.4)$$

This means that by supposing constant volume deformation, the sum of the principal strain increments is equal to zero.

If the analysis is restricted to isotropic materials, with identical properties measured in all directions, it is feasible to assume the strains in the width and thickness directions will be equal in magnitude, thus:

$$d\varepsilon_2 = d\varepsilon_3 = -\frac{1}{2}d\varepsilon_1 \quad (1.5)$$

In contrast with the tensile test in which two of the principal stresses are zero, in a typical sheet process, most elements deform under membrane stress σ_1 and σ_2 , which are both different from zero (Figure 1.2). The stress σ_3 perpendicular to the surface of the sheet, as discussed before, is generally very small compared to the membrane stresses, and therefore, assumed equal to zero. With this assumption, it is possible to develop a simple and sufficiently accurate theory of plastic deformation for metal sheet. It is convenient to describe the deformation of an element in the terms of either the strain ratio β or stress ratio α .

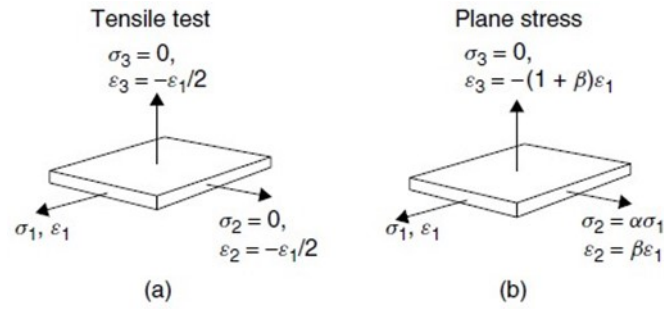


Figure 1.2 - Principal stresses and strains in uniaxial tension (a) and general plane stress sheet (b) process

The process is assumed proportional thus the ratios will remain constant. According to the usual convention, the principal directions are defined so that $\sigma_1 > \sigma_2$ and the third direction is perpendicular to the surface where $\sigma_3 = 0$. The deformation process can consequently be described by the following relations:

$$\varepsilon_1; \quad \varepsilon_2 = \beta \varepsilon_1; \quad \varepsilon_3 = -(1 + \beta)\varepsilon_1 \quad (1.6a)$$

$$\sigma_1; \quad \sigma_2 = \alpha \sigma_1; \quad \sigma_3 = 0 \quad (1.6b)$$

The third principal strain is obtained using the constant volume condition, which by integration can be expressed in terms of natural strains:

$$\varepsilon_1 + \varepsilon_2 + \varepsilon_3 = 0 \quad (1.7)$$

In case of uniaxial tension, the strain and stress ratios are $\beta = -1/2$ and $\alpha = 0$.

In order to describe the plastic material behavior, three elements are needed [1]:

- A yield criterion which expresses the relationship between the stress components when plastic deformation occurs;
- A flow rule expressing the relationship between stress and strain rate;
- A hardening law which describes the evolution of the initial yield surface due to plastic deformation.

1.2 Yield criteria

The transition from the elastic to the plastic regime occurs when the stress reaches the yield point of the material. The yield point, in case of uniaxial tension, can be easily determined using the stress-strain curve.

However, for multiaxial stress states, a relationship between principal stresses (or local stresses) is required to specify the conditions which cause plastic flow:

$$F(\sigma_1, \sigma_2, \sigma_3, \sigma_y) = 0 \quad (1.8)$$

where σ_1 , σ_2 and σ_3 are the principal stresses (or local stresses) and σ_y is the yield stress which is usually expressed as a function of the equivalent plastic strain ε_{eq}^{pl} . The yield functions can be obtained from calculus based on the crystallographic structure of the material or by approximating experimental data with an analytical function. In the latter case, they are called phenomenological yield functions and they are described by a simpler mathematical form, hence, easier to be manipulated and implemented in finite element codes in comparison to the ones based on the crystallographic texture [2]. Furthermore, they can be generalized to describe the anisotropic behavior of the materials. In this study, the yield surface and the hardening behavior are both expressed by phenomenological models since they are easy to use in the finite element analysis (FEA).

1.2.1 Huber-Mises-Hencky Yield Criterion for isotropic materials

The criterion is based on the observation according to which hydrostatic pressure cannot cause plastic yielding and that only elastic energy of distortion influences the transition from elastic to plastic behavior [3]. The elastic potential energy Wp has two components: the volumetric change energy Wv and the distortion energy, Wf :

$$Wp = Wv + Wf \quad (1.9)$$

hence, Wf can be written as:

$$Wf = Wp - Wv \quad (1.10)$$

By replacing the expressions of elastic potential energy and distortion energy, the relation becomes:

$$Wf = \frac{1 + \mu}{6E} [(\sigma_1 - \sigma_2)^2 + (\sigma_2 - \sigma_3)^2 + (\sigma_3 - \sigma_1)^2] \quad (1.11)$$

In case of uniaxial tension ($\sigma_2 = \sigma_3 = 0$) yielding occurs when the tensile stress reaches the yield stress, $\sigma_1 = \sigma_y$ along direction 1. Consequently, the critical value of the distortion energy, which causes the material passing from the elastic to the plastic state is:

$$Wf = \frac{1 + \mu}{6E} 2\sigma_y^2 \quad (1.12)$$

Equating Equations (1.11) and (1.12) the von Mises criterion can be written in the form:

$$(\sigma_1 - \sigma_2)^2 + (\sigma_2 - \sigma_3)^2 + (\sigma_3 - \sigma_1)^2 = 2\sigma_y^2 \quad (1.13)$$

Equation (1.13) represents the mathematical description of a surface in the three-dimensional space of the principal stresses. Only for the von Mises criterion it is a circular cylinder as shown in Figure 1.3.

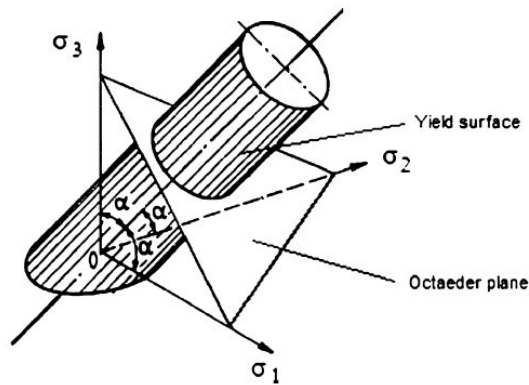


Figure 1.3 - Von Mises yield surface in the stress space

In plane stress conditions ($\sigma_3 = 0$) the yield surface reduces to a curve in a reference system where only σ_1 and σ_2 appear. Therefore, Equation (1.13) can be rewritten as:

$$\sigma_1^2 + \sigma_2^2 - \sigma_1\sigma_2 = \sigma_y^2 \quad (1.14)$$

1.2.2 Anisotropy of sheet metals

1.2.2.1 Uniaxial tension

Because of the crystallographic structure and the characteristics of the rolling process, sheet metals are often characterized by a significant anisotropy of mechanical properties. As a matter of fact, the rolling process induces a particular anisotropy characterized by the symmetry of the mechanical properties with respect to three orthogonal planes, leading to the so-called plastically orthotropic behavior [3]. The intersection lines of these planes are the orthotropy axes, which in case of rolled sheet metals are Rolling Direction (RD), Transverse Direction (TD) and Normal Direction (ND), as shown in Figure 1.4.

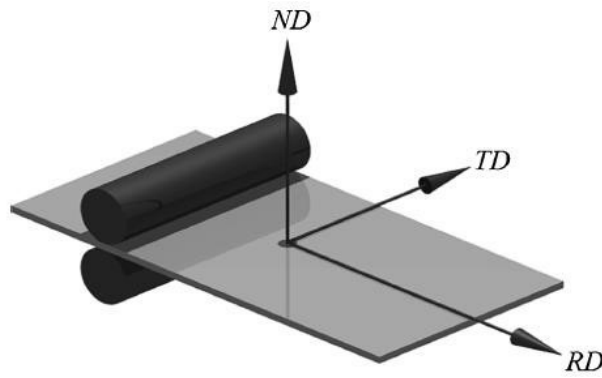


Figure 1.4 - Orthotropy axes of the rolled sheet metals: rolling direction (RD), transversal direction (TD) and normal direction (ND)

The variation of the plastic behavior with respect to the material directions is quantified by the Lankford parameter. This coefficient is determined by means of tensile tests on sheet specimens (Fig. 1.5).

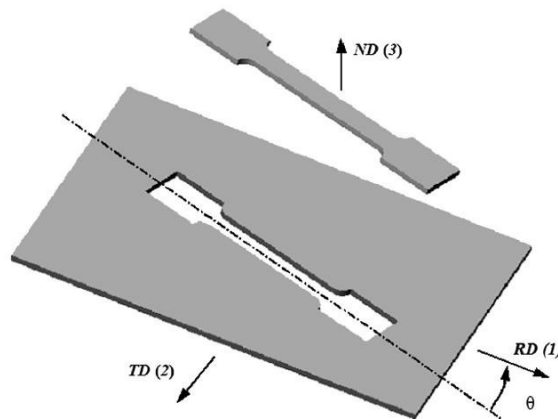


Figure 1.5 - Tensile specimen prelevated at the angle ϑ (measured from the rolling direction)

The Lankford parameter is defined as:

$$r = \frac{\varepsilon_2}{\varepsilon_3} \quad (1.15)$$

where ε_2 and ε_3 are the strains in the width and thickness directions, respectively. For an isotropic material the strains are the same along the two directions and the coefficient is equal to one. Generally, tensile tests are conducted in order to find the r -values along 0° , 45° and 90° directions with respect to the Rolling Direction. The average of the r -values obtained along the directions previously mentioned in the plane of the sheet metal results in the coefficient of normal anisotropy r_n , which is determined by:

$$r_n = \frac{r_0 + 2r_{45} + r_{90}}{4} \quad (1.16)$$

The variation of normal anisotropy with the angle to the Rolling Direction can be measured as:

$$\Delta r = \frac{r_0 + r_{90} - 2r_{45}}{2} \quad (1.17)$$

and it is known as planar anisotropy.

1.2.2.2 Hill'48 Yield Criterion

In 1948 Hill proposed an anisotropic yield criterion as an extension of the Huber-Mises-Hencky criterion. The material is supposed to have an anisotropy with three orthogonal symmetry planes. The yield surface is described by a quadratic function:

$$2f(\sigma_{ij}) = F(\sigma_{22} - \sigma_{11})^2 + G(\sigma_{33} - \sigma_{11})^2 + H(\sigma_{11} - \sigma_{22})^2 + 2L\sigma_{23}^2 + 2M\sigma_{31}^2 + 2N\sigma_{12}^2 = 1 \quad (1.18)$$

f is the yield function; F , G , H , L , M and N are constants specific to the anisotropy state of the material. The expression for f only has this form when the principal axes of anisotropy are chosen as axes of reference, otherwise the stress components have to be transformed. If X , Y and Z are the tensile yield stresses in the principal anisotropic directions, the coefficients F , G and H are obtained as functions of the uniaxial yield stresses:

$$\begin{cases} \frac{1}{X^2} = G + H & 2F = \frac{1}{Y^2} + \frac{1}{Z^2} - \frac{1}{X^2} \\ \frac{1}{Y^2} = H + F & 2G = \frac{1}{Z^2} + \frac{1}{X^2} - \frac{1}{Y^2} \\ \frac{1}{Z^2} = F + G & 2H = \frac{1}{X^2} + \frac{1}{Y^2} - \frac{1}{Z^2} \end{cases} \quad (1.19)$$

If R , S , T are the yield stresses in shear with respect to the principal axes of anisotropy, then:

$$2L = \frac{1}{R^2}, \quad 2M = \frac{1}{S^2}, \quad 2N = \frac{1}{T^2} \quad (1.20)$$

To describe completely the state of anisotropy in an element the six independent yield stresses X , Y , Z , R , S and T need to be given.

The yield criterion can be interpreted as a surface in a six-dimensional space of the stress components. The points inside the surface represent the elastic states of the material, while the points located in the surface correspond to the plastic state [4].

In case of plane stress ($\sigma_{33} = \sigma_{31} = \sigma_{23} = 0$; $\sigma_{11} \neq 0$; $\sigma_{22} \neq 0$; $\sigma_{12} \neq 0$), the yield criterion becomes:

$$2f(\sigma_{ij}) = (G + H)\sigma_{11}^2 - 2H\sigma_{11}\sigma_{22} + (H + F)\sigma_{22}^2 + 2N\sigma_{12}^2 = 1 \quad (1.21)$$

The relations between the anisotropy coefficients (r_0, r_{45}, r_{90}) and the coefficients F, G, H and N may be easily obtained from the flow rule associated to the yield function:

$$r_0 = \frac{H}{G} \quad r_{90} = \frac{H}{F} \quad r_{45} = \frac{N}{F + G} - \frac{1}{2} \quad N = (F + G) \left(r_{45} + \frac{1}{2} \right) \quad (1.22)$$

The yield stresses in the directions of the principal anisotropic axes are denoted as $X = \sigma_0$ and $Y = \sigma_{90}$. It can be shown that the following relation between yield stresses and anisotropy coefficients is valid:

$$\frac{\sigma_0}{\sigma_{90}} = \sqrt{\frac{r_0(1 + r_{90})}{r_{90}(1 + r_0)}} \quad (1.23)$$

By replacing Equations (1.22) and (1.23) in Equation (1.21), the yield criterion for plane stress can be rewritten as:

$$\sigma_1^2 - \frac{2r_0}{1 + r_0} \sigma_1 \sigma_2 + \frac{r_0(1 + r_{90})}{r_{90}(1 + r_0)} \sigma_2^2 + \frac{r_0 + r_{90}}{r_{90}(1 + r_0)} (2r_{45} + 1) \sigma_{12}^2 = \sigma_0^2 \quad (1.24)$$

If the principal directions of the stress tensor are coincident with anisotropic axes ($\sigma_{12} = 0$), the Hill'48 criterion can be written in the form:

$$\sigma_1^2 - \frac{2r_0}{1 + r_0} \sigma_1 \sigma_2 + \frac{r_0(1 + r_{90})}{r_{90}(1 + r_0)} \sigma_2^2 = \sigma_0^2 \quad (1.25)$$

Equation (1.25) geometrically represents families of ellipses depending on the parameters r_0 and r_{90} [3]. The yield stress σ_0 defines the size of the yield surface (Figure 1.6), since it depends on the equivalent plastic strain through the hardening law.

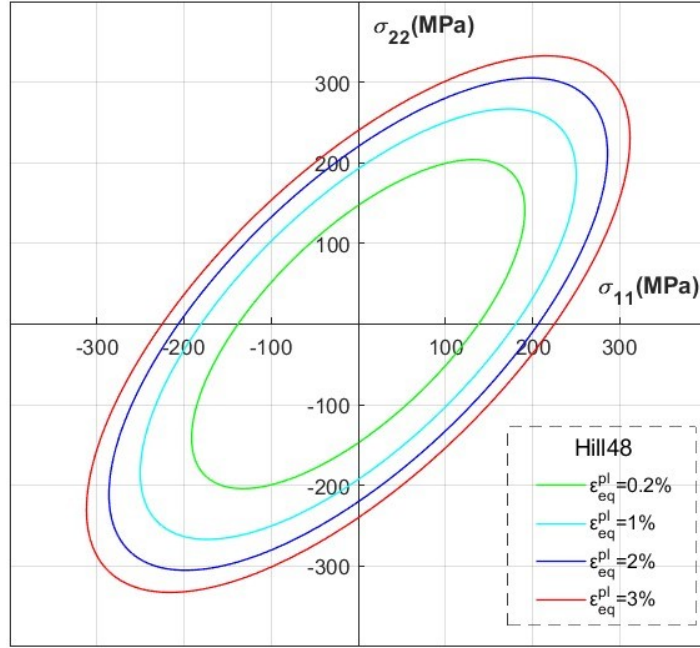


Figure 1.6 - Example of Hill48 loci for different strain levels

From the graph above it can be inferred that, by using the same Hill'48 coefficients for different strain levels, the changing of the material behavior is assumed isotropic. In the present study, the phenomenological hardening law used is the Swift's model:

$$\sigma_0 = K(\varepsilon_0 + \varepsilon_{eq}^{pl})^n \quad (1.26)$$

where K is the deformation resistance, ε_0 the initial deformation and n the hardening exponent.

1.2.2.3 Yld2000-2d Yield Criterion

The Yld2000-2d yield criterion is a plane stress yield function that well describes the anisotropic behavior of sheet metals [6,7]. It is characterized by two linear transformations on the Cauchy stress tensor and it is defined as:

$$|X'_1 - X'_2|^M + |2X''_2 + X''_1|^M + |2X''_1 + X''_2|^M = 2\bar{\sigma}^M \quad (1.27)$$

with $\bar{\sigma}$ the equivalent stress. The principal values X'_i and X''_i of the second order tensors X' and X'' are given as:

$$X'_i = \frac{1}{2} \left(X'_{xx} + X'_{yy} \pm \sqrt{(X'_{xx} - X'_{yy})^2 + 4X'^2_{xy}} \right) \quad (1.28)$$

$$X_i'' = \frac{1}{2} \left(X_{xx}'' + X_{yy}'' \pm \sqrt{(X_{xx}'' - X_{yy}'')^2 + 4X_{xy}''^2} \right) \quad (1.29)$$

The second order tensors X' and X'' are the result of a linear transformation of the Cauchy stress σ :

$$\begin{bmatrix} X'_{11} \\ X'_{22} \\ X'_{12} \end{bmatrix} = \begin{bmatrix} L'_{11} & L'_{12} & 0 \\ L'_{21} & L'_{22} & 0 \\ 0 & 0 & L'_{66} \end{bmatrix} \begin{bmatrix} \sigma_{11} \\ \sigma_{22} \\ \sigma_{12} \end{bmatrix}, \quad \begin{bmatrix} X''_{11} \\ X''_{22} \\ X''_{12} \end{bmatrix} = \begin{bmatrix} L''_{11} & L''_{12} & 0 \\ L''_{21} & L''_{22} & 0 \\ 0 & 0 & L''_{66} \end{bmatrix} \begin{bmatrix} \sigma_{11} \\ \sigma_{22} \\ \sigma_{12} \end{bmatrix} \quad (1.30)$$

$$\begin{bmatrix} L'_{11} \\ L'_{12} \\ L'_{21} \\ L'_{22} \\ L'_{66} \end{bmatrix} = \begin{bmatrix} \frac{2}{3} & 0 & 0 \\ -\frac{1}{3} & 0 & 0 \\ 0 & -\frac{1}{3} & 0 \\ 0 & \frac{2}{3} & 0 \\ 0 & 0 & 0 \end{bmatrix} \begin{bmatrix} \alpha_1 \\ \alpha_2 \\ \alpha_7 \end{bmatrix}, \quad \begin{bmatrix} L''_{11} \\ L''_{12} \\ L''_{21} \\ L''_{22} \\ L''_{66} \end{bmatrix} = \begin{bmatrix} -2 & 2 & 8 & -2 & 0 \\ 1 & -4 & -4 & 4 & 0 \\ 4 & -4 & -4 & 1 & 0 \\ -2 & 8 & 2 & -2 & 0 \\ 0 & 0 & 0 & 0 & 9 \end{bmatrix} \begin{bmatrix} \alpha_3 \\ \alpha_4 \\ \alpha_5 \\ \alpha_6 \\ \alpha_8 \end{bmatrix} \quad (1.31)$$

The mentioned yield criteria will be used in Chapter 4 to conduct the virtual experiment.

1.3 Flow rule

A wide class of material behavior can be modelled using the general form:

$$d\varepsilon_{ij}^p = d\lambda \frac{\partial g}{\partial \sigma_{ij}} \quad (1.32)$$

where g is a scalar function called plastic potential that, when differentiated with respect to the stresses, gives the plastic strains. The flow rule mentioned before is called a non-associated flow rule. By considering a sub-class of materials whose plastic potential is the yield function $g=f$:

$$d\varepsilon_{ij}^p = d\lambda \frac{\partial f}{\partial \sigma_{ij}} \quad (1.33)$$

On the contrary, this flow rule is called associated flow rule due to the fact that the flow is associated with a particular yield criterion.

The yield surface $f(\sigma_{ij}) = 0$ is displayed in Figure 1.7. The normal to the yield surface is in the direction $\partial f / \partial \sigma_{ij}$, hence, according to the associated flow rule, the plastic strain increment vector is normal to the yield surface [5].

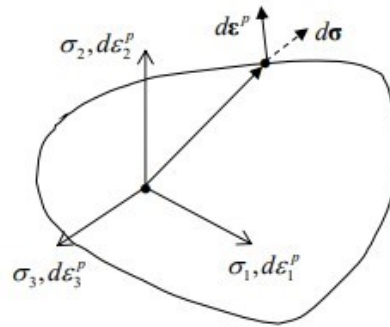


Figure 1.7 - Yield surface

By applying Equation (1.33) to the von Mises yield criterion, it results that:

$$\begin{bmatrix} d\epsilon_1^p \\ d\epsilon_2^p \\ d\epsilon_3^p \end{bmatrix} = d\lambda \begin{bmatrix} \frac{2}{3} \left(\sigma_1 - \frac{1}{2} (\sigma_2 + \sigma_3) \right) \\ \frac{2}{3} \left(\sigma_2 - \frac{1}{2} (\sigma_1 + \sigma_3) \right) \\ \frac{2}{3} \left(\sigma_3 - \frac{1}{2} (\sigma_1 + \sigma_2) \right) \end{bmatrix} \quad (1.34)$$

which is none other than the Levy-Mises flow rule. Figure 1.8 shows the strain increment components, which are perpendicular to the von Mises yield locus.

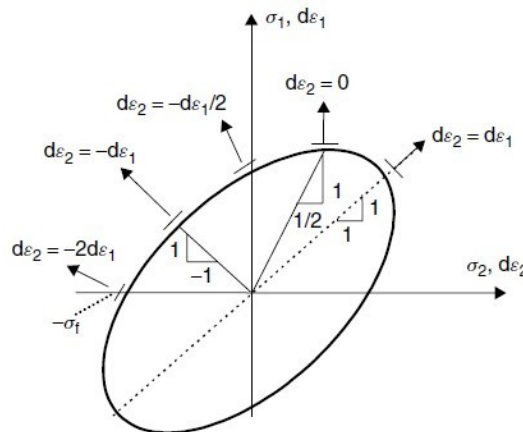


Figure 1.8 - Strain increment components for different stress states around the von Mises yield locus.

In Figure 1.9 the main modes of deformation are represented, by considering the major principal direction 1, coincident with the vertical axis, as the direction along which the largest principal stress is and, therefore, the greatest strain. As a consequence, all points will be to the left of the right-hand diagonal [1].

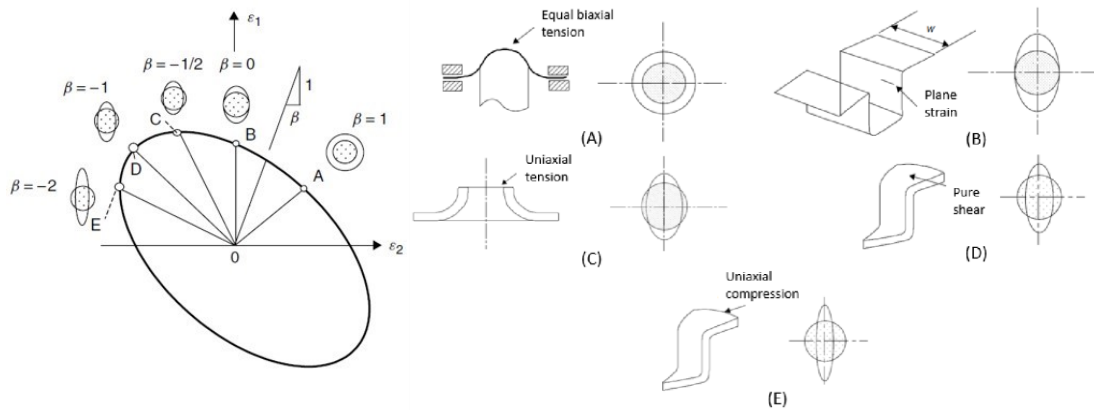


Figure 1.9 - Strain diagram shows the different deformation modes corresponding to different strain ratios. (A) Equibiaxial stretching. (B) Deformation in plane strain. (C) Uniaxial extension. (D) Pure shear. (E) Uniaxial compression.

1.4 Load instability

The forming processes may be limited or terminated by certain events and part of the analysis of these operations has to include the prediction of these limits. One of the events that may limit the forming operation is the *localized necking or tearing*. When any local neck occurs it rapidly leads to tearing and failure, and therefore, to the end of a forming operation. It is observed that in continuous sheet, local necks develop similarly to those that occur within the diffuse neck of a tensile test-piece. The width of the local necks is almost equal to the thickness of the sheet and they do not influence the global strain distribution [1]. However, they cause tearing, resulting in the quick end of the process. For this reason, in designing sheet forming processes, it is crucial to understand the conditions under which local necks develop. In the following a model to predict necking is described.

A region of the sheet deforming uniformly in a proportional process is shown in Figure 1.10. The deformation in this region is described by Equations (1.6a) and (1.6b).

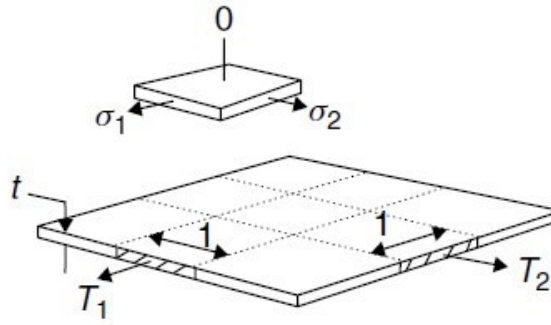


Figure 1.10 - Uniform deformation of part of a continuous sheet in a plane stress proportional process

The principal tensions in the sheet are:

$$T_1 = \sigma_1 t \quad \text{and} \quad T_2 = \alpha T_1 = \sigma_2 t \quad (1.35)$$

These tensions will remain proportional during forming.

The condition for local necking is that it starts when the major tension reaches a maximum. The process is proportional, so α and β are constant. By differentiating Equation (1.35), it is found that:

$$\frac{dT_1}{T_1} = \frac{d\sigma_1}{\sigma_1} + \frac{dt}{t} = \frac{d\sigma_1}{\sigma_1} + d\varepsilon_3 = \frac{d\sigma_1}{\sigma_1} - (1 + \beta)d\varepsilon_1 \quad (1.36)$$

When the tensions reach a maximum the derivative equals zero, thus Equation (1.36) becomes:

$$\frac{1}{\sigma_1} \frac{d\sigma_1}{d\varepsilon_1} = 1 + \beta \quad (1.37)$$

Before proceeding, it is necessary to recall the equivalent strain function:

$$\bar{\varepsilon} = \sqrt{\frac{2}{9}[(\varepsilon_1 - \varepsilon_2)^2 + (\varepsilon_2 - \varepsilon_3)^2 + (\varepsilon_3 - \varepsilon_1)^2]} \quad (1.38)$$

Replacing Equation (1.6a) in Equation (1.38), it results that:

$$\bar{\varepsilon} = \sqrt{\frac{4}{3}(1 + \beta + \beta^2)\varepsilon_1} \quad (1.39)$$

The equivalent stress $\bar{\sigma}$ is described by the following function:

$$\bar{\sigma} = \sqrt{\frac{1}{2}[(\sigma_1 - \sigma_2)^2 + (\sigma_2 - \sigma_3)^2 + (\sigma_3 - \sigma_1)^2]} \quad (1.40)$$

that, with the hypothesis of plane stress and proportional process (Equation (1.6b)) becomes:

$$\bar{\sigma} = \left(\sqrt{1 - \alpha + \alpha^2} \right) \sigma_1 \quad (1.41)$$

For a material that obeys the generalized stress-strain law:

$$\bar{\sigma} = K(\bar{\varepsilon})^n \quad (1.42)$$

It may be shown that, by substituting Equation (1.39) and (1.41) in Equation (1.42), the relationship between principal stress and strain during the deformation process can be written as:

$$\sigma_1 = K'(\varepsilon_1)^n \quad (1.43)$$

where K' is a material constant that can be computed from K , n , α and β .

By calculating the derivative of Equation (1.43), the following relation is obtained:

$$\frac{1}{\sigma_1} \frac{d\sigma_1}{d\varepsilon_1} = \frac{n}{\varepsilon_1} \quad (1.44)$$

and substituting in Equation (1.37), the local necking condition is found:

$$\varepsilon_1^* = \frac{n}{1 + \beta} \quad \text{and} \quad \varepsilon_2^* = \frac{\beta n}{1 + \beta} \quad (1.45a)$$

or

$$\varepsilon_1^* + \varepsilon_2^* = n \quad (1.45b)$$

Here the star indicates the strain at maximum tension. In case of tensile test $\beta = -1/2$. If the maximum tension condition represents the onset of local necking as assumed, the local necking strain in uniaxial tension occurs when $\varepsilon_1^* = 2n$.

1.5 DC04

In this section a brief description of the material used in the mechanical tests is given. The material chosen is an industrial cold-rolled steel sheet. More details can be found in [6]. The steel sheet has a nominal thickness of 1 mm and its chemical composition is shown in Table 1.

Designation	C (%)	Mn (%)	P (%)	S (%)
DC04	0.08	0.40	0.03	0.03

Table 1 - Chemical composition test material

Standard tensile tests were conducted to determine the work hardening properties, the maximum uniform strain ε_{max} and r-values along 0° , 45° and 90° directions with

respect to the Rolling Direction (RD). These informations are reported in Table 2 and the uniaxial strain-stress curves are plotted in Figure 1.11.

r0	1.645
r45	1.18
r90	2.09

Table 2 - Lankford parameters retrieved from classical tests

K [MPa]	547
n	0.268538
ϵ_0	0.009337

Table 3 - Swift's hardening law fitted in a range from $e_{q^{pl}} = 0,01$ up to $e_{q^{pl}} = 0,25$

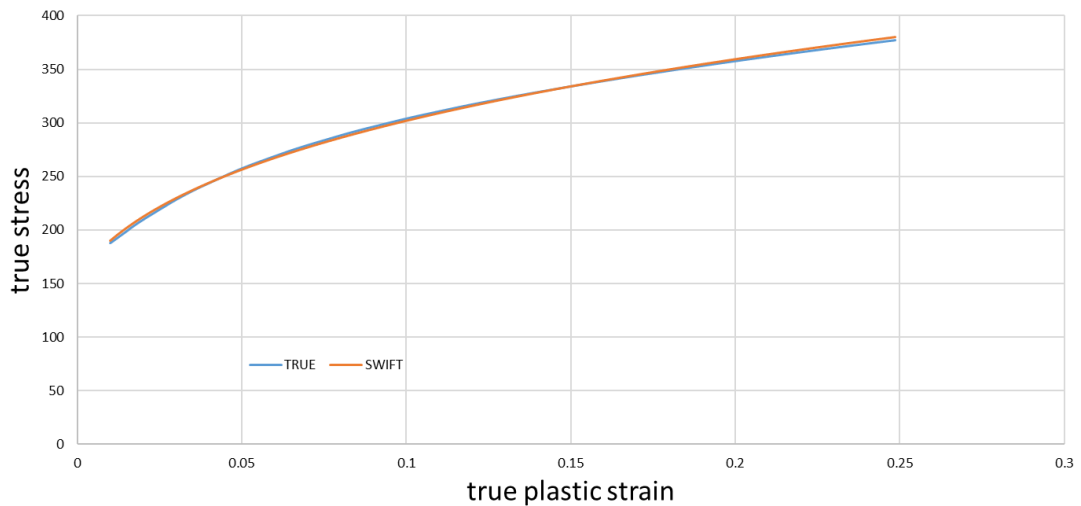


Figure 1.11 - Uniaxial stress-strain curve along the rolling direction (RD). The SWIFT curve is formulated by minimizing the variance with the experimental TRUE curve.

Chapter 2

General framework of FEMU

2.1 Basic principles of inverse modelling

In order to identify an unknown set of material parameters, which cannot be measured using a single homogeneous test, an inverse methodology is required. Thanks to the improvement of full-field measurement techniques, inverse modelling offers accuracy and flexibility. The five main methods are: the Finite Element Model Updating method (FEMU), the Constitutive Equation Gap Method (CEGM), the Equilibrium Gap Method (EGM), the Virtual Fields Method (VFM) and the Reciprocity Gap Method (RGM) [8]. FEMU and VFM are among the most commonly used. Both methods require a full-field measurement technique, such as Digital Image Correlation (DIC). The VFM method is based on the Principle of Virtual Work (PVW), according to which the external work must be equal to the internal work during deformation. Hence, the discrepancy between internal and external work is minimized by adapting the parameters of the constitutive model. With this approach FE simulations are not required. However, since DIC is able only to measure over the surface of the specimen, the assumption of plane stress is used, which means that VFM should be applied only if the plane stress assumption is verified [9].

On the other hand, the Finite Element Model Updating (FEMU) involves both FE modelling and full-field measurements techniques. This method is based on the discrepancy between the experimentally measured and numerically computed data, which is represented by a cost function, dependent on the material parameters. The constitutive parameters are identified when the difference reaches a minimum. The flowchart in Figure 2.1 illustrates the basic principles of FEMU. The left side of the flowchart shows a tensile experiment in which DIC is used to obtain the strain field. The same experiment is modelled using the FE analysis (Abaqus/Standard [10]), with a certain plastic model whose unknown parameters need to be identified [11].

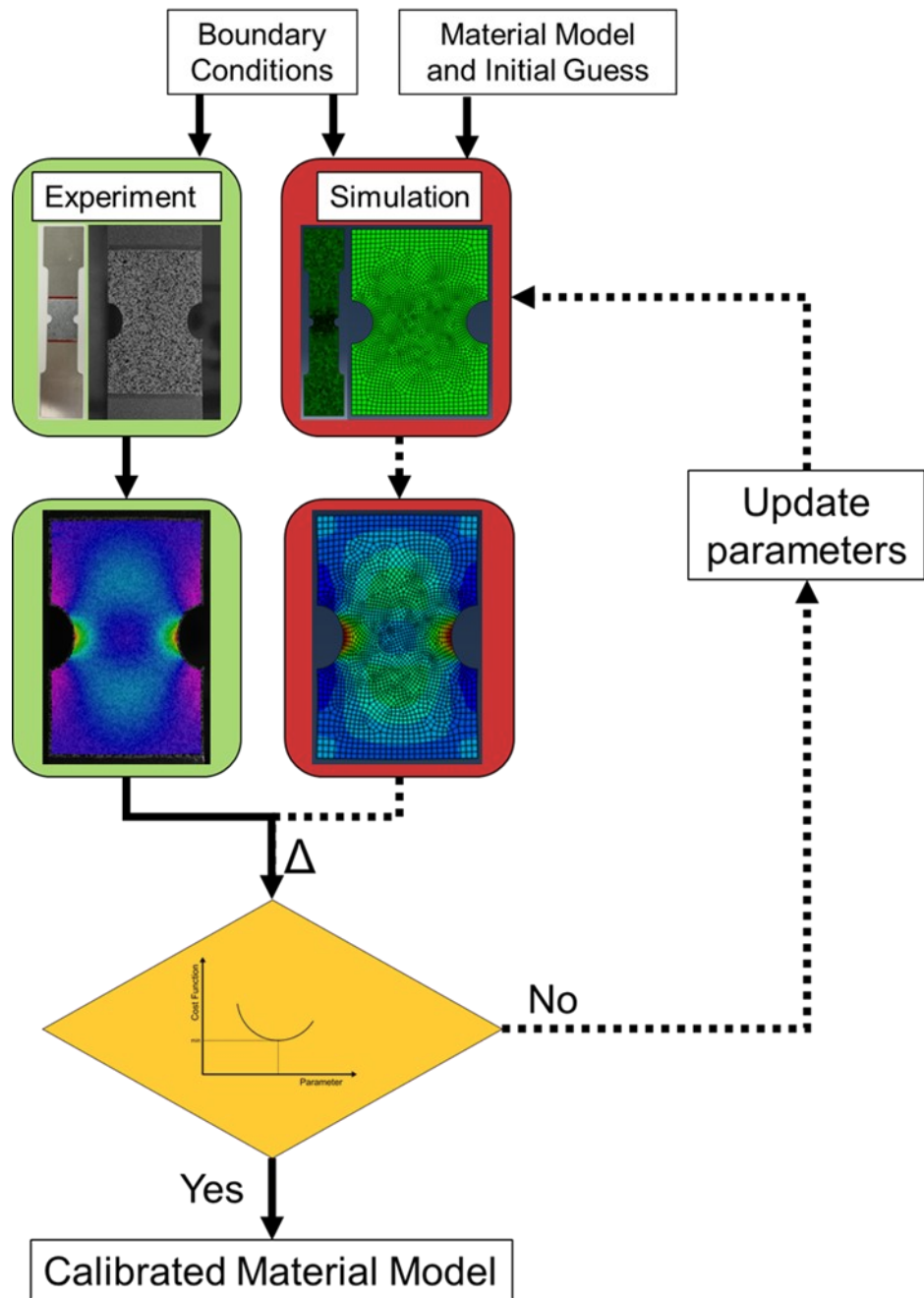


Figure 2.1 - Principle of the FEMU method

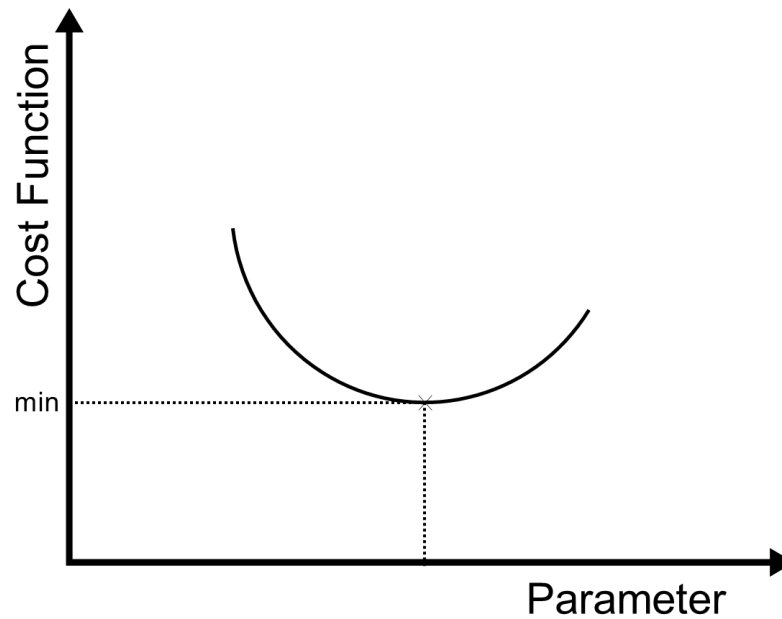


Figure 2.2 – Cost function varying with a defined parameter

The FEMU approach is adopted in the current work. Its main ingredients are briefly discussed in the following subchapters

2.2 Digital Image Correlation technique

The Digital Image Correlation (DIC) technique is an optical-numerical technique used to measure the evolving full-field 2D or 3D coordinates on the surface of a specimen throughout a mechanical test. The measured coordinate fields can be used to calculate derived field quantities-of-interest (QOIs), such as displacements, strains, strain rates, velocities and curvatures. DIC can be adopted in a wide variety of applications to investigate and characterize the deformation of solids since it is a non-contact technique, thus independent on the material being tested or the length-scale of interest. Some common materials that are tested include metals, polymers, concrete, geological samples, biological tissues, battery electrodes, explosives, etc. and test pieces range from, for example, small coupons used in tensile tests up to entire sub-assemblies of aircraft [12]. The operating principle of DIC consists in estimating full-field coordinates and displacements from a sequence of digital images of the surface of a test piece. Because the surface textures of most materials do not have a significant difference in grey level, an artificial speckle pattern is applied. A fundamental assumption in DIC measurements is that the pattern on the surface of the test piece

follows the deformation of the material. Such a pattern is generally created by applying a white base coat with a random black speckle pattern painted on top of it. Regarding the dimensions of an individual speckle, values that range from a maximum of 5 px [13, 14] to a minimum of 3 px [15] are suggested. Another important parameter is the coverage factor, which expresses the percentage of the surface covered by the speckle pattern. The concerning factor should range between 40% and 70% for optimal measurements [13]. The images of the test piece taken throughout the test can be correlated to produce full-field coordinates representative of the shape, motion and deformation of the surface. 2D coordinates can be measured using a single camera system, this is the case of 2D-DIC. 3D coordinate measurements of the surface require at least 2 cameras (3D-DIC or Stereo-DIC). Before measurements are made, the camera/lens system is calibrated by taking pictures of a calibration target (see Figure 2.3), which is rotated and translated during the calibration procedure.

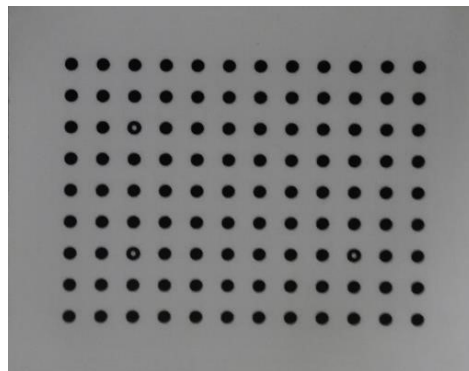


Figure 2.3 - Calibration target

The calibration allows DIC software to correct for lens distortion and, for stereo-DIC, provides the location and orientation of the cameras in space with respect to each other, and to the test piece. The parameters that can be obtained from the calibration process can be distinguished into intrinsic and extrinsic camera parameters [16]. The intrinsic parameters are those that relate a single camera image to the world, they include: the sensor center point, lens focal length, camera skew and any lens distortions. The extrinsic parameters, which relate the cameras to one other in the space, are the cameras relative orientations and x, y, and z positions in space. Before starting calibration, however, it is fundamental to determine the required Depth-Of-Field (DOF) so that the entire Region-Of-Interest (ROI) remains in focus during the test. To do so, the desired aperture is selected. The aperture of the lens governs how much light

enters the optical system. For Stereo-DIC, the aperture should be the same, or at least as close as possible, in both cameras. Typically, the aperture is chosen based on the desired DOF, while external light and exposure are regulated in order to limit motion blur and achieve sufficient contrast [12]. The software code analyzes a user-defined Region-Of-Interest (ROI). The commercial code employed in this work is MatchID [17], which is based on the so-called subset method. The correlation consists in tracking a series of pixels inside a square, denoted as subset, from the undeformed to the deformed image. The reason why only one pixel cannot be used in the correlation process is given by the fact that the same grey level, which characterizes the concerned pixel, can be observed multiple times in the same picture, which means that its uniqueness is not guaranteed. As a consequence of this, a virtual grid is created, partitioned in square areas (subsets), which in turn are formed by a certain number of pixels. A subset should be large enough to contain sufficient information so that one subset can be distinguished from all other subsets in ROI (see Figure 2.6). The rule of thumb is that the subset should contain a minimum of three DIC speckles. If the speckles are in the optimum 3-5 pixels size range and the speckle pattern density is 50%, then subsets of approximately 15x15 are required.

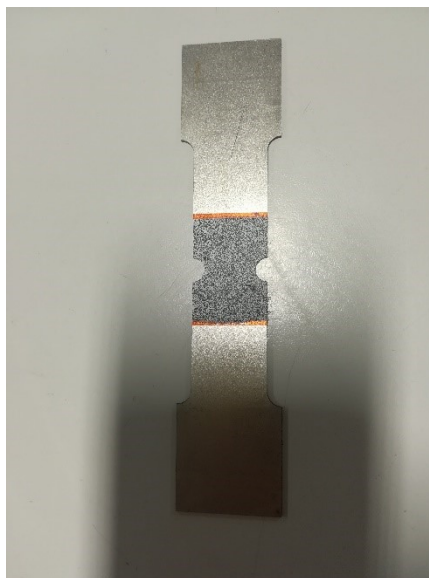


Figure 2.4 - Specimen with manually applied speckle pattern in the AOI

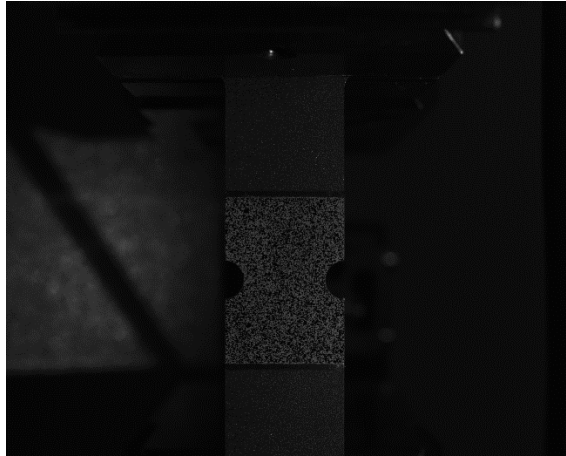


Figure 2.5 - Image of the AOI grabbed with a frontal DIC camera

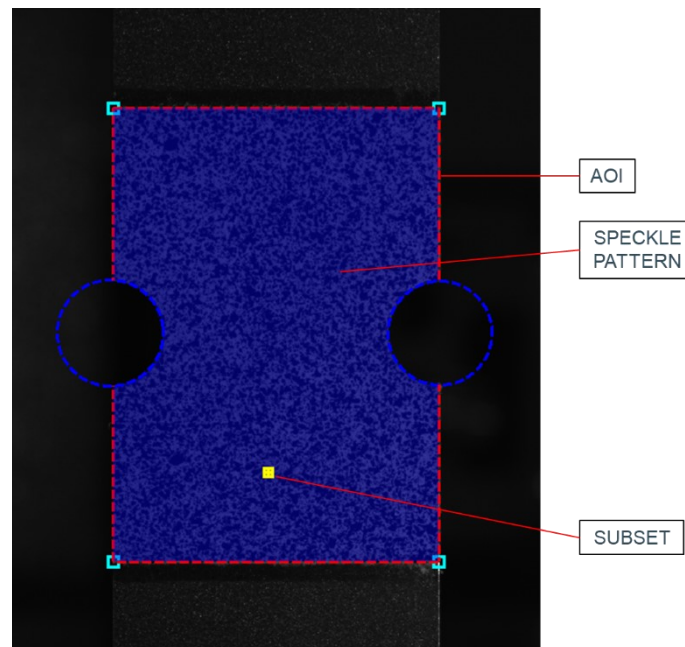


Figure 2.6 - Subset, area/region-of-interest (AOI/ROI), speckle pattern

Each subset contains an interrogation point or measurement point. The interrogation points are typically defined at some regular spacing, expressed by the step size. The subsets are numerically correlated from the undeformed image (or reference image) to each subsequent deformed image. During the correlation process the subset can change shape to consider the deformation of the specimen. The affine transformation is usually used to describe the way in which the subset can deform. The general form of a 2D affine transformation is:

$$\begin{bmatrix} u(x, y) \\ v(x, y) \end{bmatrix} = \begin{bmatrix} u \\ v \end{bmatrix} + \begin{bmatrix} \frac{\partial u}{\partial x} & \frac{\partial u}{\partial y} \\ \frac{\partial v}{\partial x} & \frac{\partial v}{\partial y} \end{bmatrix} \begin{bmatrix} \Delta x \\ \Delta y \end{bmatrix} \quad (2.1)$$

An affine transformation is a transformation that preserves collinearity, which means that all the points located on a line remain on a line after transformation, and ratios of distances, i.e. the midpoint of a line segment remains the midpoint after transformation. Therefore, it can represent rigid body motion, shear and normal straining [5].

When a pixel (x, y) in the center of the subset, noted as integration point, is shifted by a displacement (u, v) , the corresponding point in the deformed subset will be $(x+u, y+v)$. If the grey level of the undeformed subset is denoted with f and the grey level of the deformed one with g , the correlation process intends to minimize the difference between $f(x, y)$ and $g(x+u, y+v)$, which is expressed by a correlation function. The unknown parameters $\left(u, v, \frac{\partial u}{\partial x}, \frac{\partial u}{\partial y}, \frac{\partial v}{\partial x}, \frac{\partial v}{\partial y}\right)$ are determined by minimizing the correlation function, thus, by matching the same subset in the undeformed and deformed image as shown in Figure 2.7.

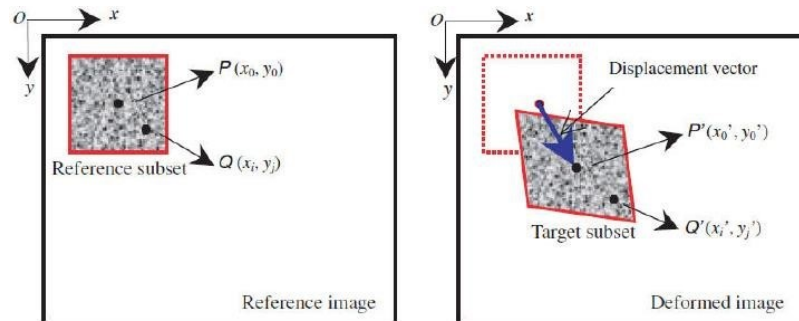


Figure 2.7 - A subset in the reference image is tracked in the deformed image and the displacement vector of the integration point is retrieved

Furthermore, an interpolation function can be employed so that the deformation can be obtained at sub-pixel level, leading to a better accuracy. Typically, polynomial or B-spline interpolation functions are adopted.

Different correlation criteria can be used to deal with offset and scaling of light conditions [18]. The first is called *Sum of Squared Differences* (SSD) criterion and it is defined as:

$$C_{SSD} = \sum_i^N \sum_j^N [f(x_i, y_j) - g(x'_i, y'_j)]^2 \quad (2.2)$$

with N the dimension of the subset in pixels, f and g are the grey values of the pixel in the undeformed and deformed configurations respectively, x_i and y_i represent the coordinates in the undeformed configuration, while x'_i and y'_i are the coordinates in the deformed configuration. This is the fastest and the simplest criterion. However, it does not take into account any scaling of lightning, hence it is not a robust criterion and, consequently, it is not usually recommended.

The second one is *Normalized Sum of Squared Differences* (NSSD) criterion:

$$C_{NSSD} = \sum_i^N \sum_j^N \left[\frac{f(x_i, y_j)}{\bar{f}} - \frac{g(x'_i, y'_j)}{\bar{g}} \right]^2 \quad (2.3)$$

where

$$\bar{f} = \sqrt{\sum_i^N \sum_j^N [f(x_i, y_j)]^2} \quad \text{and} \quad \bar{g} = \sqrt{\sum_i^N \sum_j^N [g(x'_i, y'_j)]^2} \quad (2.4)$$

By adopting normalization, the criterion can take into account the scaling of intensity. The NSSD criterion is more robust than the previous one and it is suggested for most of the analysis.

The last criterion and the more sophisticated is the *Zero-Normalized Sum of Squared Differences* (ZNSSD) criterion:

$$C_{ZNSSD} = \sum_i^N \sum_j^N \left[\frac{f(x_i, y_j) - f_m}{\Delta f} - \frac{g(x'_i, y'_j) - g_m}{\Delta g} \right]^2 \quad (2.5)$$

with

$$\Delta f = \sqrt{\sum_i^N \sum_j^N [f(x_i, y_i) - f_m]^2} \quad \text{and} \quad \Delta g = \sqrt{\sum_i^N \sum_j^N [g(x'_i, y'_j) - g_m]^2} \quad (2.6)$$

f_m and g_m are the average values of grey levels of the subsets in the undeformed and deformed image, respectively. This formulation allows to make the measurement independent on the offset and scaling of lightning conditions.

The process described above allows to compute the displacement field. However, strain fields are more interesting than displacement fields since they are directly

connected to the material properties. Once the surface displacements have been measured using DIC, the strains can be derived subsequently. To accomplish this the displacement field is locally approximated by a polynomial function to smooth the noise present on the displacement data. The strain field can be afterwards calculated by derivation of these analytical functions. The interrogation points of a predefined number of subsets, which form the so-called strain window, are used to locally fit the measured displacement field. The strain value is computed by means of a FE code at a certain point, defined as Gauss point. During this procedure two parameters can be varied: the size of the strain window and the order of the polynomial functions. Increasing the polynomial order will lead to a larger accuracy of the fit but will result in a higher standard deviation of the computed strain values. If the size of the strain window is reduced, both the accuracy and the standard deviation will decrease [5]. In case a bilinear polynomial function is chosen, it results that:

$$u^{fit} = f_1(x, y) = a_1 + b_1x + c_1y + d_1xy \quad (2.7)$$

$$v^{fit} = f_2(x, y) = a_2 + b_2x + c_2y + d_2xy \quad (2.8)$$

The parameters a_1 , b_1 , c_1 , d_1 and a_2 , b_2 , c_2 , d_2 are determined by minimizing the following least square cost function C:

$$C = \sum_{i=1}^N (u_i^{fit} - u_i^{exp}) \quad (2.9)$$

with N the number of data points inside the strain window, u^{fit} and u^{exp} the fitted and the experimental displacements components respectively at those data points. The strain derivation procedure is shown in Figure 2.5.

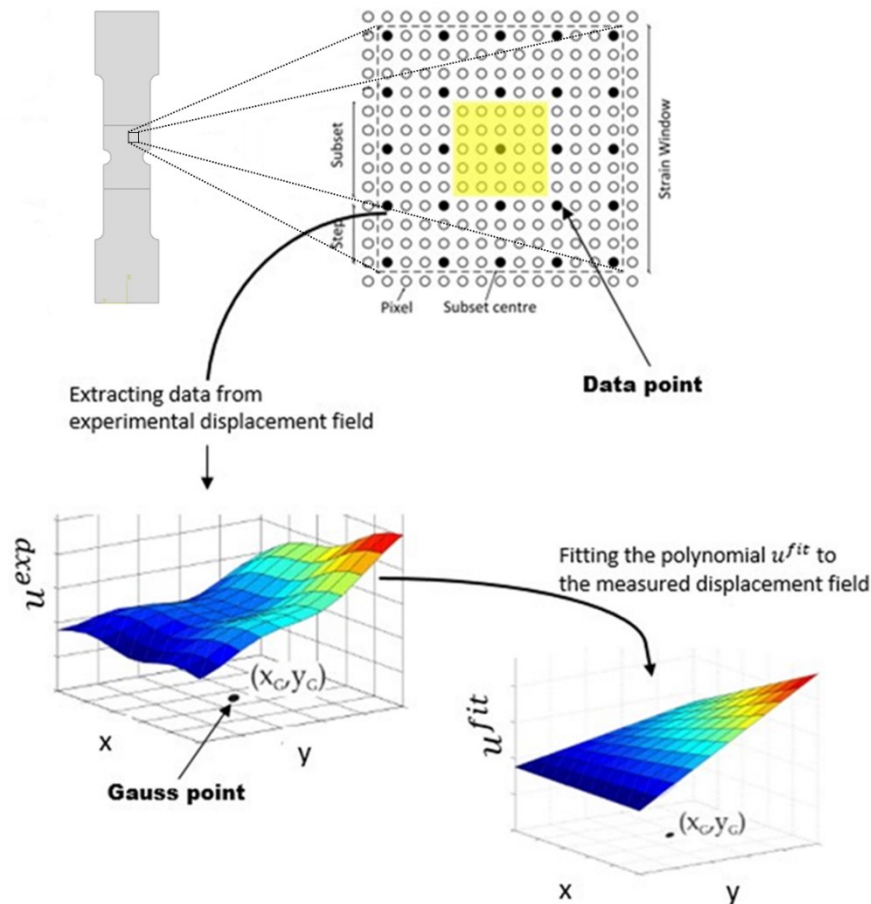


Figure 2.8 - Procedure for strain derivation

2.3 Cost function

The cost function expresses the discrepancy between the experimentally measured and the numerically computed strains. Several optimization algorithms can be found in literature. A general distinction can be made between zero-order and first order (or gradient based methods). The former algorithms require only cost function evaluations and they can find global minimum with high probability. However, these methods have the disadvantage that the cost function needs to be evaluated a lot of times due to the fact that there is no gradient information, thus they are based on probabilistic searching. First-order methods are based on gradient information to update the unknown parameters in an appropriate direction. For this reason, they can get trapped in a local minimum since they depend on the initial parameter estimates. The main advantage is given by the fact that they require far less function evaluations to reach a minimum. As just mentioned, the gradient based methods allow to find a minimum for a given cost function, whether it is a local or a global minimum. Hence, the convexity

of the cost function should be proved. However, it is impossible to guarantee that the cost function is convex. Therefore, different local minimizers should be searched by conducting several optimizations with different initial guesses and the values assumed by the cost function at the corresponding local minimizers should be afterwards compared [19].

In the present work two gradient based algorithms, named Gauss-Newton algorithm and the Levenberg-Marquardt algorithm, are chosen to identify the optimal set of parameters. The cost function $C(p)$ is defined by the least squares norm of the differences between the measured and the computed strain fields:

$$C(p) = \frac{1}{2} (\varepsilon_i^{exp} - \varepsilon_i^{num}(p)) (\varepsilon_i^{exp} - \varepsilon_i^{num}(p)) \quad (2.10)$$

with ε_i^{exp} the column vector of experimentally measured strains and $\varepsilon_i^{num}(p)$ the column vector of numerically computed strains, which are a function of the material parameters p . Equation (2.10) represents the unweighted least squares formulation. However, also a weighted least squares formulation has been proposed:

$$C(p) = \frac{1}{2} (\varepsilon_i^{exp} - \varepsilon_i^{num}(p)) W_{ij}^r (\varepsilon_i^{exp} - \varepsilon_i^{num}(p)) \quad (2.11)$$

where W_{ij}^r is a diagonal weight matrix. This matrix is composed of weights which can be calibrated so that measurement errors are minimized and higher weights are assigned to those experimental data that are trusted more [5].

If the FE simulation is displacement driven, both strain field and tensile force should be taken into account in the cost function [9]. These two physical quantities have a different order of magnitude, therefore they need to be normalized in order to have the same weight in the cost function, which can be decomposed in two parts:

$$C(p) = C(p)_1 + C(p)_2 \quad (2.12)$$

where the cost function $C(p)_1$ is formed by numerical and experimental strain data (ε_{xx} , ε_{yy} and ε_{xy}) normalized by their root mean square (RMS) of the region of interest:

$$C(p)_1 = \sum_{i=1}^m \sum_{j=1}^n \left[\left(\frac{\varepsilon_{xx,ij}^{exp} - \varepsilon_{xx,ij}^{num}}{\varepsilon_{xx,RMS,i}^{exp}} \right)^2 + \left(\frac{\varepsilon_{yy,ij}^{exp} - \varepsilon_{yy,ij}^{num}}{\varepsilon_{yy,RMS,i}^{exp}} \right)^2 + \left(\frac{\varepsilon_{xy,ij}^{exp} - \varepsilon_{xy,ij}^{num}}{\varepsilon_{xy,RMS,i}^{exp}} \right)^2 \right] \quad (2.13)$$

while the cost function $C(p)_2$ is characterized by experimentally measured and numerically computed tensile force normalized by the experimental value:

$$C(p)_2 = \sum_{i=1}^m \left[n_i \left(\frac{F_i^{exp} - F_i^{num}}{F_i^{exp}} \right)^2 \right] \quad (2.14)$$

where n_i is a weight function which allows to have an equal weight between the strain fields and the force values.

For the next considerations an unweighted cost function only based on the discrepancy between strain fields and written in matrix notation is considered:

$$C(p) = \frac{1}{2} (\varepsilon^{exp} - \varepsilon^{num}(p))^T \cdot (\varepsilon^{exp} - \varepsilon^{num}(p)) \quad (2.15)$$

The optimal set of parameters p^* is that set of values which minimize the cost function $C(p)$. This can be found by setting the partial derivative of the cost function with respect to the unknown material parameters equal to zero:

$$\left[\frac{\partial C(p)}{\partial p} \right]_{p=p^*} = 0 \quad (2.16)$$

The cost function is not explicitly known in general, hence it can be approximated with a Taylor series around p^k , i.e., the unknown set of material parameters at iteration step k .

The Taylor series approximation is truncated after the second order term:

$$\begin{aligned} C(p) \approx C^k(p) &= [C(p)]_{p=p^k} + \left(\left[\frac{\partial C(p)}{\partial p} \right]_{p=p^k} \right) (p - p^k) \\ &+ \frac{1}{2} (p - p^k)^T \left(\left[\frac{\partial^2 C(p)}{\partial p^2} \right]_{p=p^k} \right) (p - p^k) \end{aligned} \quad (2.17)$$

The minimum of this approximation can be found by computing the partial derivative of Equation (2.17) with respect to the unknown parameters p :

$$\frac{\partial C^k(p)}{\partial p} = 0 + \left[\frac{\partial C(p)}{\partial p} \right]_{p=p^k} + \left(\left[\frac{\partial^2 C(p)}{\partial p^2} \right]_{p=p^k} \right) ((p^k)^* - p^k) \quad (2.18)$$

If the partial derivative (Equation (2.18)) is set equal to zero, the minimum $(p^k)^*$ of the local approximation is calculated as:

$$p^{k+1} = (p^k)^* = p^k - \left(\left[\frac{\partial^2 C(p)}{\partial p^2} \right]_{p=p^k} \right)^{-1} \left[\frac{\partial C(p)}{\partial p} \right]_{p=p^k} \quad (2.19)$$

The minimum $(p^k)^*$ is assumed as starting point for the next iteration. The procedure is shown in Figure (2.9) for the one-dimensional case.

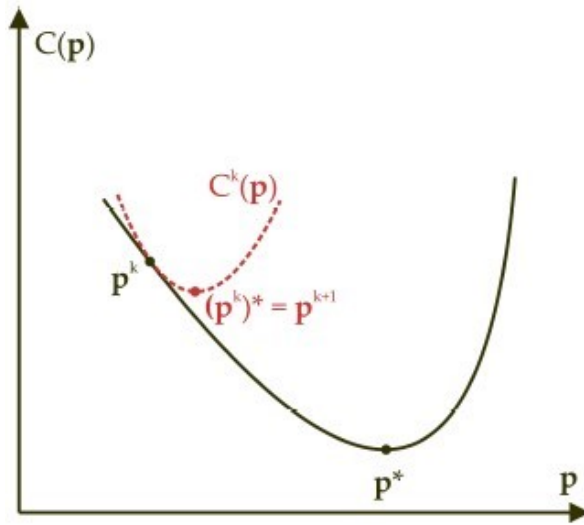


Figure 2.9 - Working principle for the Gauss-Newton method for one dimensional case. The solid black line represents the real cost function $C(p)$, the red dashed line represents the Taylor series approximation $C^k(p)$.

The first and second order partial derivatives of the cost function $C(p)$ are computed in matrix notation as:

$$\left[\frac{\partial C(p)}{\partial p} \right]_{p=p^k} = \left[- \left(\frac{\partial \varepsilon^{num}(p)}{\partial p} \right)^T \cdot (\varepsilon^{exp} - \varepsilon^{num}(p)) \right]_{p=p^k} \quad (2.20)$$

$$\left[\frac{\partial^2 C(p)}{\partial p^2} \right]_{p=p^k} = \left[\left(\frac{\partial^2 \varepsilon^{num}(p)}{\partial p^2} \right)^T \cdot (\varepsilon^{exp} - \varepsilon^{num}(p)) + \left(\frac{\partial \varepsilon^{num}(p)}{\partial p} \right)^T \cdot \left(\frac{\partial \varepsilon^{num}(p)}{\partial p} \right) \right]_{p=p^k} \quad (2.21)$$

However, the first term of Equation (2.21) is usually omitted because of two reasons [5]:

1. The inclusion of the second order derivative can be destabilizing if the model fits badly or is contaminated by outlier points;
2. The second order derivative is multiplied by the term $(\varepsilon^{exp} - \varepsilon^{num}(p))$, which, close to the minimum, is just a random measurement error that can have

positive or negative sign. Therefore, the sum of the second-order derivative terms tends to zero.

The term $\left(\frac{\partial \varepsilon^{num}(p)}{\partial p}\right)$, which expresses the sensitivity of the numerically computed strain values with respect to the material parameters p , represents the sensitivity matrix S .

Equations (2.20) and (2.21) can then be rewritten as:

$$\left[\frac{\partial C(p)}{\partial p}\right]_{p=p^k} = [S^T \cdot (\varepsilon^{exp} - \varepsilon^{num}(p))]_{p=p^k} \quad (2.22)$$

$$\left[\frac{\partial^2 C(p)}{\partial p^2}\right]_{p=p^k} = [S^T \cdot S]_{p=p^k} \quad (2.23)$$

Replacing Equations (2.22) and (2.23) in (2.19), it results:

$$p^{k+1} = p^k + [S^T \cdot S]_{p=p^k}^{-1} \cdot [S^T \cdot (\varepsilon^{exp} - \varepsilon^{num}(p))]_{p=p^k} \quad (2.24)$$

from which the vector of parameter updates Δp is obtained:

$$\Delta p = p^{k+1} - p^k = [S^T \cdot S]^{-1} \cdot [S^T \cdot (\varepsilon^{exp} - \varepsilon^{num}(p))] \quad (2.25)$$

If the cost function is given by a weighted least square formulation, the Gauss-Newton update algorithm can be expressed as:

$$\Delta p = p^{k+1} - p^k = [S^T \cdot W^r \cdot S]^{-1} \cdot [S^T \cdot W^r \cdot (\varepsilon^{exp} - \varepsilon^{num}(p))] \quad (2.26)$$

For the minimization of the cost function the Levenberg-Marquardt algorithm, originally proposed by Levenberg [20] and further developed by Marquardt [21], is strictly connected to the Gauss-Newton algorithm. As a matter of fact, the Gauss-Newton algorithm may sometimes have convergence problem, thus, the Levenberg-Marquardt algorithm has been developed and employed with the purpose of having a stable convergence. In this case, the parameter updates are computed as:

$$\Delta p = [S^T \cdot S + \delta I]^{-1} \cdot [S^T \cdot (\varepsilon^{exp} - \varepsilon^{num}(p))] \quad (2.27)$$

The δ parameter is a strictly positive scalar to ensure that the matrix $[ST, S + \delta I]$ is positive definite and I is the unit matrix. It has been experienced that this additional matrix has a positive influence on the conditioning of the problem and on its stability when the standard Gauss-Newton algorithm is adopted. If the parameter δ is chosen to be large, the Levenberg-Marquardt algorithm tends towards the steepest descent method. When it is small, the Levenberg-Marquardt algorithm tends towards the Gauss-Newton algorithm. As previously reported, the Gauss-Newton and Levenberg-Marquardt algorithms require the computation of a sensitivity matrix \mathcal{S} , which quantifies the influence of the model parameters on the output quantities of the numerical model. Three different methods can be found in literature to compute this matrix [5]: finite differentiation, adjoint method and direct differentiation. However, the latter two methods require direct access to the FE code and this is not possible since a commercial FE code is used (Abaqus/Standard). Finite differentiation is the oldest and the most widely adopted algorithm to compute the sensitivity matrix because it can be implemented rather easily and it doesn't require access to the FE code. With this method the partial derivative is calculated by introducing a perturbation in the model parameters:

$$S_{ij} = \frac{\partial C(p)}{\partial p_j} \approx \frac{(\varepsilon_i^{num}(p, p_j + \Delta p_j) - \varepsilon_i^{num}(p, p_j - \Delta p_j))}{2\Delta p_j} \quad (2.28)$$

where Δp_j is the parameter perturbation. The advantage of this approach, named centred finite differentiation scheme, is its accuracy, but it requires two more FE simulations per iteration and per unknown parameter.

Two more efficient schemes, from the computational point of view, are the forward and backward finite differentiation, where the sensitivity coefficients are respectively calculated as follow:

$$S_{ij} \approx \frac{(\varepsilon_i^{num}(p, p_j + \Delta p_j) - \varepsilon_i^{num}(p))}{\Delta p_j} \quad (2.29)$$

$$S_{ij} \approx \frac{(\varepsilon_i^{num}(p) - \varepsilon_i^{num}(p, p_j - \Delta p_j))}{\Delta p_j} \quad (2.30)$$

These two methods require only one extra FE simulation per iteration and per unknown parameter. If the parameter perturbation Δp_j is chosen rather small, the difference

between the centred method and the forward or backward one is minimal. This means that the forward or backward approach should be preferred over the centred because of its larger efficiency. However, the finite differentiation method remains very inefficient from a computational point of view. The centred, forward and backward differentiation schemes are shown in Figure 2.7.

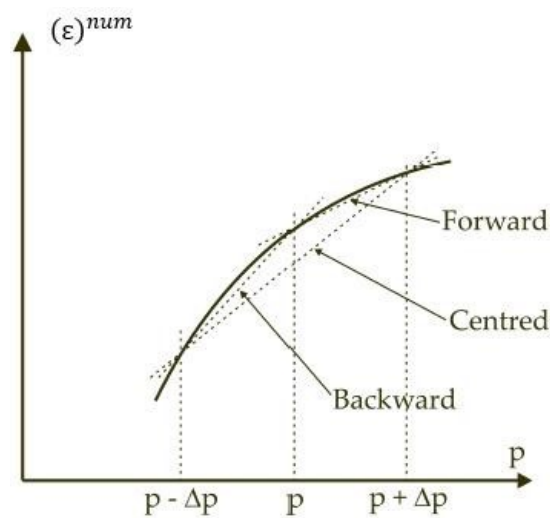


Figure 2.10 - Comparisons of the centred, forward and backward finite differentiation approximation schemes

The flowchart in Figure 2.11 illustrates the implemented algorithm for parameters identification. The algorithm is initialized with the Gauss-Newton algorithm. If it has stability problems in finding a smaller cost function than the one previously computed, it transitions to the Levenberg-Marquardt algorithm. The value of δ is chosen to be 10^{-7} , producing mostly the same result as the Gauss-Newton algorithm. If the parameter update Δp gives different values than the current values, the cost function is evaluated. The value of δ increases with a factor of 10 each time the new cost function is larger than the previous one. On the other hand, a smaller cost function leads to a decreasing value of δ with a division by 10 [9].

Finally, the algorithm is stopped if the ratio of the parameters changes to the current parameter value, or the ratio of the cost functions changes to the current cost function value is lower than a predefined convergence value:

$$\left| \frac{C(p_{k+1}) - C(p_k)}{C(p_k)} \right| < \xi_c \tag{2.31}$$

$$\left| \frac{p_{k+1} - p_k}{p_k} \right| < \xi_p \quad (2.32)$$

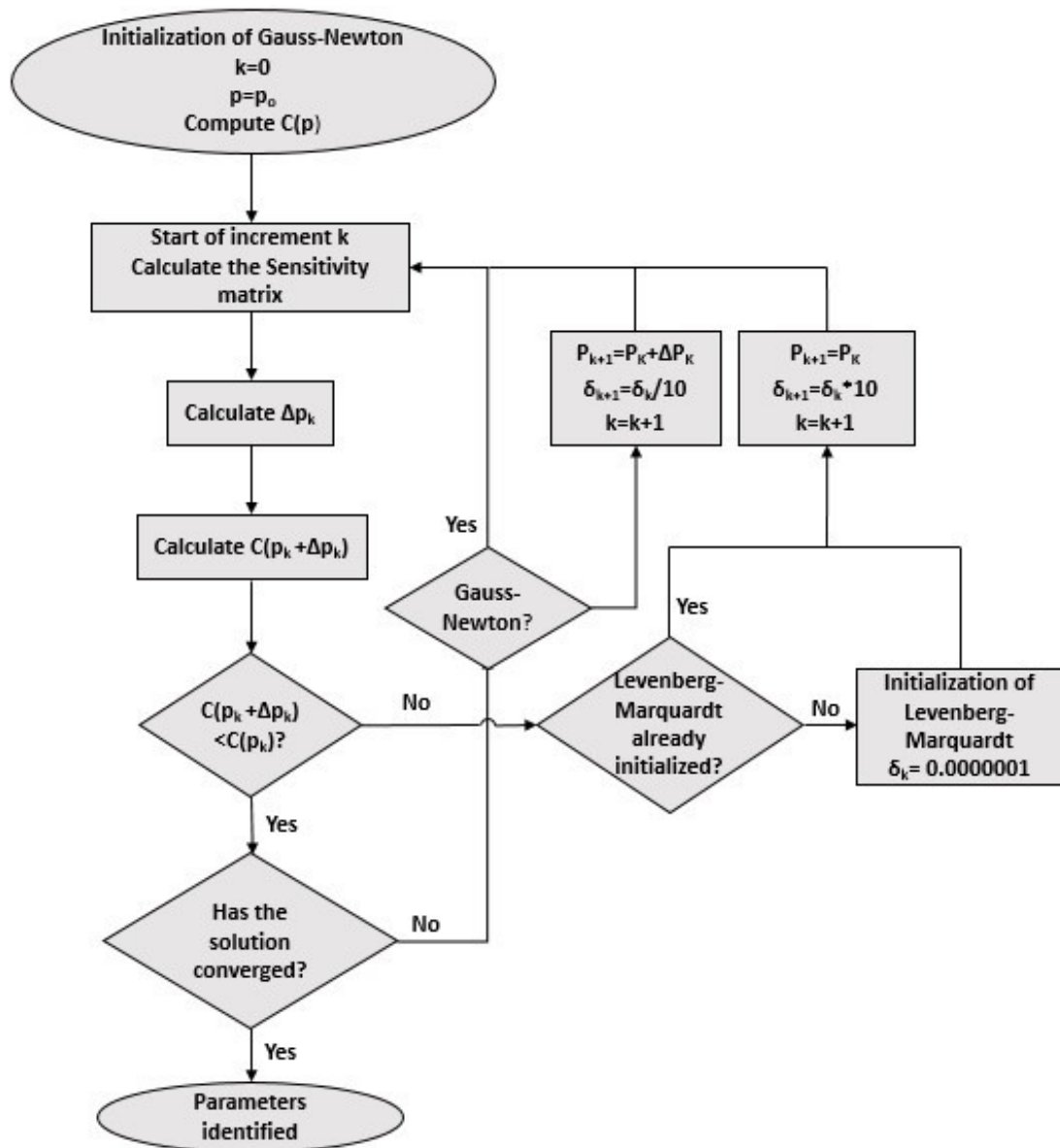


Figure 2.11 - Principle of the combined Gauss-Newton and Levenberg-Marquardt algorithms

2.4 Actual Experiment and Virtual Experiment

In this work material identifications were conducted using two different experimental methodologies.

2.4.1 Actual Experiment

In an Actual Experiment (AE), the specimen is deformed using a tensile machine and, during the test, images of the surface of the specimen in the AOI are grabbed at a certain frequency, using two cameras for Stereo DIC. At the same time, the software records force measured by the load cell, creating a file in which each image is related to the corresponding force.

For this reason, in order to compare numerical and experimental results, a force-driven approach is used in Abaqus, which means in every step the applied load is the force related to the chosen experimental image.

A flowchart of material identification using AE is shown in Figure 2.12. MatchID is used to correlate the digital images grabbed in the laboratory and obtain the displacement fields, which are used as inputs for FEMid, together with the Boundary Conditions, to start the identification process. It is important to say that the material parameters in the experiment are unknown.

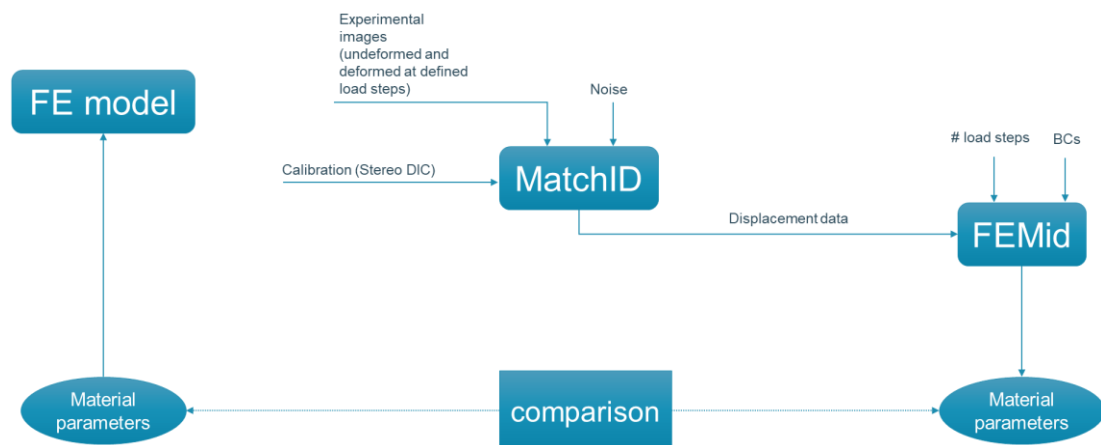


Figure 2.12 - Flowchart of material identification using AE

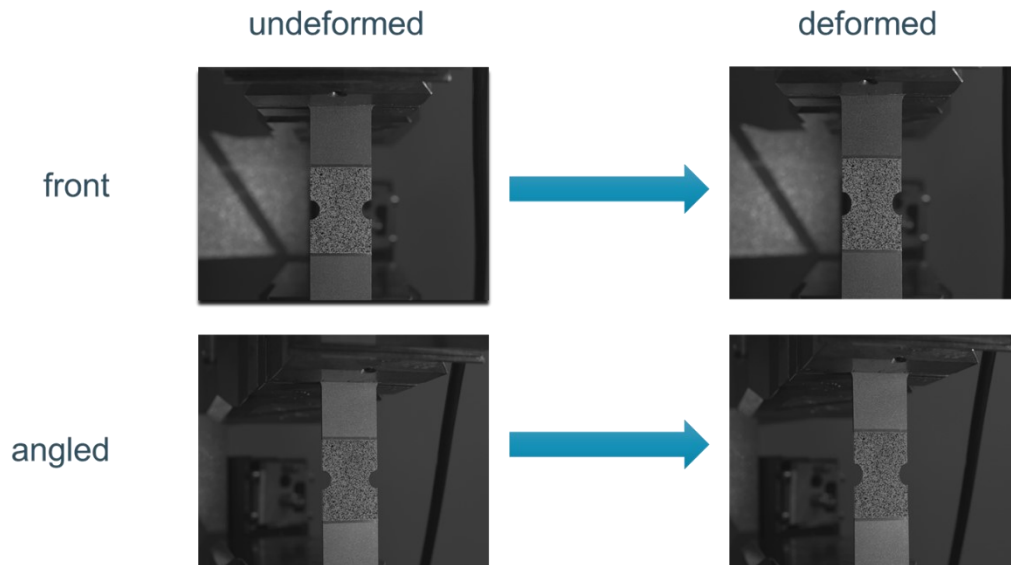


Figure 2.13 – Digital images of the AOI using Stereo-DIC

2.4.2 Virtual Experiment

In a Virtual Experiment, an image of the undeformed surface of the specimen is grabbed in the laboratory and it's then numerically deformed applying the Abaqus output files, which are coordinates and displacement fields at the end of the test. In this case, a displacement-driven approach was used in the simulation, which means in every step the specimen is subjected to a stretch caused by a displacement.

A flowchart of material identification using VE is shown in Figure 2.14. FEDEF is the MatchID module used for the numerical deformation of a real image using the Abaqus .job file, hence the results are obtained starting from known material parameters

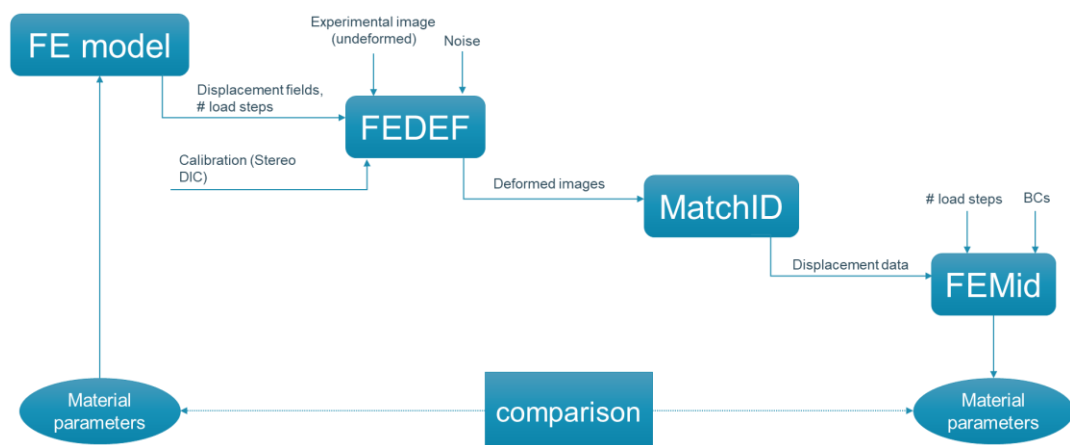


Figure 2.14 - Flowchart of material identification using AE

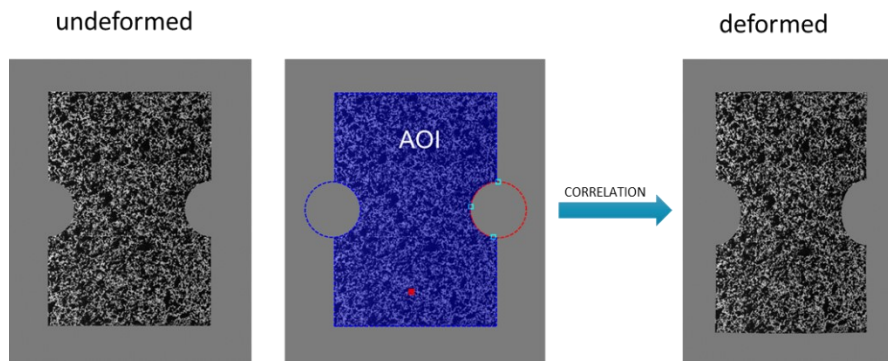


Figure 2.15 - Numerical deformation and correlation

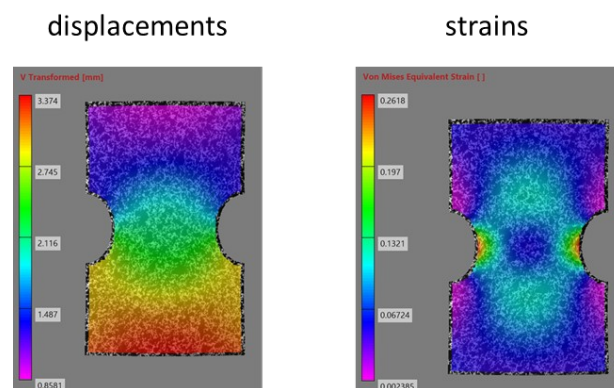


Figure 2.16 – Displacement fields and strain fields from VE

Since Abaqus and MatchID adopt two different computation approaches to derive the strain fields, FEMid utilizes the displacement fields as input, from which strain fields are consequently calculated. However, before importing the displacement fields from MatchID, a coordinate transformation is required to make the coordinate system coincide with the coordinate system of the FE model (see Figure 4.16). Nonetheless, while Abaqus adopts a left-handed coordinate system, MatchID works with right-handed coordinate systems, thus v displacements and y coordinates must change sign.

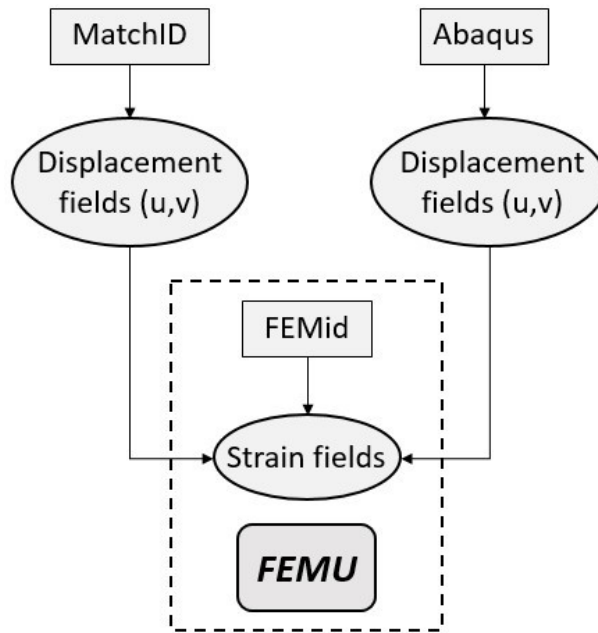


Figure 2.17 - Coordinate transformation in MatchID and strain fields computation approach in FEMid

Chapter 3

Design of heterogeneous experiments

3.1 Evaluation of heterogeneity

3.1.1 Stress state

The idea residing in the FEMU approach relies on a heterogeneously deforming specimen. In fact, it has been shown that a heterogeneous stress/strain state leads to a more robust and reliable identification of material parameters. This concept will be more deeply analyzed and discussed in the following subchapters. To this end, a specimen with notches is considered in this work. A FE model assuming the Hill'48 material model is used to investigate the stress and strain states generated in the Area Of Interest (AOI), i.e. the region in which the strains are measured. The FE model will be described in more detail in Chapter 4.

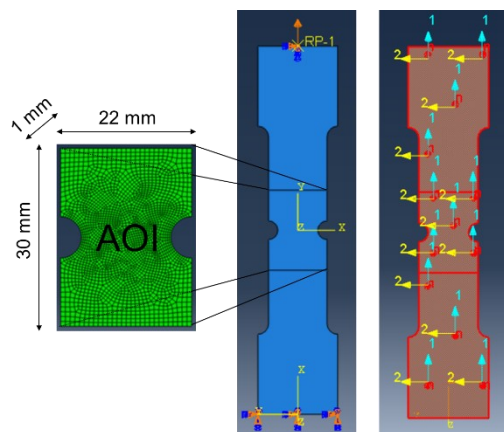


Figure 3.1 - FE model with material orientation and dimensions of the AOI. Dimension of the radius of the notches: 3.5 mm

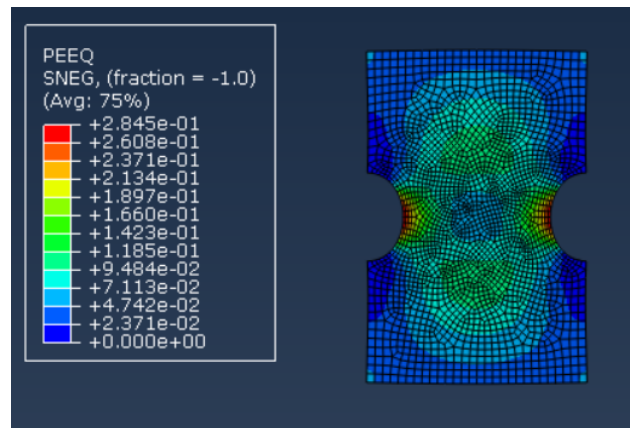


Figure 3.2 - Heterogeneous strain distribution in the AOI. Dimension of the radius of the notches: 3.5 mm

The graphs in Figure 3.3 show the stress distribution in the AOI using the Hill'48 yield locus for plane stress, coupled with the Swift hardening law, to describe the material behavior for the specimen with a 3.5mm radius of the notches. The stress components are normalized by the equivalent stress, making the stress state representation independent of the load steps. The contour lines can be plotted using Equation (1.25), which is the Hill'48 criterion written for plane stress considering local coordinates. The local stresses σ_{11} and σ_{22} are the stresses along the Rolling Direction (RD) and Transverse Direction (TD), respectively; the axis perpendicular to the plane of the figure represents the normalized shear stress σ_{12} . Each point in the graphs represents a stress state in the AOI. It can be inferred that the specimen generates stress states with positive σ_{11} , which is obvious, while σ_{22} varies in sign, which means along the TD some points are stretched and some are compressed. The points are concentrated in the vicinity of the uniaxial tensile stress and plain strain states.

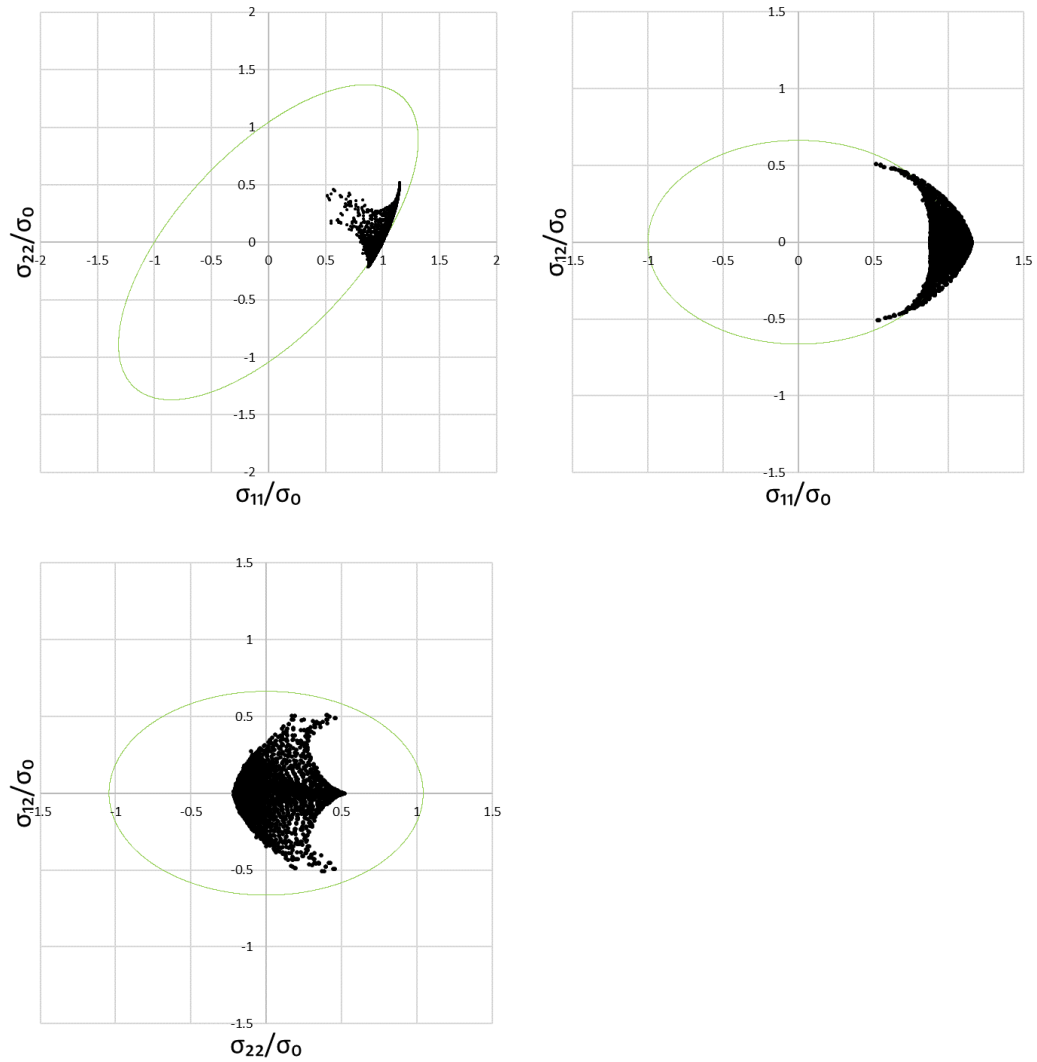


Figure 3.3 - Stress distribution in the AOI using the Hill'48. Dimension of the radius of the notches: 3.5 mm

Given the wide stress distribution, the specimen can be considered a good candidate for inverse yield locus identification through FEMU.

3.1.2 Strain state

A different approach to analyze how the AOI deforms during the mechanical test is to consider strain states, defined as the ratio between the minor ε_2 and the major ε_1 principal strains. The graph shown in Figure 3.4 is characterized by straight lines, each one with a different angle because it is related to a different strain state. It is seen that the strain states tend to cluster around the uniaxial tension strain state.

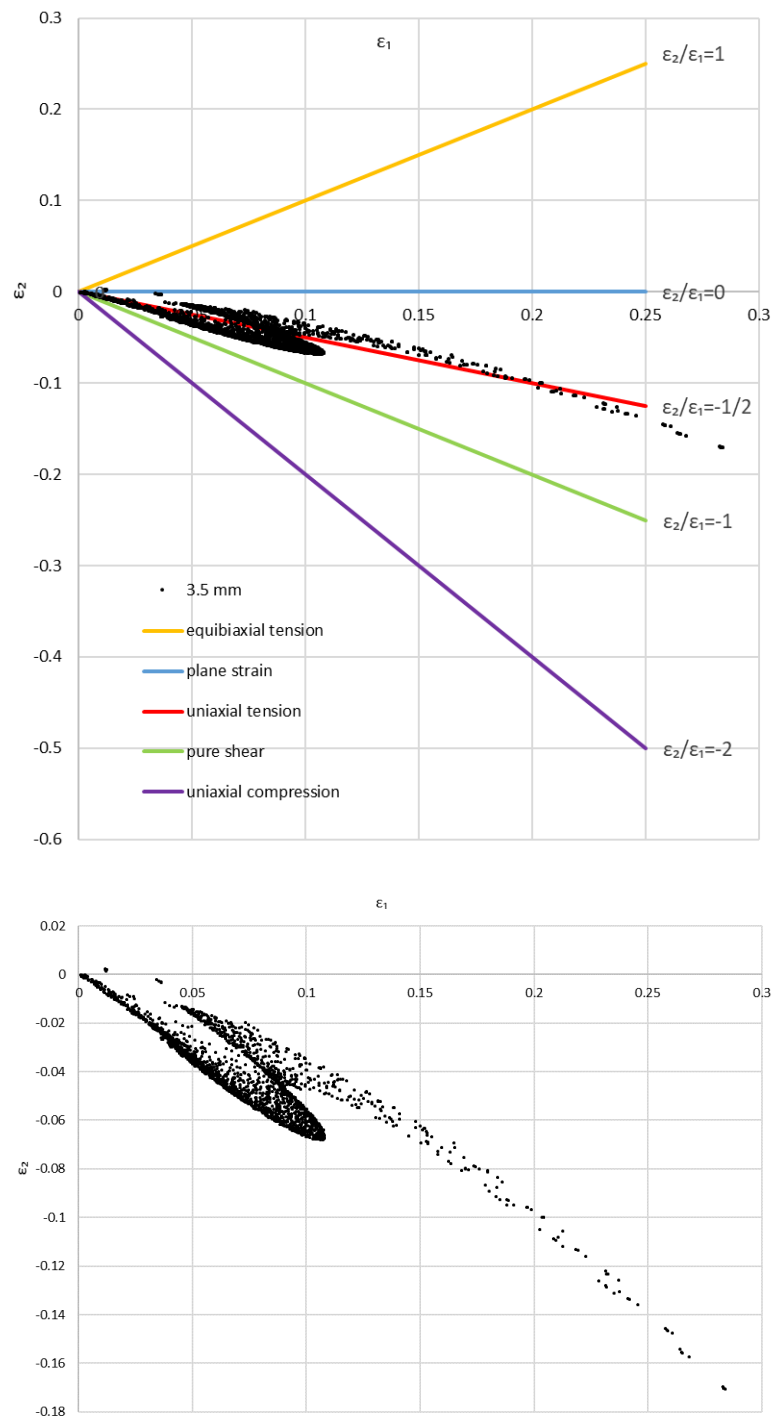


Figure 3.4 - Strain state for a specimen with 3.5 mm radius

The scatter is also an indicator of the heterogeneity for this specific specimen. The notches determine a strain concentration in the central part of the AOI and, as will be shown later, the heterogeneity of the strain distribution changes by varying the shape of the specimen.

3.2 Definition of an indicator for heterogeneity assessment

3.2.1 Definition of I_T

Over the years, material parameters have been identified using classical mechanical tests, such as, uniaxial tension and simple shear, characterized by a rather homogeneous strain distribution over the gauge area of the specimen [22, 23]. As a matter of fact, this kind of tests provides stress and strain data only for a fixed stress state, requiring more additional classical tests when the adopted constitutive model depends on several stress states. Moreover, the development of new non-linear and more complex constitutive models increased the number of material parameters to be identified, making the material identification process more expensive and time consuming. Therefore, heterogeneous experiments with the intent to reproduce non-homogeneous and multiaxial strain paths, characterizing sheet metal forming processes, have been proposed. According to [24], the quality of material parameters identified improves and the number of experiments required decreases when the heterogeneity of the strain field increases. Specimens with notches have been designed aiming at obtaining a wide range of strain paths and sensitivity to material anisotropy [25]. As a consequence of the fact that a heterogeneous strain field provides much more information than a homogeneous strain field, leading to a better characterization of the material behavior, the design of new heterogeneous tests has been the focus of several studies. With the following aims for the mechanical characterization of sheet metals:

- Identifying large sets of material parameters;
- Improving the quality and reliability of the identified parameters;
- Reducing the number of required experimental tests, a quantitative indicator able to distinguish and rate different mechanical tests has been designed. The purpose of this indicator is also to guide the design of new heterogeneous tests [26].

Since several strain states are expected during sheet metal forming processes, the strain state range must be taken into account by the indicator. The range of the strain state

$(\varepsilon_2/\varepsilon_1)_R$ of the mechanical test can be evaluated by considering the maximum and the minimum strain state values $(\varepsilon_2/\varepsilon_1)$ measured in the test:

$$\left(\frac{\varepsilon_2}{\varepsilon_1}\right)_R = \left(\frac{\varepsilon_2}{\varepsilon_1}\right)_{max} - \left(\frac{\varepsilon_2}{\varepsilon_1}\right)_{min} \quad (3.2)$$

However, Equation (3.2) does not quantify the diversity of mechanical information obtained from the test. The diversification of mechanical information provided by the test is a relevant feature and it can be assessed by measuring the strain state variation during the test. This is achieved by evaluating the standard deviation Std of $(\varepsilon_2/\varepsilon_1)$ obtained from the specimen during the test, where Std is a statistical function that reveals how much dispersion from the average exists. A low value of Std implies that the data points are close to the mean value, which is the case of homogeneous experiments, while a large value of Std indicates that the data points are spread out over a large range of values, expected for heterogeneous tests. $Std(\varepsilon_2/\varepsilon_1)$ is defined as:

$$Std\left(\frac{\varepsilon_2}{\varepsilon_1}\right) = \sqrt{\frac{\sum_i^n [(\varepsilon_2/\varepsilon_1)_i - \mu_{\varepsilon_2/\varepsilon_1}]^2}{n-1}} \quad (3.3)$$

where $(\varepsilon_2/\varepsilon_1)_i$ is the ratio $\varepsilon_2/\varepsilon_1$ for each element i of the mesh, $\mu_{\varepsilon_2/\varepsilon_1}$ is the mean value of $\varepsilon_2/\varepsilon_1$ and n is the number of elements that compose the specimen.

The heterogeneity of the strain levels of the specimen is also taken into account in the formulation of the indicator. It is assessed as the Std of the equivalent plastic strain (ε_p) :

$$Std(\varepsilon_p) = \sqrt{\frac{\sum_i^n (\varepsilon_i^p - \mu_{\varepsilon_p})^2}{n-1}} \quad (3.4)$$

Where ε_i^p is the equivalent plastic strain of the element i and μ_{ε_p} is the mean ε_p value of the specimen.

The parameters mentioned above, represent a measure of the heterogeneity that characterizes a certain mechanical test. However, also the strain level should be considered, since for material identification the same deformation level recorded in sheet metal forming processes should be reached. To that purpose, the maximum strain (ε_{MAX}^p) and the average deformation (Av_{ε_p}) achieved in the test are taken into account. The latter is calculated as:

$$Av_{\varepsilon^p} = \frac{\sum_i^n \varepsilon_i^p v_i}{v_T} \quad (3.5)$$

with v_i the volume of the element i and v_T is total volume of the specimen.

The indicator is formulated based on Equations (3.2)-(3.5) which characterize the range of strain state, heterogeneity and strain level features. Within the characterized features, ε_{MAX}^p and Av_{ε^p} consist of cumulative data of the test, thus only the values obtained at the end of the test are considered for the indicator calculation. The parameters $Std(\varepsilon_2/\varepsilon_1)$ and $Std(\varepsilon^p)$ are not cumulative and may change in different load steps. Consequently, the mean values calculated over the entire test time are taken into account in the definition of the indicator. By considering the previous assumptions, the indicator I_T is computed as:

$$I_T = w_{r1} \frac{Mean[Std(\varepsilon_2/\varepsilon_1)]}{w_{a1}} + w_{r2} \frac{(\varepsilon_2/\varepsilon_1)_R}{w_{a2}} + w_{r3} \frac{Mean[Std(\varepsilon^p)]}{w_{a3}} + w_{r4} \frac{\varepsilon_{MAX}^p}{w_{a4}} + w_{r5} \frac{Av_{\varepsilon^p}}{w_{a5}} \quad (3.6)$$

where w_r and w_a are relative and absolute weighting factors respectively. The absolute weighting factors w_a have physical meaning and correspond to the maximum achievable value for each indicator term. The weights w_{a4} and w_{a5} are defined assuming that the maximum and average plastic strain values that can be measured in the test are 1.

Regarding w_{a1} and w_{a3} , they are evaluated based on the mean values of $Std(\varepsilon_2/\varepsilon_1)$ and $Std(\varepsilon^p)$ obtained for different tests in [26]. Finally, w_{a2} is defined considering the range of the strain state limited between equibiaxial state ($\varepsilon_2/\varepsilon_1 = 1$) and a compression state with $\varepsilon_2/\varepsilon_1 = -3$, therefore, $w_{a2} = 4$. The relative weighting factors w_r are adjusted considering each one of the indicator terms for a proper calculation of I_T . The weighting factors w_{r1} , w_{r2} and w_{r3} are related to the I_T terms that evaluate strain state range/heterogeneity while w_{r4} and w_{r5} are related to the strain level. Different sets of weighting factors w_r can be adopted for I_T calculation, depending on the importance attributed to each term:

1. Equal importance (50%-50%) for strain range/heterogeneity and strain level;
2. 65%-35% importance for strain range/heterogeneity and strain level;
3. 35%-65% importance for strain range/heterogeneity and strain level.

The relative weighting factors w_r , for each of three cases, together with the absolute weighting factors are listed in Table 4 and Table 5.

	W_{r1}	W_{r2}	W_{r3}	W_{r4}	W_{r5}
I_T (50-50)	0.3	0.03	0.17	0.4	0.1
I_T (65-35)	0.36	0.05	0.24	0.23	0.12
I_T (35-65)	0.22	0.04	0.09	0.5	0.15

Table 4 - Relative weighting factors for 50-50, 65-35 and 35-65 importance for strain range/heterogeneity and strain level for I_T calculation

W_{a1}	W_{a2}	W_{a3}	W_{a4}	W_{a5}
1	4	0.25	1	1

Table 5 - Absolute weighting factors for I_T calculation

3.2.2 Application of I_T to specimen with notches

The I_T calculation is applied to the notched specimen. The purpose of this study is to evaluate the I_T indicator as a function of the radius R of the notches of the specimen. The terms characterizing the concerned indicator are evaluated up to local necking, which occurs when the sum of the major and minor principal strains equals the hardening exponent, condition expressed by Equation (1.45b).

The parametric study $I_T(R)$ is performed through FE simulations, using a commercial FE code (Abaqus/Standard [10]), which are run until Equation (1.45b) predicts local necking. As can be seen from Equation (3.6), the I_T indicator depends on terms that are functions of principal strains and elements volume, hence varying the radius of the notches will result in a variation of the aforementioned parameters, thus, in the change of the I_T value:

$$I_T = I_T \left(\left(\frac{\varepsilon_2}{\varepsilon_1} \right)_R, Std \left(\frac{\varepsilon_2}{\varepsilon_1} \right), Std(\varepsilon_p), \varepsilon_{Max}^p, Av_{\varepsilon^p} \right) = I_T(\varepsilon_1, \varepsilon_2, v) = I_T(R) \quad (3.7)$$

The values of principal strains and elements volume are obtained using a Python script, communicating with the .odb file of Abaqus.

As already stated, the simulations are terminated when local necking occurs, i.e. when the sum of the major and minor principal strains equals the exponent of the power law (refer to Table1). This condition is verified in the central area of the specimen, in the notch area.

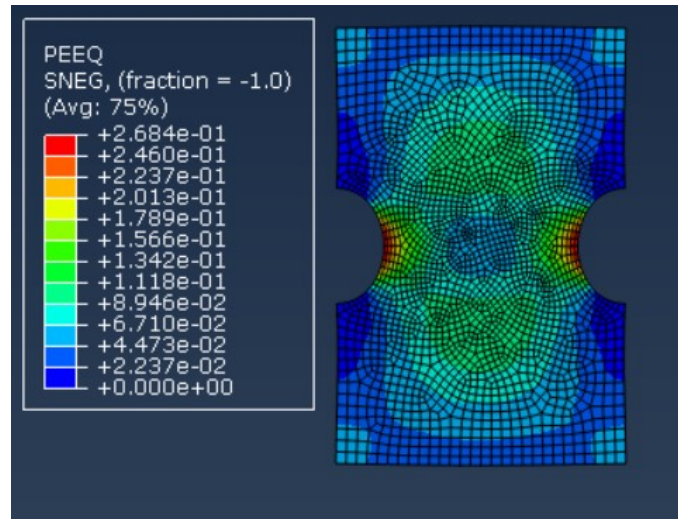


Figure 3.5 – Strain field in the AOI

In the following, the dependency on the hole radius R of the terms characterizing I_T is analyzed. As said in subchapter 3.2.1, the terms ε_{MAX}^p and $Av_{\varepsilon p}$ are cumulative, therefore only the values obtained at the end of the simulation are considered. On the other hand, $Std(\varepsilon_2/\varepsilon_1)$ and $Std(\varepsilon_p)$ are not cumulative, hence the mean values are computed.

Regarding $(\varepsilon_2/\varepsilon_1)_R$, the maximum value during the test is taken into account for I_T calculation. The simulations are carried out using a constant displacement field (i.e. assuming perfect gripping of the arm) in the upper side and a clamping in the lower side, as boundary condition.

In figure 3.6 ε_{MAX}^p is displayed as function of the radius of the notches. It has a minimum for the 0.5 mm and 6 mm radii, and a maximum for the 3.5 mm radius.

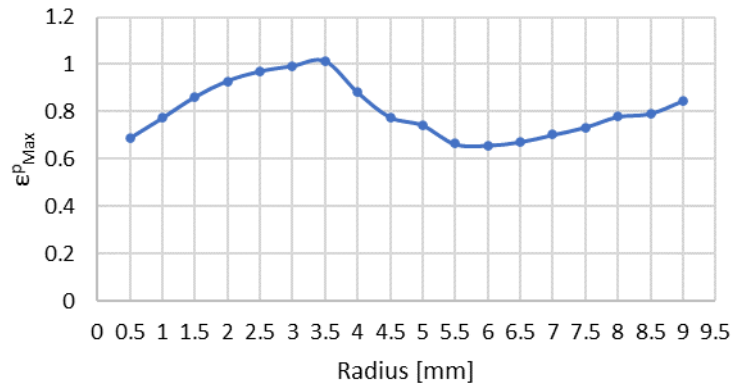


Figure 3.6 - Distribution of ϵ_{MAX}^p as function of the radius of the notches

The average deformation has a decreasing trend with the radius (see Figure 3.7) because larger notches imply a stronger localization of the strain distribution in the central area of the AOI, between the two notches, as shown in figure

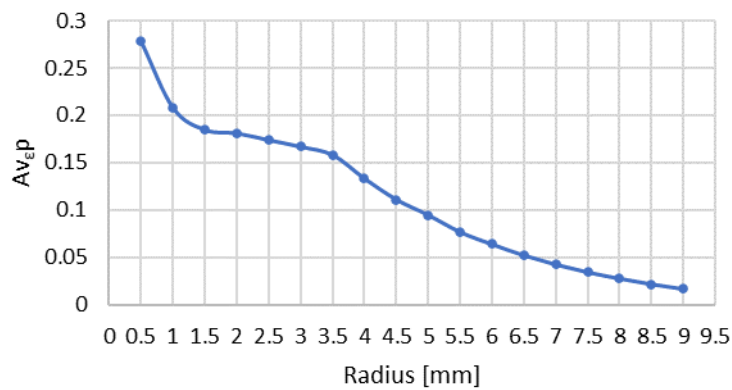
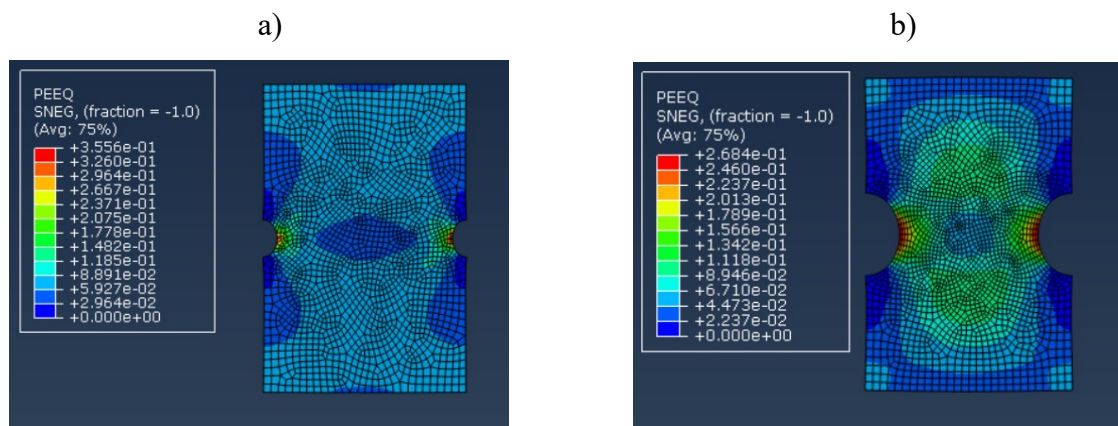


Figure 3.7 - Distribution of Av_{ϵ^p} as a function of the radius



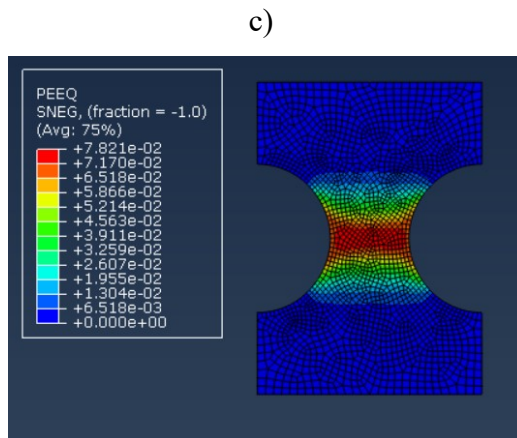


Figure 3.8 – Strain fields for radii a) 1.5 mm, b) 3.5mm, c) 7 mm

Figure 3.9 shows that the maximum range of the strain state reaches its maximum in a plateau corresponding to a range of the value of the radius between 3.5 mm and 6.5 mm. However, the range of the strain state is just the result of the difference between the maximum and the minimum value of the strain states occurring in the specimen, therefore, it doesn't take into account the heterogeneity of the strain state, i.e. their distribution in the specimen, and thus, the diversity of the mechanical information obtained, which is on the other hand considered by the standard deviation of the strain state.

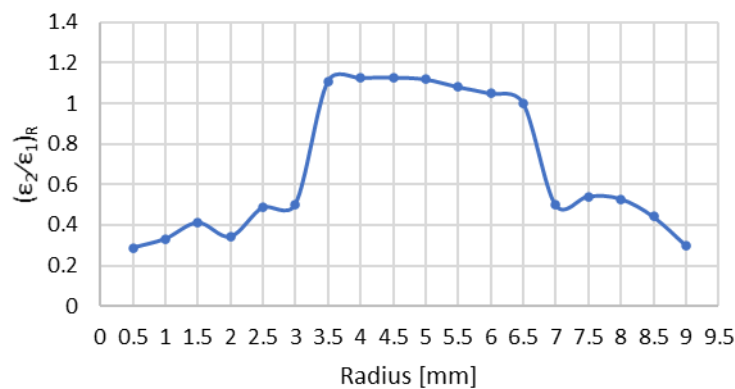


Figure 3.9 - Distribution of $(\epsilon_2/\epsilon_1)_R$ as a function of the radius

The heterogeneity of the strain levels increases until a maximum at 3.5 mm radius. After that, it slightly decreases (see Figure 3.10).

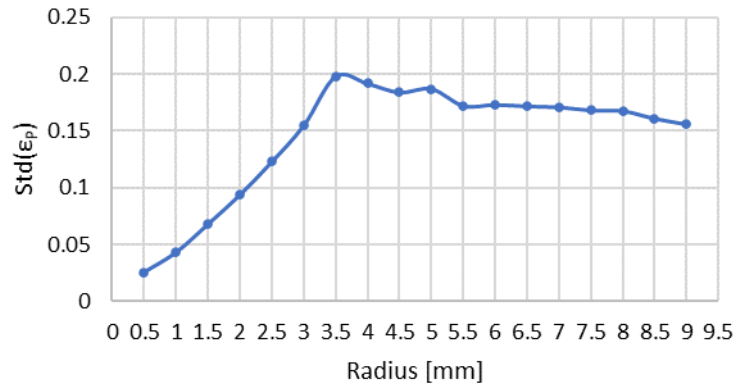


Figure 3.10 - Distribution of $Std(\epsilon_p)$ as a function of the radius

From Figure 3.11, it can be stated that a maximum is attained for the 7.5 mm radius, then it drops.

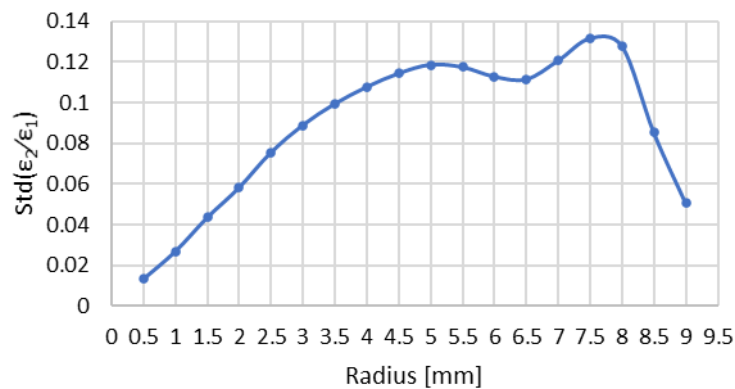
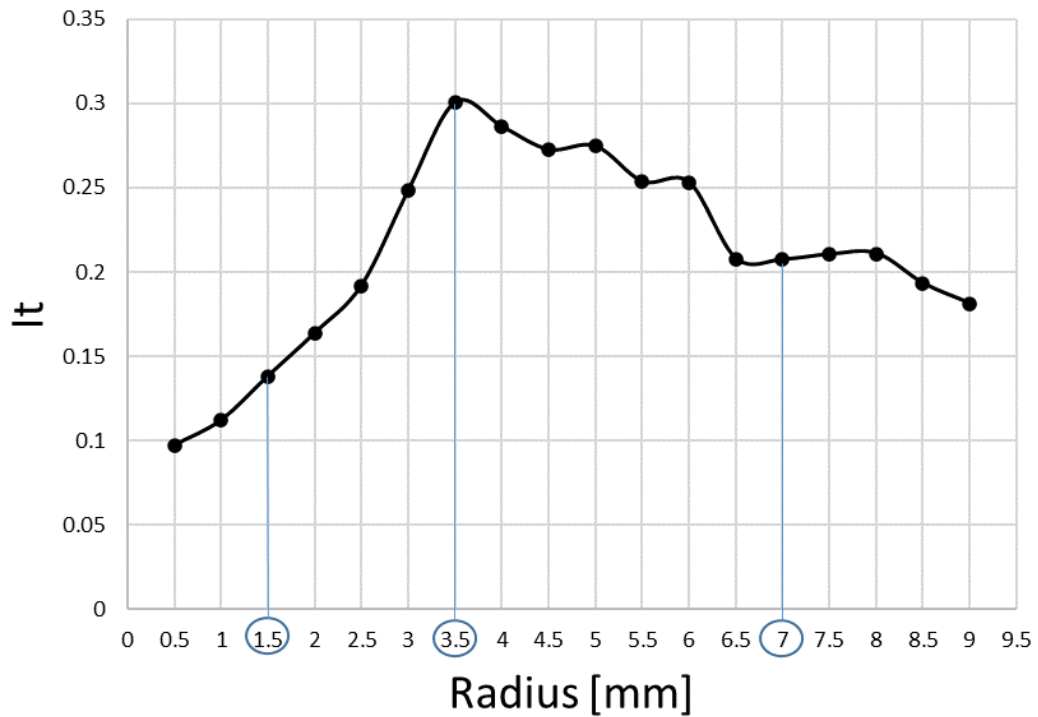


Figure 3.11 - Distribution of $Std(\epsilon_z/\epsilon_1)$ as a function of the radius

In the following graph the variation of the I_T indicator is represented as a function of the radius. As already discussed, a larger value of I_T leads to a better characterization of the material. Therefore, it can be stated that a specimen with a 3.5 mm radius of the notches should be adopted for inverse identification.

Figure 3.12 – Trend of I_T as a function of the radius

In addition to the optimal radius, two radii with a pretty lower value of the I_T indicator are chosen for comparison.

Figure 3.13 reports three histograms related to the three radii of the hole. The histograms show the number of elements subjected to each value of plastic deformation. The amplitude of the bell characterizing the histogram is closely related to the standard deviation of the plastic strains, and thus, to the heterogeneity of the strain levels. In fact, the larger the amplitude, the higher the standard deviation, and the greater the heterogeneity.

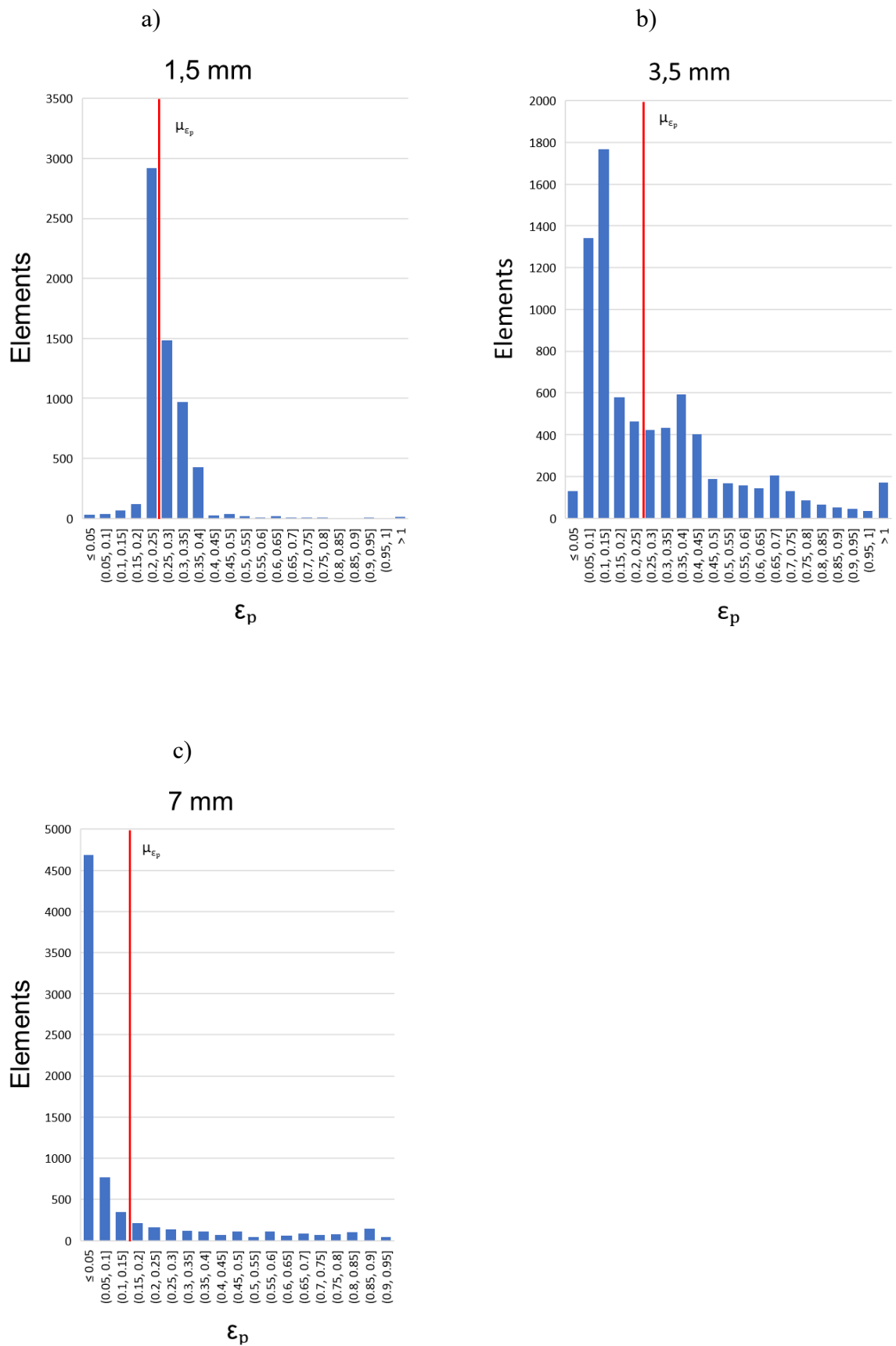


Figure 3.13 - Histograms showing the number of elements subjected to the same value of plastic strain with radius of the notch (a) 1.5 mm, (b) 3.5 mm, (c) 7 mm

The same statements made for the strain levels are also valid for the strain states. In this case the histograms show the number of elements subjected to each strain state characterizing the gauge area (see Figure 3.20). If the majority of elements present similar (ϵ_2/ϵ_1) values, a lower $Std(\epsilon_2/\epsilon_1)$ is obtained since the majority of the elements is close to the mean value $\mu_{\epsilon_2/\epsilon_1}$.

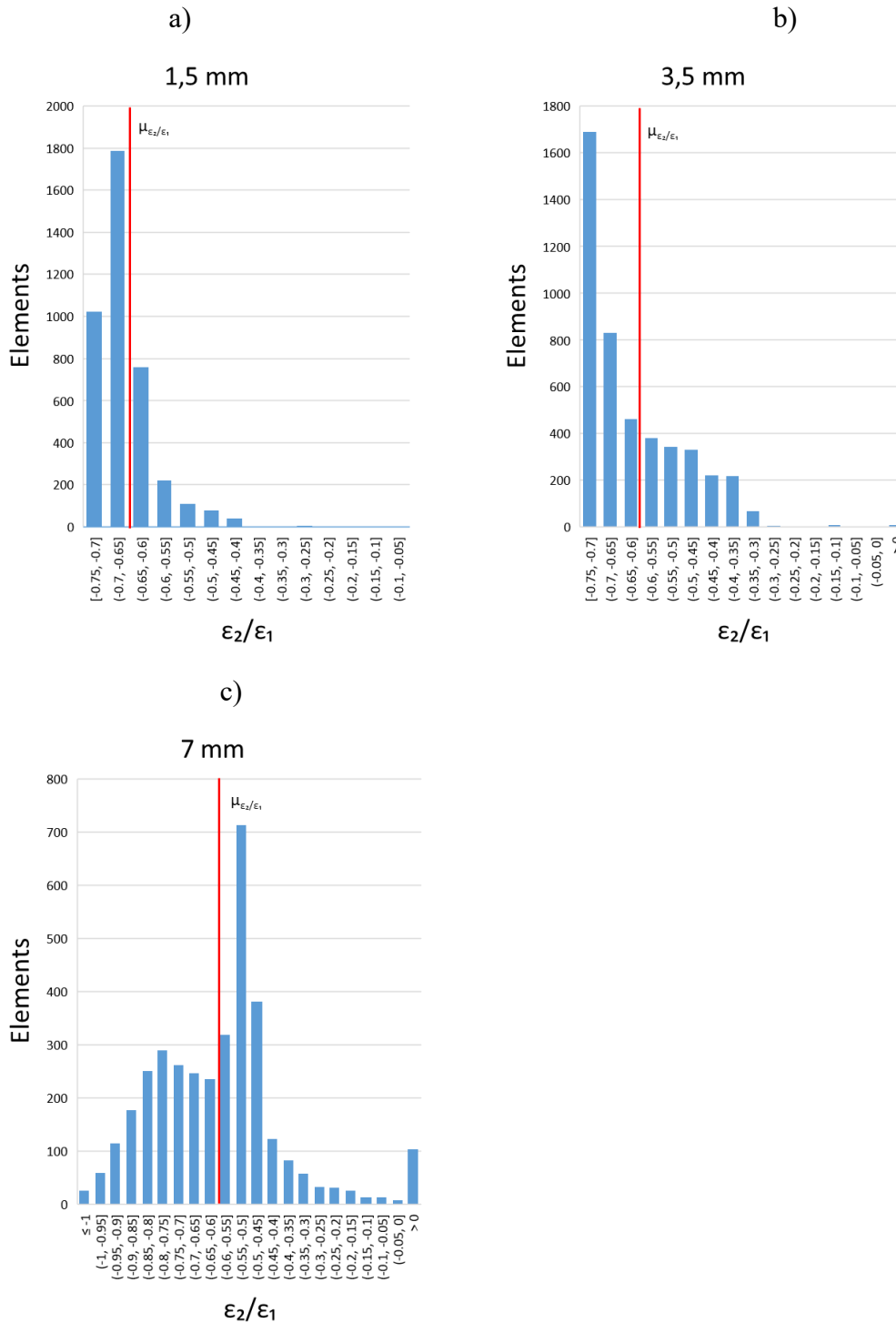


Figure 3.14 - Histograms showing the number of elements subjected to the same strain state with radius of the notch of (a) 1.5 mm, (b) 3.5 mm, (c) 7 mm

Another approach to analyze the variation of the heterogeneity of the strain state is plotting the strain states related to different values of the radius (see Figure 3.15). A larger scatter of the strain states plot corresponds to a bigger value of the standard deviation and, therefore, to a higher heterogeneity of the strain state.

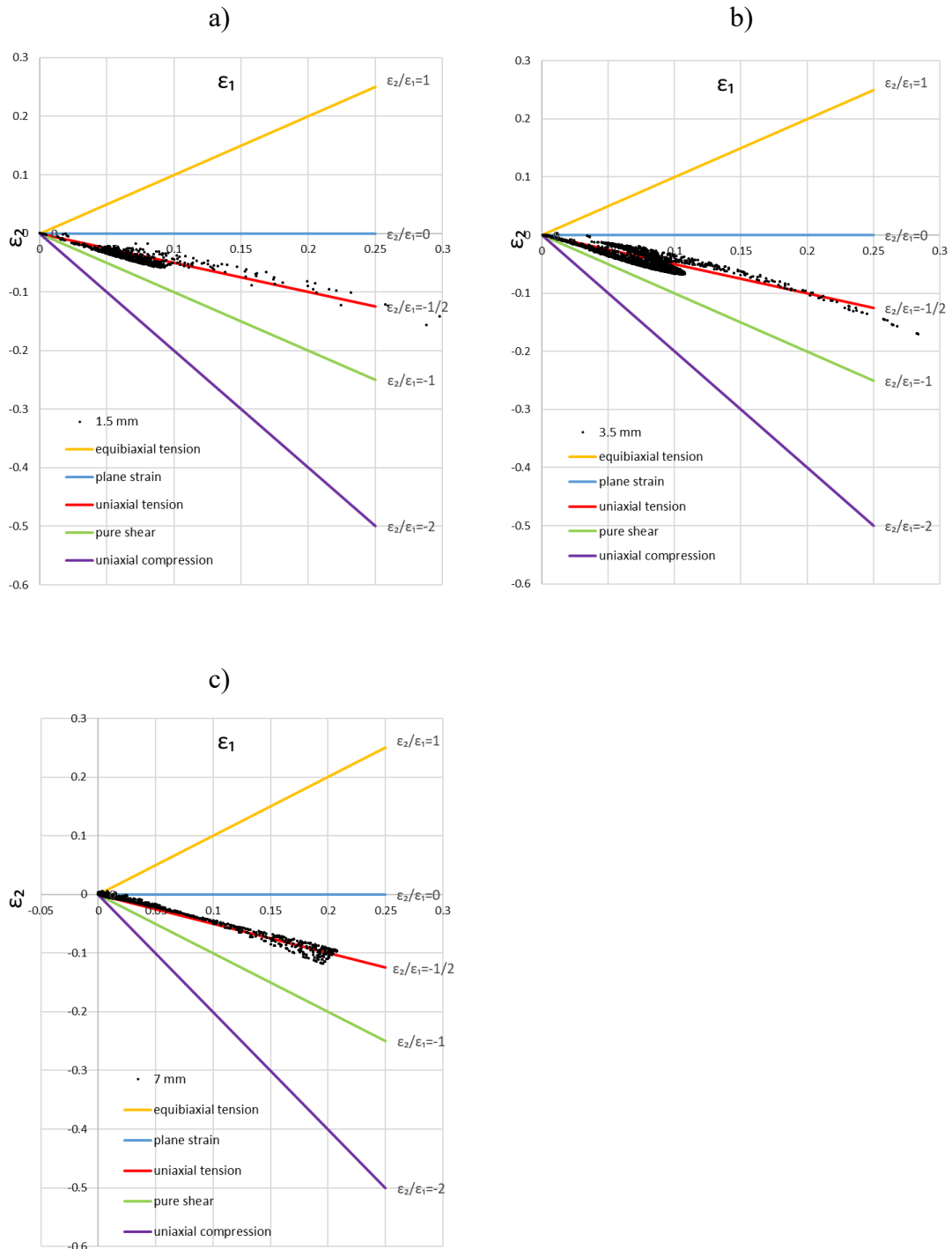


Figure 3.15 - Strain states of a specimen with a radius of the notch of (a) 1.5 mm, (b) 3.5 mm and (c) 7 mm

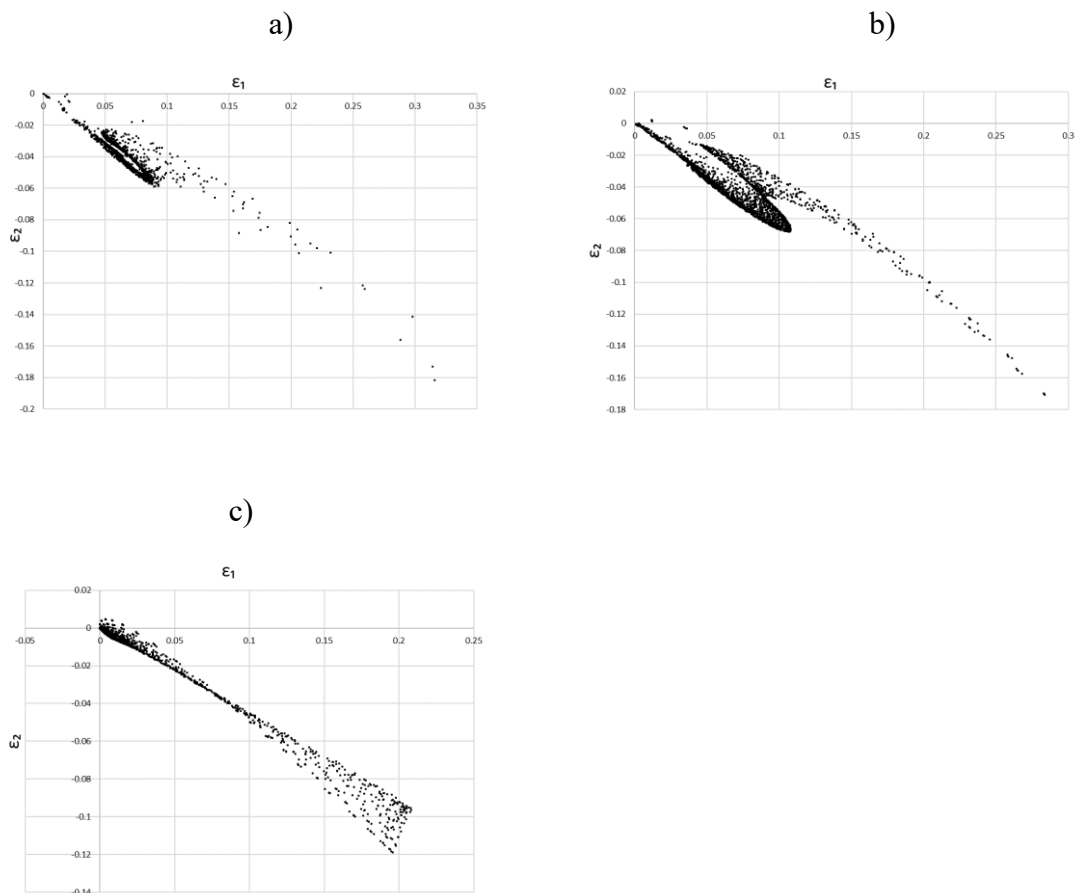


Figure 3.16 - Strain states of a specimen with a radius of the notch of (a) 1.5 mm, (b) 3.5 mm and (c) 7 mm

3.3 Topology Optimization

3.3.1 Definition and applications

The efficient use of materials is a relevant feature in many different fields. The aerospace industry and the automotive industry for example, apply sizing and shape optimization to the design of structures and mechanical elements. Shape optimization is also used in the design of electromagnetic, electrochemical and acoustic devices. The optimization of geometry and topology of structural lay-out has great impact in the performance of structures, and the last decade has seen a great amount of work in this important area of structural optimization. This has mainly been favored by the success of the material distribution method for generating optimal topologies of structural elements. The material distribution method for topology design has demonstrated its potential in a large number of case studies. Also commercial design Software have now been available for a number of years and the method is standard

technology in many industries. Topology Optimization (TO) has been recently adopted for a wide range of structural problems, e.g., free and forced vibrations, buckling, stress constraints, pressure loads, material design, design of supports, crashworthiness, biomechanics, etc. Moreover, new areas are today included in the problems that can be handled, such as electrothermal actuators, MEMS, Stokes flow problems, piezoelectric transducers, electromagnetic, and band gap structures [27]. As previously discussed, the I_T parameter is a quantitative indicator than enables to rate and rank different mechanical tests used to characterize the material behavior of sheet metals. The concerned parameter can be applied to design new heterogeneous experiments enabling to attain a higher quality and a more robust and reliable material characterization [26, 28]. In the previous section, the variation of I_T as a function of the radius of the notches has been evaluated. However, it would be interesting to investigate the optimal shape of the specimen that maximizes the concerning parameter, by analyzing all the possible geometrical combinations. For this purpose, Topology Optimization can be adopted. The goal of TO is to find the optimal layout of a structure within the specified design space. Differently from the size and shape optimization techniques, Topology Optimization does not require an initial layout of the design. The key merit of Topology Optimization over conventional size and shape optimization is that the former can provide more design freedom, leading to the creation of more innovative and highly efficient designs.

Several Topology Optimization methods have been proposed so far, e.g., density based methods (Bendsøe 1989 [29]; Zhou and Rozvany 1991 [30]; Bendsøe and Sigmund 2003 [27]), evolutionary structural optimization methods (BESO; Xie and Steven 1993 [31], 1997 [32]), level-set method (LSM; Sethian and Wiegmann 2000 [33]; Wang et al. 2003 [34-35]; Allaire et al. 2004 [36]), hybrid cellular automaton (Tovae et al. 2004 [37]) and phase field method (Bourdin and Chambolle 2003 [38]). All the methods mentioned are based on finite element analysis (FEA), therefore, the design domain is discretized into a number of finite elements [39]. However, the most popular approach, which is also implemented in the commercial Software FEMtools [40], is the SIMP (Solid Isotropic Material with Penalization) approach, a density-based method. The topology optimization starts from a continuous model of the design space and, using an iterative method, the optimization process removes or redistributes the material that is not efficiently used, until a pre-defined volume fraction is left. The resulting design

provides the optimal material distribution for the considered application. Topology optimization can sometimes lead to very surprising designs. Nonetheless, a further refinement of the design might be needed, e.g., re-working the design in CAD and re-meshing, or directly smoothing the mesh obtained by Topology Optimization. To run a Topology Optimization, it is necessary to define the design space, which represents the domain of material available to optimize the layout of the design. The design space is subdivided into an active and a passive domain. The passive domain includes the areas where the material cannot be removed. Whereas the active domain comprises the areas which can be reshaped in order to obtain the optimal design for the desired purpose [41].

Solving a Topology Optimization problem consists of the following five steps:

- Creating an FE-model of the design space;
- Applying the loads and boundary conditions of the design space;
- Defining the element sets for active and passive regions;
- Defining the manufacturing constraints, e.g., casting, extrusion, symmetry constraints;
- Launching the topology optimizer.

Figure 3.17 shows the optimization process implemented in FEMtools.

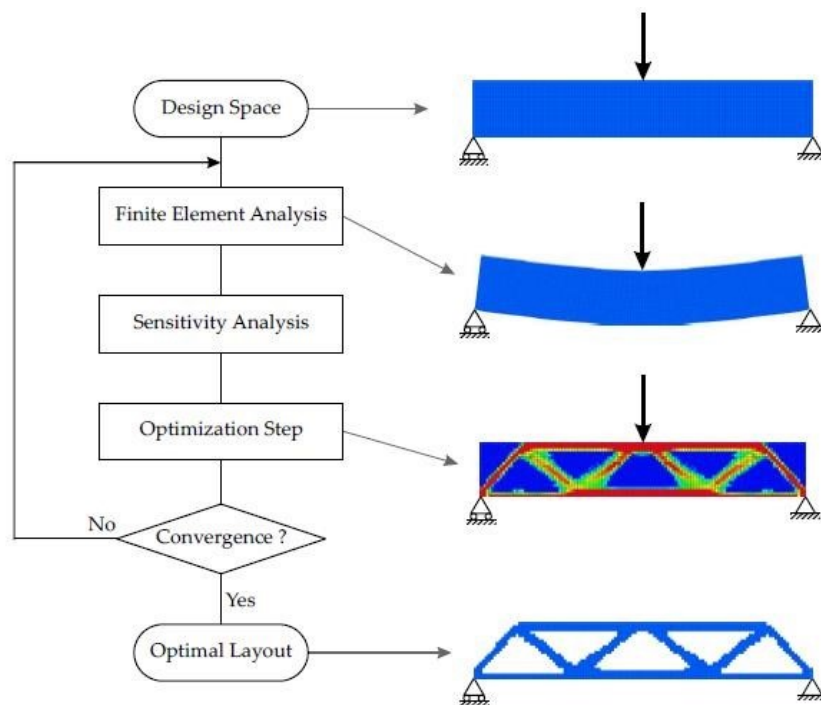


Figure 3.17 - Flow chart of the topology optimizer functioning for minimum static compliance design

The goal of this research is to find the optimal shape of the specimen to be used in the tensile test maximizing the I_T indicator, which is computed considering the principal strains of each element of the mesh. This means that the material should be removed and/or redistributed in order to maximize the concerned indicator. However, commercial topology optimizer tools, e.g., FEMtools, are currently able to solve only a limited number of design problems. The most common are [41]:

- Minimum Static Compliance Design – the design with the highest global stiffness for the considered load and volume fraction;
- Maximum Fundamental Eigenvalue Design – the Topology Optimization for maximizing a natural frequency in a structure;
- Minimum Dynamic Compliance Design – the design with the lowest response for a given frequency.

All these design problems are based on algorithms, which aim at minimizing or maximizing a certain cost function. Since no studies have been previously conducted on Topology Optimization related to the I_T indicator, further research would be needed to write new algorithms or adapt the old ones. In this case, the cost function to maximize would be I_T . Moreover, FEMtools takes into account only elastic material properties, e.g., Young's modulus E and Shear modulus G . However, plasticity as well as elasticity would be required to describe the material behavior, thus, also the use of plastic material properties should be included.

3.3.2 Topology Optimization applied to I_T indicator

3.3.3.1 Feasibility study

The material parameters are usually identified from a set of mechanical tests, such as uniaxial tensile test, simple shear test and classical biaxial test, which develop quasi-homogeneous strain fields. Nonetheless, when constitutive models are characterized by a large number of material parameters to be determined, the identification process becomes expensive and time consuming. Thus, designing non-homogeneous tests has assumed great relevance since heterogeneity of the stress and strain fields leads to a larger amount of information, and therefore, to a better quality of the identified parameters [26, 28]. It should be of interest to find the optimal specimen shape using Topology Optimization in order to maximize the I_T indicator. The bigger I_T , the larger

the heterogeneity of the strain field and, consequently, the mechanical characterization of sheet metals is enhanced.

In the following lines, a brief discussion regarding Topology Optimization related to the I_T indicator and suggestions for further research is presented. Evaluations have been made using the SIMP approach. The concerned method links an element relative density (ρ_e) to every active element of the design space. The relative element densities are real numbers that can take any value between 0 and 1. By multiplying the stiffness matrix of the active elements with their corresponding element relative density, the stiffness can be varied in a continuous way and assumes the expression:

$$[k] = \rho_e^p [k_e] = [k(\rho_e)] = [k(\rho_e(i, j))] \quad (3.8)$$

where p is the exponential penalty factor, while i and j define the number of the considered element along the x and y directions. In this way, the stiffness of the element is expressed as a function of the corresponding element relative density. The global stiffness matrix is obtained by combining the stiffness matrices of all the elements of the structure:

$$[K] = [K(\bar{\rho}_e(i, j))] = [K(\rho)] \quad (3.9)$$

where $\bar{\rho}_e$ stands for the vector containing the relative densities of all the elements of the structure and $[K]$ is the global stiffness matrix of the structure. Since the global stiffness matrix is dependent on the relative densities and the vector of nodal loads $\{F\}$ is constant, the vector of nodal displacements $\{U\}$ will also be a function of the relative densities:

$$\{U(\rho)\} = \frac{\{F\}}{[K(\rho)]} \quad (3.10)$$

Strains $\{\varepsilon\}$ can be determined knowing displacements at nodal points, consequently, also the strain field is a function of the relative densities:

$$\{\varepsilon(\rho)\} = [B]\{U(\rho)\} \quad (3.11)$$

where the matrix $[B]$ is the displacement differentiation matrix.

Once the local strains are known, the principal strains and the equivalent plastic strains, i.e. $\{\varepsilon_1(\rho)\}$, $\{\varepsilon_2(\rho)\}$ and $\{\varepsilon_{eq}^{pl}(\rho)\}$ can be also computed. The following step consists of the quantification of the I_T parameter, which, since derived from the strain distributions, is dependent on the relative densities:

$$I_T(\bar{\rho}_e(i, j)) = I_T(\rho) = w_{r1} \frac{\text{Mean}[\text{Std}(\varepsilon_2(\rho)/\varepsilon_1(\rho))]}{w_{a1}} + w_{r2} \frac{(\varepsilon_2(\rho)/\varepsilon_1(\rho))_R}{w_{a2}}$$

$$+w_{r3} \frac{\text{Mean}[\text{Std}(\varepsilon_p(\rho))]}{W_{a3}} + w_{r4} \frac{\varepsilon_{p,MAX}(\rho)}{W_{a4}} + w_{r5} \frac{Av_{\varepsilon p}(\rho)}{W_{a5}} \quad (3.12)$$

In this way, I_T is expressed as a function of the relative density distribution of the structure. The developed Topology Optimization approach aims at maximizing the strain field information provided by the heterogeneous test. Therefore, the value of the I_T indicator should increase during the optimization process. However, as the optimization process was conceived for a minimization, the cost function can be defined in order that its minimization means the maximization of I_T . Hence the cost function can be written as:

$$C = 2 - I_T \quad (3.13)$$

Because of the complex dependency of I_T on the relative densities, the sensitivity of the objective function with respect to the relative density can be expressed as:

$$\frac{\partial C}{\partial \rho} = \frac{\partial I_t}{\partial \rho} \quad (3.14)$$

The latter expression cannot be found analytically, therefore, a numerical method to calculate the derivative would be required. In this case, the sensitivity would be calculated as the variation of I_T due to a density perturbation:

$$\frac{\partial I_t}{\partial \rho} = \frac{\Delta I_t}{|\Delta \rho|} \quad (3.15)$$

where $|\Delta \rho|$ represents the module of the total density perturbation, that is obtained considering the density perturbations to which every element of the structure is subjected:

$$|\Delta \rho| = \sqrt{\sum_{e=1}^N (\bar{\rho}_e^k - \bar{\rho}_e^{k-1})^2} \quad (3.16)$$

Where $\bar{\rho}_e^k - \bar{\rho}_e^{k-1}$ represents the difference between the vector of relative densities at the iteration k and the one at the previous iteration $k-1$. Although this method seems to be the solution for the raised problem, it is not mathematically applicable, unless a suitable way to update the densities for each element and at each iteration is found. This problem is mainly due to two reasons:

- The I_T parameter is a global parameter, which means that it is defined considering the entire structure. It is not achievable to determine I_T for each finite element of the structure;
- The derivative of I_T with respect to the relative densities cannot be analytically computed.

For a better understanding of these statements a part of the code written by O. Sigmund for structural optimization [42] is described below:

$$c(x) = U^T K U = \sum_{e=1}^N (\rho)_e^p u_e^T k_0 u_e \quad (3.17)$$

where $c(x)$ is the cost function to minimize. The sensitivity of the objective function is found as:

$$\frac{\partial c}{\partial \rho_e} = -p(\rho_e)^{p-1} u_e^T k_0 u_e \quad (3.18)$$

A heuristic scheme is used to update the element densities:

$$x_e^{\text{new}} = \begin{cases} \max(\rho_{\min}, \rho_e - m), & \text{if } \rho_e B_e^\eta \leq \max(\rho_{\min}, \rho_e - m) \\ \rho_e B_e^\eta, & \text{if } \max(\rho_{\min}, \rho_e - m) < \rho_e B_e^\eta < \min(1, \rho_e + m) \\ \min(1, \rho_e + m), & \text{if } \min(1, \rho_e + m) \leq \rho_e B_e^\eta \end{cases} \quad (3.19)$$

where m is a positive move-limit, η ($=1/2$) is a numerical damping coefficient and B_e is found as:

$$B_e = \frac{-\frac{\partial c}{\partial \rho_e}}{\lambda \frac{\partial V}{\partial \rho_e}} \quad (3.20)$$

with λ a Lagrangian multiplier that can be found by a bi-sectioning algorithm.

3.3.3 I_T indicator applied to the specimen with notches

In this work a simple way has been used for the design of the specimen. A displacement-driven model has been created in Abaqus for each value of the radius included in the range 0.5 - 9 mm with a 0.5 mm increment. For each radius, the displacement value that provides necking is found in a model called model-0. An equivalent model, called model-1, has been created applying the displacement values found in model-0, so that the calculation stops when necking occurs, according to

Equation (1.45b). Finally, the indicator value is calculated from the .odb file using a python script.

Chapter 4

Inverse identification of anisotropic yield functions using a tensile test and DIC

4.1 FE Model

The specimen with notches is utilized for inverse identification (see Figure 4.1). Abaqus/Standard is used to build up the FE model, using shell elements (S4R) with an average dimension of 0.6 mm, and a static general analysis is adopted to perform the simulation. Regarding the material properties, a Young's modulus E of 200 GPa and a Poisson's ratio ν of 0.3 are assumed to describe the elastic-isotropic material behavior. The Hill'48-r material model coupled with the Swift hardening law (see Table 3) are adopted to characterize the plastic anisotropy. Moreover, the material orientation is defined to identify the Rolling and the Transverse Directions in the FE model. Two FEMU approaches are used: the displacement-driven approach, where the FE simulation is performed using, as boundary conditions, the displacement components, fitted with polynomial functions, that lead to a 20/30% plastic deformation level; the force-driven approach, where the FE simulations are performed applying shell edge loads to the ends, corresponding to the ones measured in the actual experiment.

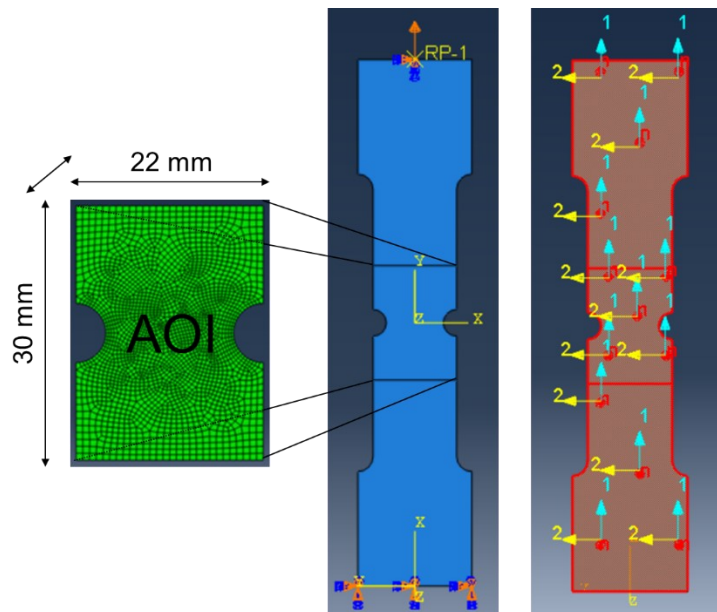


Figure 4.1 - FE model: shape of the specimen, AOI, mesh, material orientation, boundary conditions (clamping and load)

4.2 Material identification using a VE

A first identification through Virtual Experiment has been conducted to compare the results using the three radii: 1.5 mm, 3.5 mm, 7 mm. As expected, the optimal radius gave the best results, as shown in table 6.

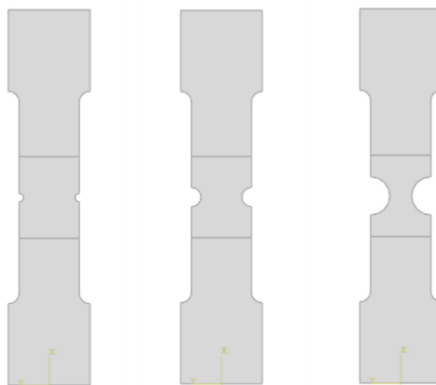


Figure 4.2 – Specimens with three different radii: 1.5 mm, 3.5 mm, 7 mm

	Traditional experiments	1.5 mm	3.5 mm	7 mm
r0	1.645	1.468126	1.621583	1.216039
r45	1.18	0.852733	1.307271	2.097882
r90	2.09	1.234349	2.187647	17.39974

Table 6 – Inversely identified r-values for the three radii

From this moment on, the study has been focused on Virtual Experiments on the 3.5 mm radius specimen. A reference identification with the following parameters has been conducted:

- Tension along RD: R0
- 1 LS
- 2D DIC: only front camera
- Default DIC parameters given by the software: SS = 21, ST = 10, SW = 7, VSG = 81
- Average speckle size = 5 pixels (Figure 4.3)

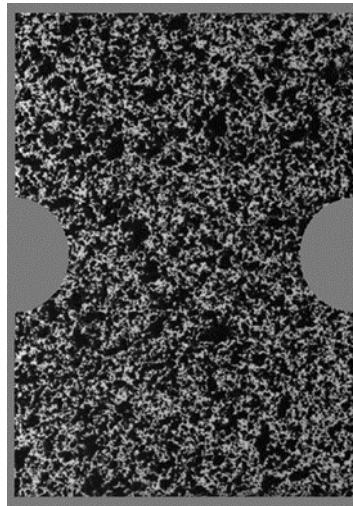


Figure 4.3 – Digital image of the AOI with a 5 pixels average speckle size

In Figure 4.4 two loci are shown: the black one refers to the Hill model and is plotted using the r-values retrieved from traditional experiments; the blue one is plotted using the identified material parameters.

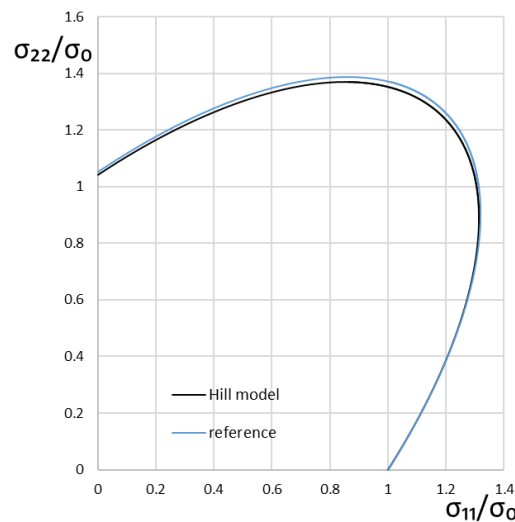


Figure 4.4 – Hill'48 loci: model (black), identified (blue)

The identification already seems to be good in the vicinity of the uniaxial tension along the RD and the plane strain state.

Starting from this experiment, many other identifications have been conducted in order to assess the influence of some parameters.

The influence of DIC settings is evaluated by comparing different VSG values (Figure 4.5)

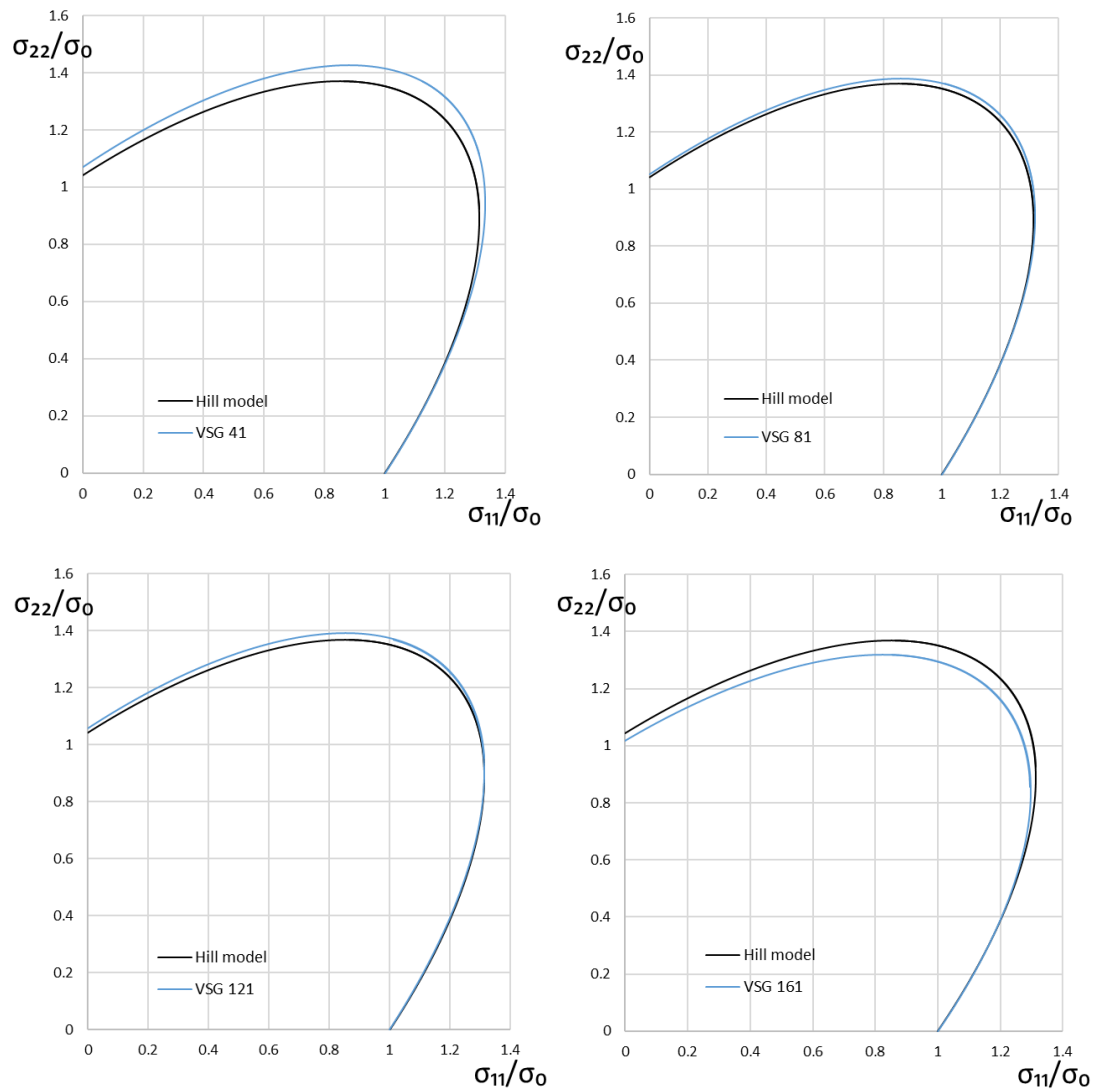


Figure 4.5 – Hill loci with four different VSG values

It turned out the best identification is obtained using a VSG equal to 81, which is the one used in the reference identification.

The influence of the noise included during the numerical deformation process turned out to be not relevant (Figure 4.6). The noise is defined as the difference in grey level between two still images.

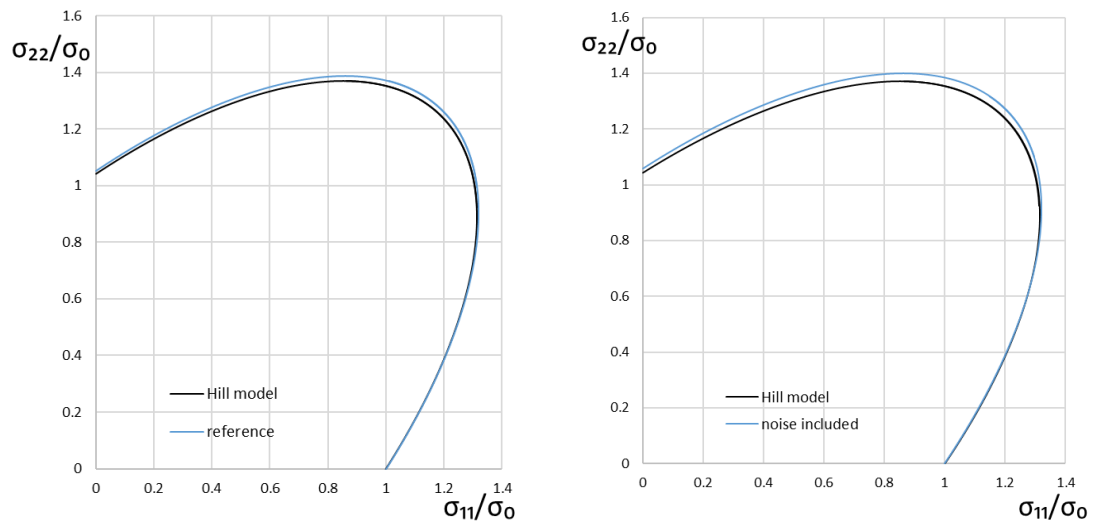


Figure 4.6 – Hill loci without noise and with noise included in the numerical deformation

In this case, using multiple Load Steps did not improve the identification (Figure 4.7)

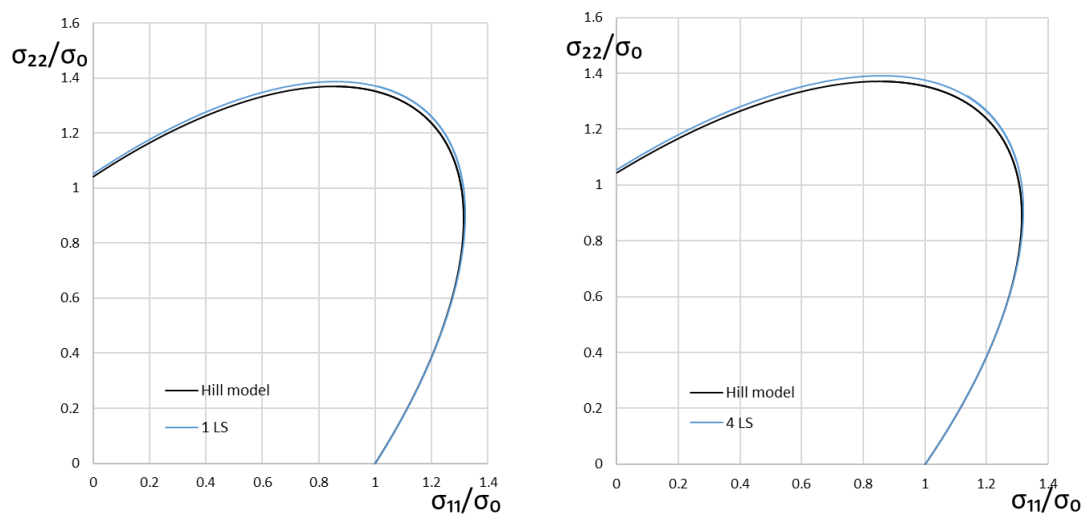


Figure 4.7 - Hill loci using 1 LS or 4 LS

The influence of the .force file is null, this means that, since Hill'48 is based on strains, the .force file is not needed. It would be necessary if a more accurate yield criterion was used in Abaqus, because it would be difficult to compare the experimental and the numerical results (for example Yld-2000 in Abaqus and Hill'48 in FEMid).

The influence of the projection error introduced using Stereo DIC is shown in figure. There's a very good correspondence between the two loci, so a projection error of 0.02919 is negligible.

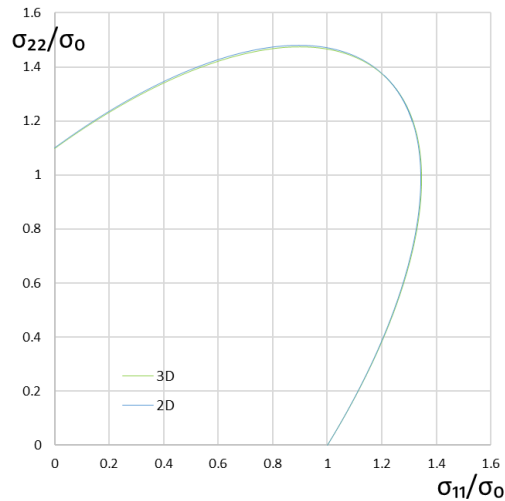


Figure 4.8 – Hill loci from 2D-DIC and 3D-DIC

The influence of the speckle pattern using two still images, with an average speckle size of 5 and 3 pixels respectively, appeared to be very significant.

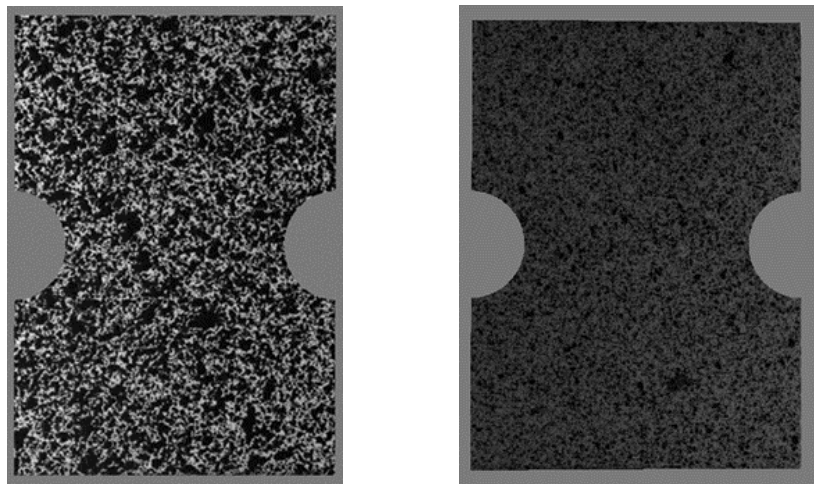


Figure 4.9 - Digital images of the AOI with a 5 and a 3 pixels average speckle size

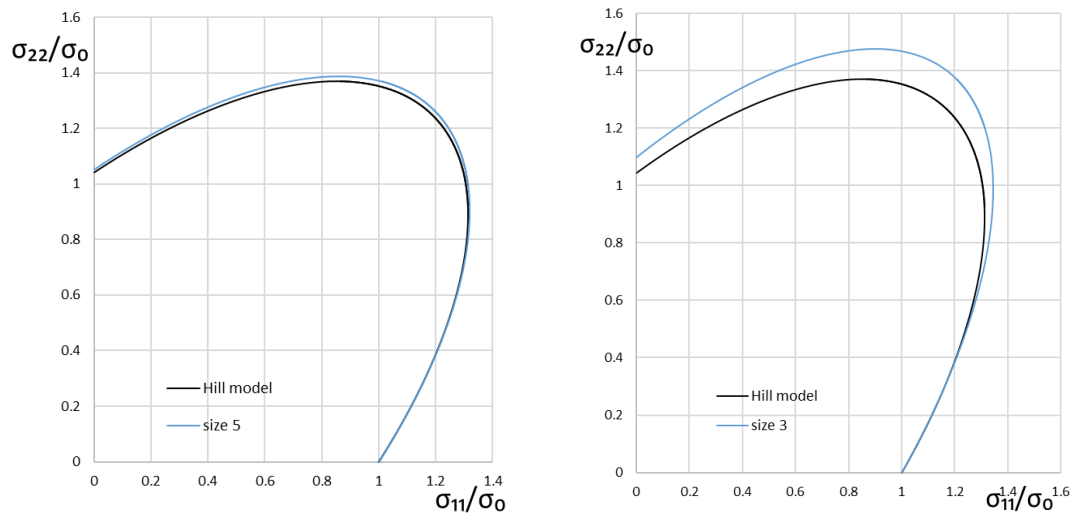
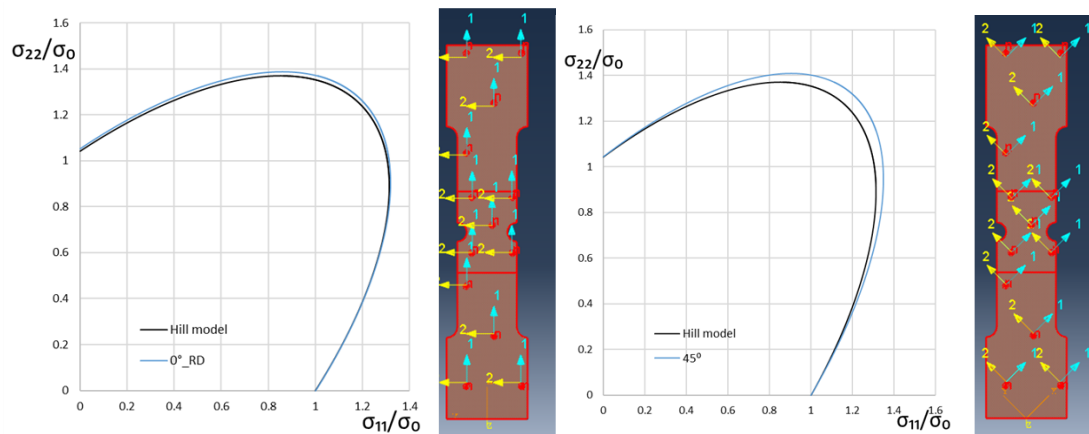


Figure 4.10 – Hill loci using different speckle patterns

A remarkable difference is evident in the results using a different speckle pattern, it must be considered that the DIC settings are closely related to the speckle size, hence in this case a smaller speckle size does not get along with the default DIC settings.

At the end, different identifications were done with a different material orientation (Figure 4.11)



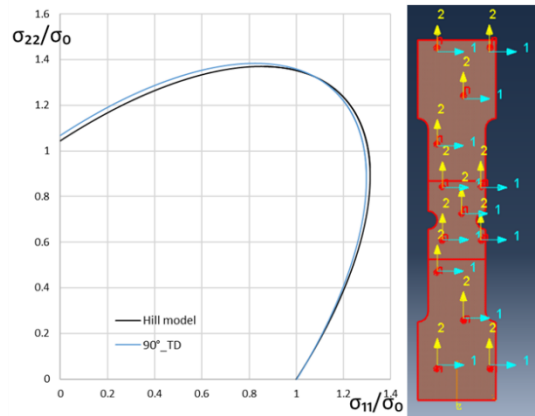


Figure 4.11 – Hill loci with different material orientation

The following considerations can be retrieved:

- For the case of material stretched along the RD, the identification is good in the region of locus in the vicinity of the uniaxial tension and plane strain states;
- For the case of material stretched in a direction tilted 45° to the RD, the identification is only right along the principal directions;
- For the case of traction along the TD, the identification is correct for the uniaxial and biaxial tension states.

Further studies should be done on the influence of the material orientation on other specimens.

It can be stated that the most influent parameters are the DIC settings, the speckle pattern, and the material orientation.

4.3 Material identification using a AE

A tensile machine with a maximum capacity of 10 kN is used to perform the tensile test. The two cameras used to perform the Stereo-DIC are located in front of the machine in order to measure the displacement and strain fields in the Area Of Interest (AOI). One camera is perpendicular to the target surface of the specimen, the other one is tilted 16° with respect to the first one. The speed of the test is set equal to 5 mm/min and the images are captured with a frequency of 1 Hz. Three tests are conducted for every radius: the optimal radius (3.5 mm) and two other radii which have a sufficiently lower heterogeneity level (1.5 mm and 7 mm). All the specimens are produced by waterjet cutting and they are characterized by a nominal thickness of 1 mm.

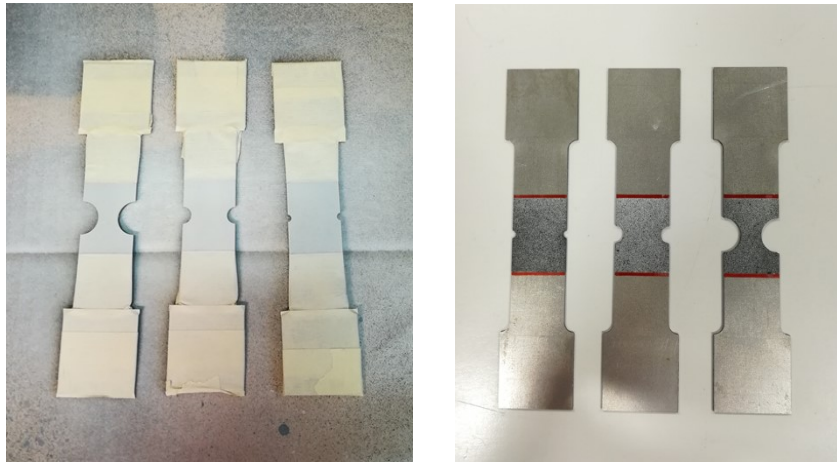


Figure 4.12 – Preparation of the specimens: creation of the speckle pattern

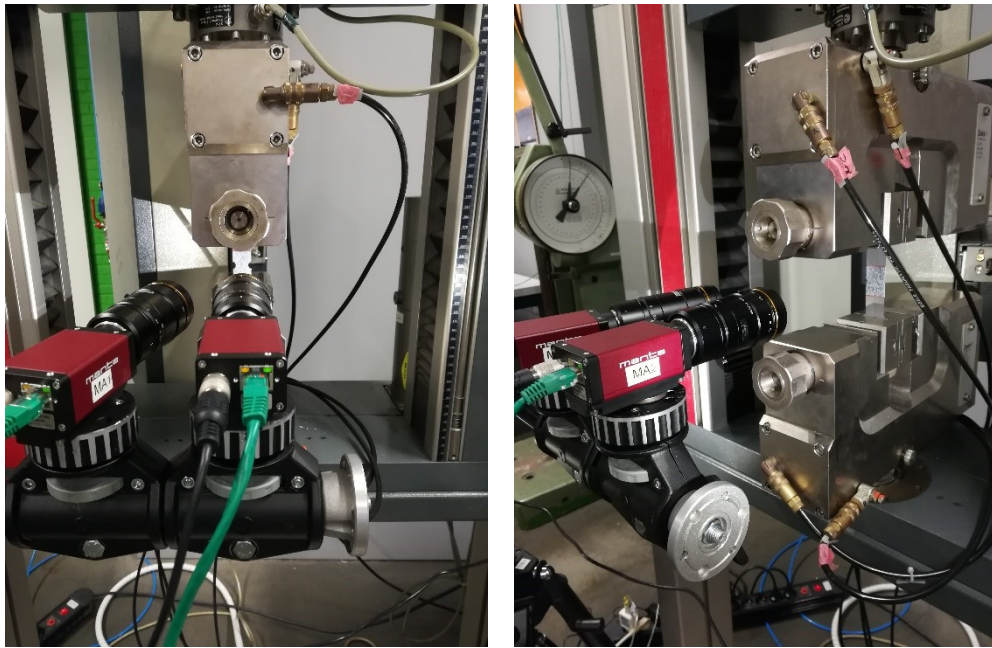


Figure 4.13 – Camera set-up: front and angled cameras

During the test, the tensile load is measured, and the signals are transmitted to an amplifier. The tensile load is directly synchronized with the DIC system, so every captured image is correlated with the corresponding load.

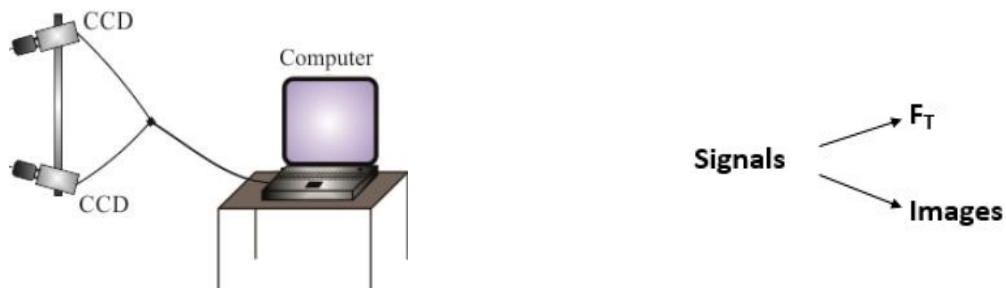


Figure 4.14 - Experimental set-up: DIC system and signals received

Using the conversion constant, the signal is converted from mV to kN:

$$F \text{ (kN)} = C \text{ (kN/}\mu\text{V)} V \text{ (mV)} 10^3 \quad (4.1)$$

where F is the load, C , equal to $0.01125 \text{ (kN/}\mu\text{V)}$, is the calibration constant and V is the voltage.

The tensile load-time curves are shown in Figure 4.15.

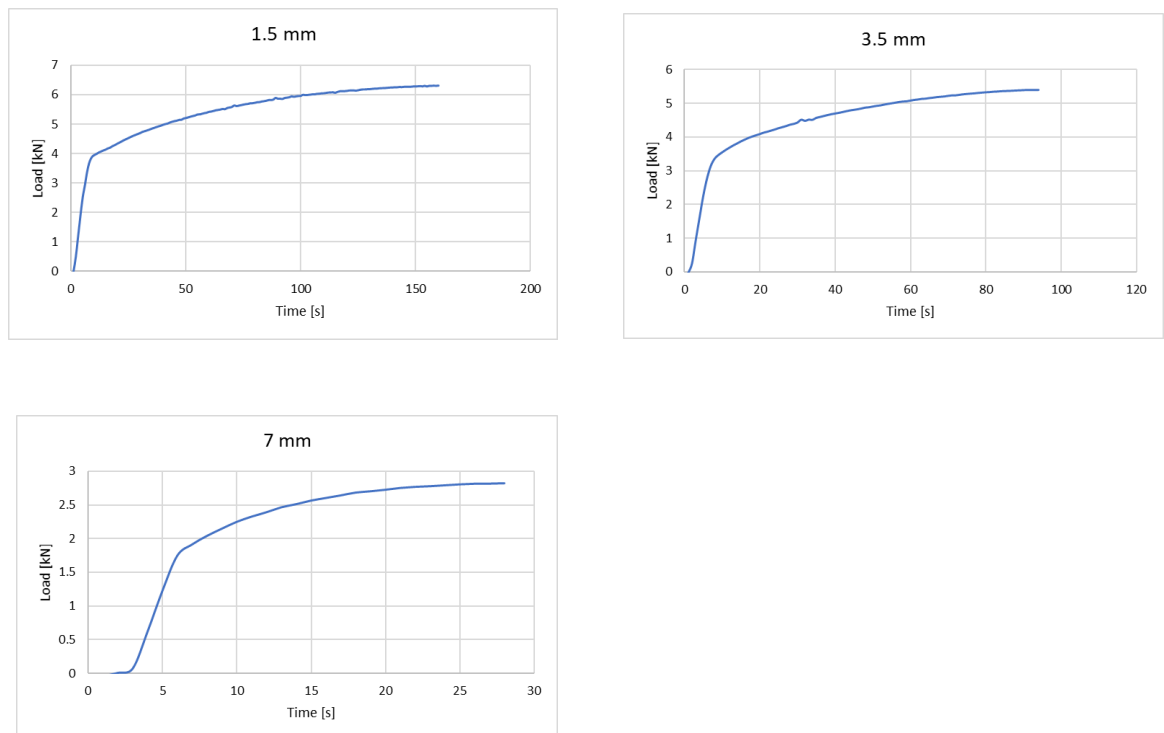


Figure 4.15 - Tensile load-time curves

The specimens are brought to fracture, obviously they exhibit different deformation levels and distributions (Figure 4.16). It must be said that for the 1.5 mm radius, only

one out of the three tests is valid because in the others errors were made while applying the paint.

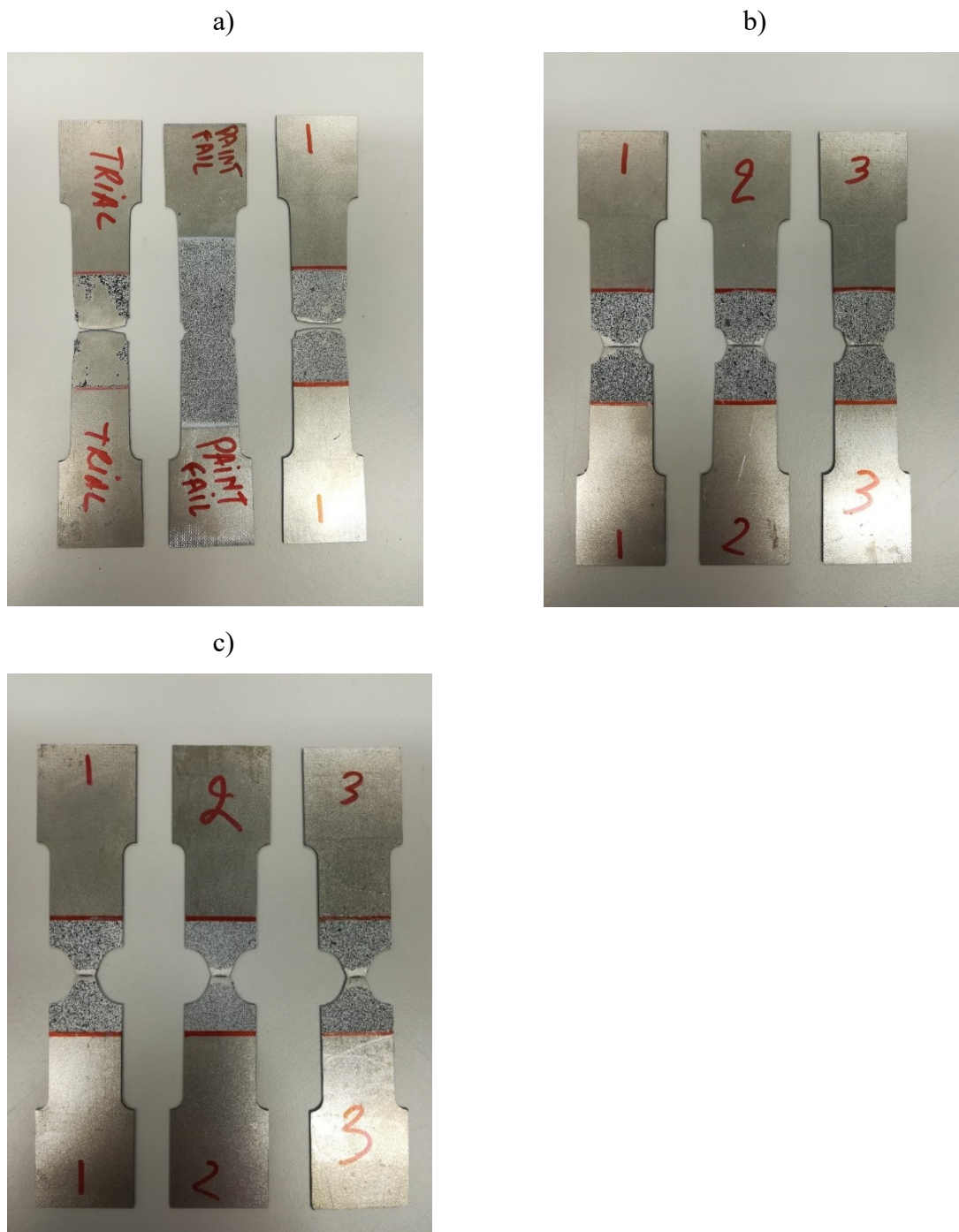


Figure 4.16 – Specimens at the end of the tests: different strain distribution are noticeable for the three radii. a) 1.5 mm b) 3.5 mm c) 7 mm.

4.3.1 Digital Image Correlation

4.3.1.1 Calibration process

Before starting the test, the DIC system is calibrated. For the calibration procedure, the calibration target 12 x 9 x 0.5, shown in Figure 2.3, is employed. Camera 1 is perpendicular to the target surface, while camera 0 is angled. In Table 7 and Table 8 the calibration parameters are shown.

	Camera 0	Camera 1
Fx [pixels]	5822.065	5773.331
Fy [pixels]	5781.577	5732.773
Fs [pixels]	0	0
K 1	-0.18459	-0.18731
K 2	3.29609	3.331229
K 3	-53.8006	-52.568
P1	0.001927	0.001927
P2	-0.00026	-0.00026
Cx [pixels]	1337.095	1356.241
Cy [pixels]	1119.851	1133.711

Table 7 - Calibration parameters related to camera 0 and camera 1

Tx [mm]	62.38445
Ty [mm]	-4.16722
Tz [mm]	20.80599
Theta [deg]	-1.26146
Phi [deg]	-15.767
Psi [deg]	-0.08616
Tx [mm]	62.38445

Table 8 - Relative positions between camera 0 and camera 1

A white uniform paint and a black speckle pattern on top of it are applied to the AOI of the specimens for the calibration and correlation processes (Figure 4.17).

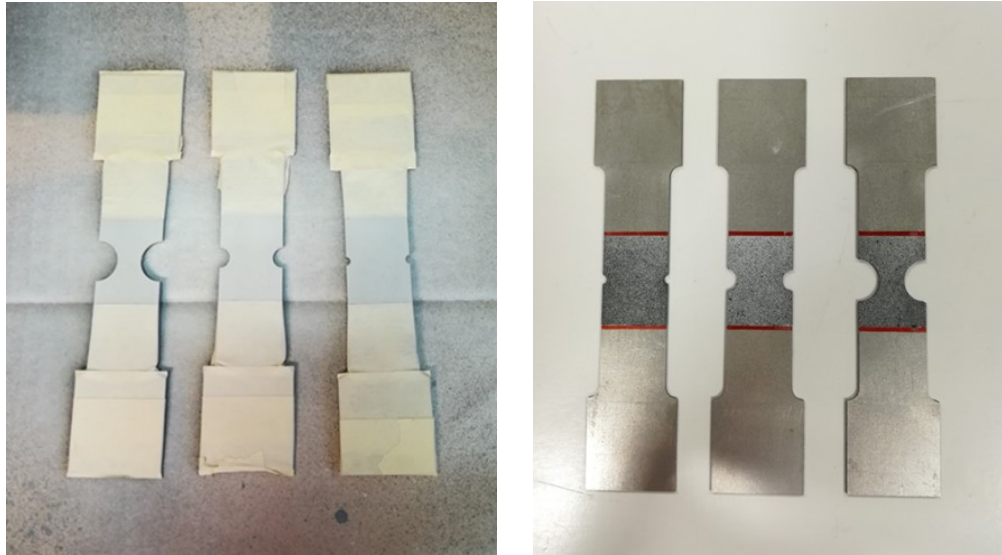


Figure 4.17 - Creation of the speckle pattern on the AOI

4.3.1.2 Performance analysis

Before starting the correlation process a Performance Analysis (PA) is conducted to analyze the influence that DIC parameters such as subset, step size and strain window have in the displacement and strain fields resulting from the correlation process. Therefore, the PA allows the optimal DIC settings to be found, leading to the best trade-off between accuracy and noise.

It can be stated that, adopting small values of step size, i.e. a larger number of measurement points, results in a higher accuracy and an increased noise effect. On the other hand, if large values are employed the noise effect is reduced, but less accuracy is attained due to the excessive smoothing of the displacement field. Similar statements can be made for the strain window size. In fact, it can be observed that employing an excessively large value of strain window size results in a relevant smoothing and averaging of the strain levels. Whereas, a small strain window size leads to more accuracy, but also noisy strain fields, with higher strain peaks, which, in some cases, are apparent strain peaks inside the material. Concerning the subset, the size should mainly be in accordance with the size of the speckles (refer to Chapter 2). The DIC settings adopted for the notched specimens are reported in Table 10.

	Subset (SS)	Stepsize (ST)	Strain Window (SW)	Polynomial order
Minimum	13	3	3	Q4
Maximum	19	5	11	Q8
Increment	2	2	4	

Table 9 – Performance Analysis

4.3.1.3 Correlation process

The correlation process is performed using the settings listed in Table 10.

Criterion	ZNSSD
Subset size	15
Step size	3
Interpolation	Bicubic Splines
Shape function	Affine
Prefiltering	Gaussian
Progress history	Spatial + Update
Strain Window	7
Virtual Strain Gauge	33
Strain interpolation	Q4
Strain convention	Log. Euler-Almansi

Table 10 - Optimal DIC settings from the PA

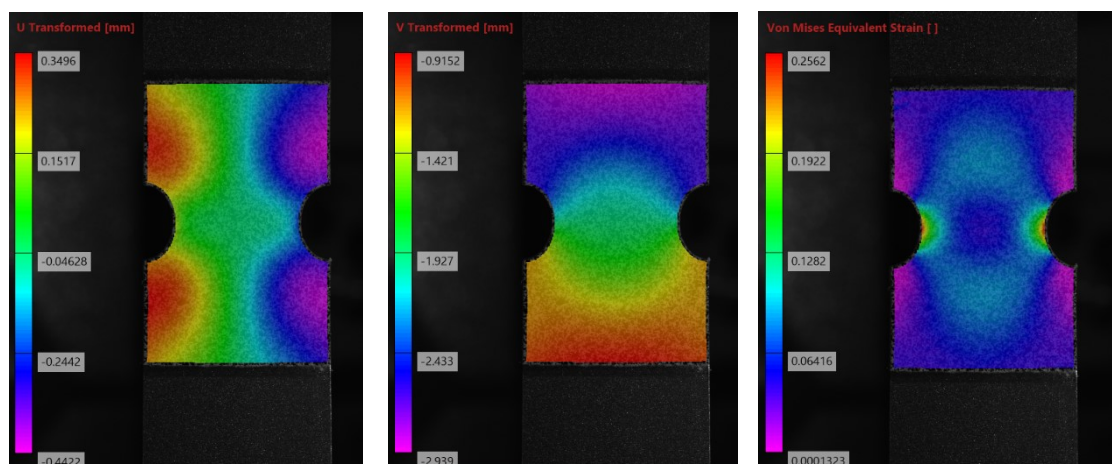


Figure 4.18 - Displacement and strain fields of the specimen obtained using DIC

4.3.2 Results

For the 1.5 mm radius, from the comparison between experimental and numerical results, it is noticeable a similarity in the strain distribution but a 5% difference in the strain level (Figure 4.19)

	Traditional experiments	1.5 mm_AE	1.5 mm_VE
r0	1.645	1.440446	1.468126
r45	1.18	0.844173	0.852733
r90	2.09	1.177569	1.234349

Table 11 - Identified r-values for the 1.5 mm radius: AE and VE

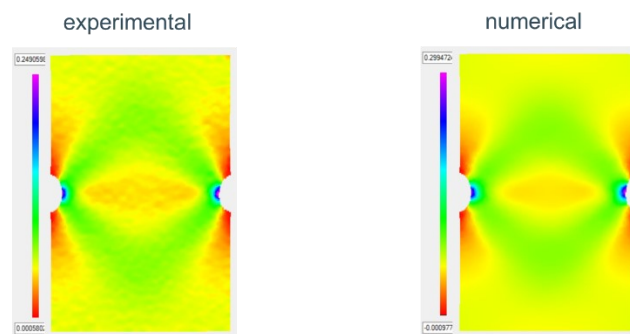


Figure 4.19 - Experimental and numerical strain fields for the 1.5 mm radius (AE)

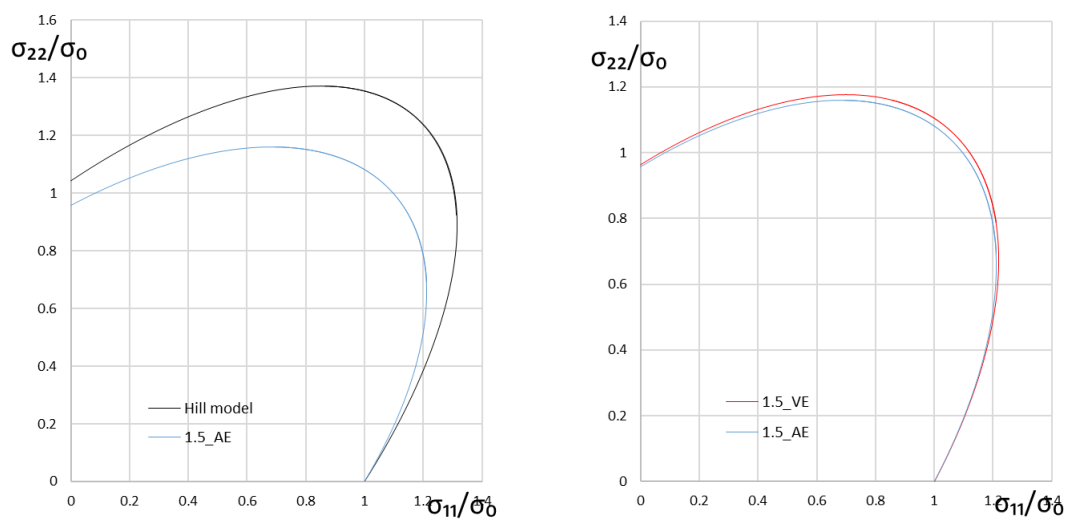


Figure 4.20 – Hill loci for the 1.5 mm radius (AE and VE)

Indeed, the difference between the two curves in the first graph is evident but, comparing the results from AE ad VE, a very good match of the loci is noticeable: this means the identification is correct either knowing the material model, which happens in the VE, or using real AE data. Hence, the difference with respect to the theoretical model must be due to the low heterogeneity level introduced by the 1.5 mm radius of the notches.

For the 7 mm radius, plasticity is strictly concentrated in the center of the specimen. Furthermore, both VE and AE gave erroneous results that are not comparable with the model, probably because Abaqus has problems in simulating load instability or localization

	Traditional experiments	7 mm_AE	7 mm_VE
r0	1.645	8.720361	1.216039
r45	1.18	0.109188	2.097882
r90	2.09	0.654658	17.39974

Table 12 - Identified r-values for the 7 mm radius: AE and VE

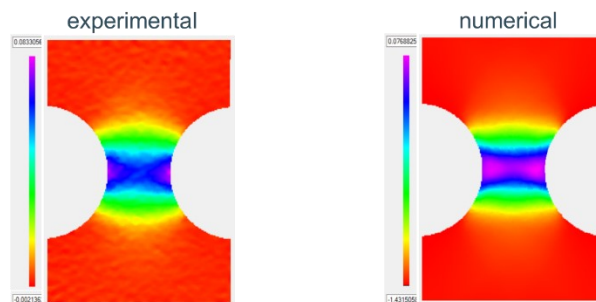


Figure 4.21 - Experimental and numerical strain fields for the 7 mm radius (AE)

For the 3.5 mm the results are very good, even better if 2 LS are used.

	Traditional experiments	3.5 mm_AE1	3.5 mm_AE2	3.5 mm_AE3	3.5 mm_AE1_2LS	3.5 mm_VE
r0	1.645	1.555699	1.614921	1.667827	1.566078	1.650223
r45	1.18	1.17897	1.1.193944	1.183471	1.103984	1.179025
r90	2.09	2.710426	2.470269	2.20969	2.113101	2.059449

Table 13 - Identified r-values for the 3.5 mm radius: AE and VE

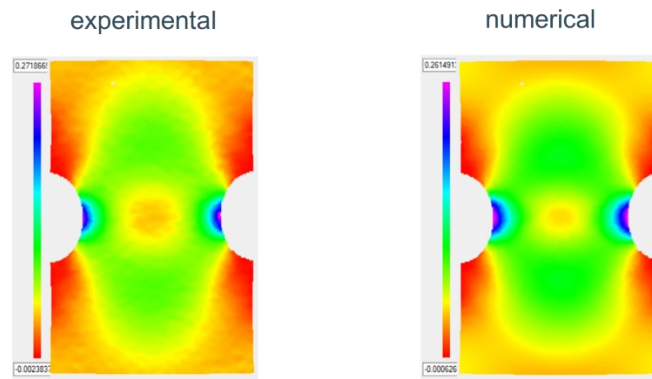


Figure 4.22 - Experimental and numerical strain fields for the 3.5 mm radius (AE)

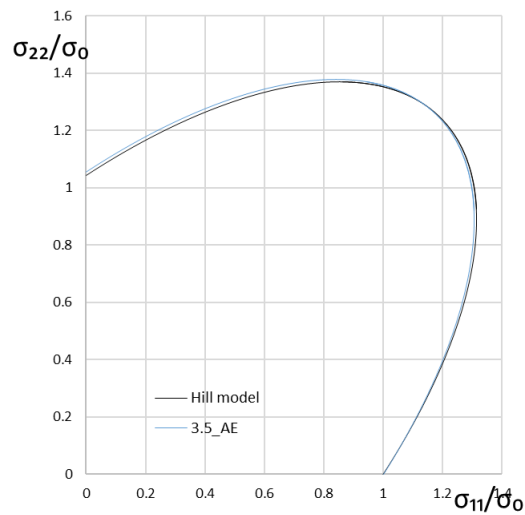


Figure 4.23 – Hill loci for the 3.5 mm radius (AE_2LS)

At the end, a VE has been conducted for the optimal radius, and results are excellent.

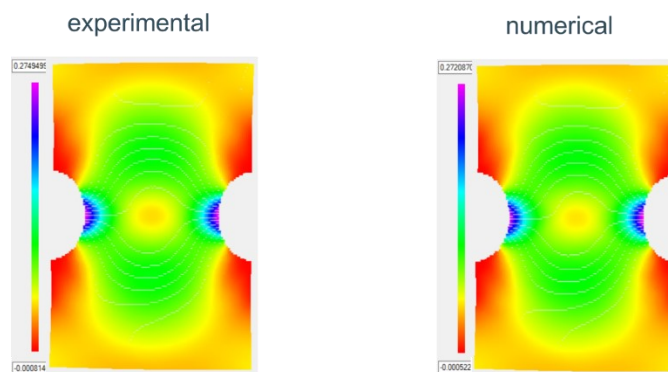


Figure 4.24 - Experimental and numerical strain fields for the 3.5 mm radius (VE)

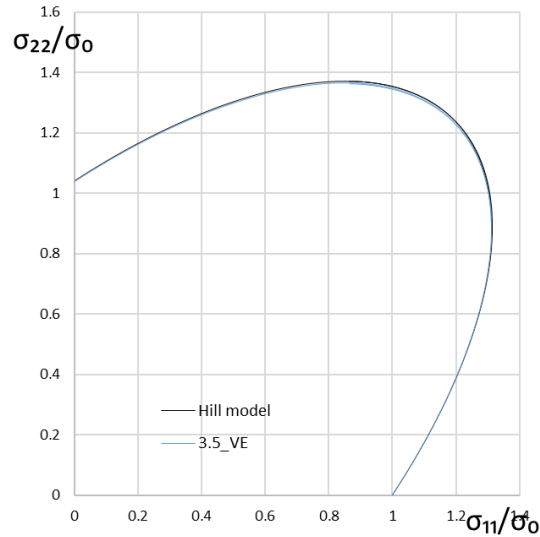
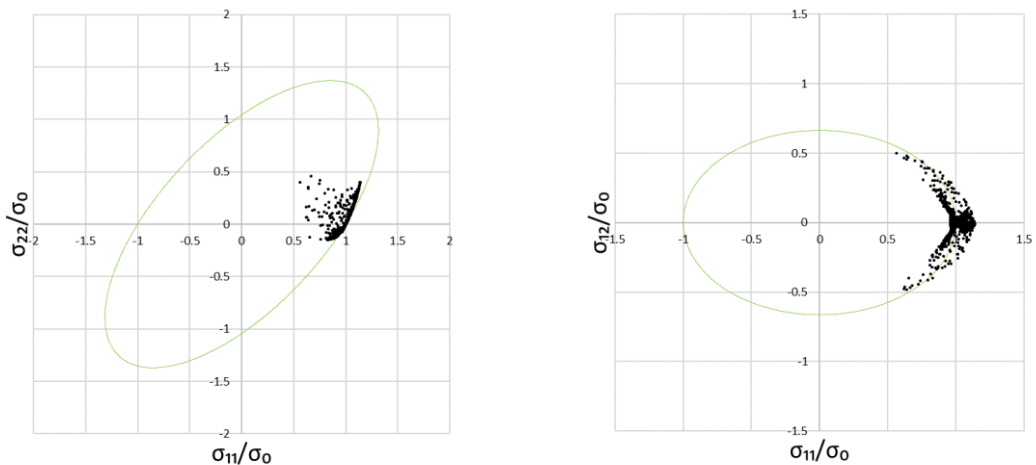


Figure 4.25 - Hill loci for the 3.5 mm radius (VE)

The identifications with the optimal radius prove that this shape is a valid candidate for inverse identification of the material using Hill'48-r for this specific test. Furthermore, again the VE appears to be a valid alternative to the AE.

4.4 Stress states

In this paragraph the stress states for the three radii are shown. The evaluation for the identification has to be done looking at the first plane ($\sigma_{11}/\sigma_0 - \sigma_{22}/\sigma_0$), but the other planes show the values of the σ_{12}/σ_0 , which represents shear stress. The larger is the radius, the larger is the plasticized area.



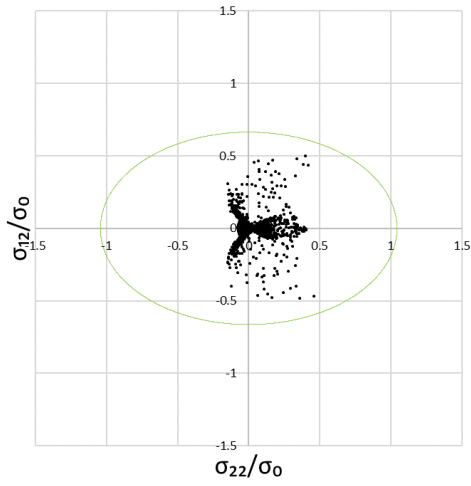


Figure 4.26 – Stress loci for the 1.5 mm radius

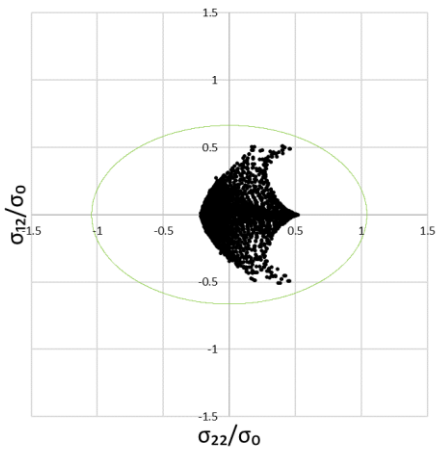
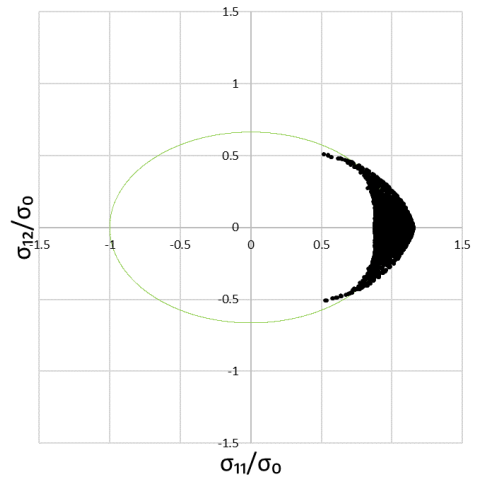
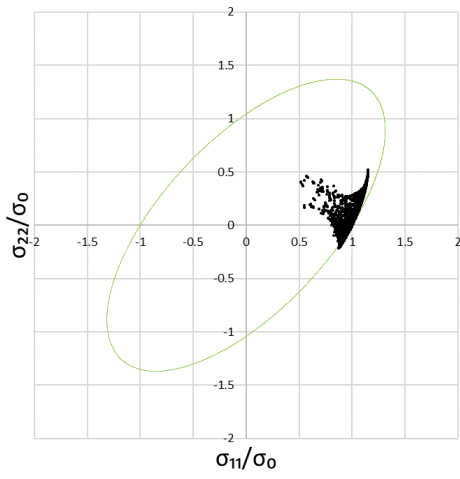


Figure 4.27 - Stress loci for the 3.5 mm radius

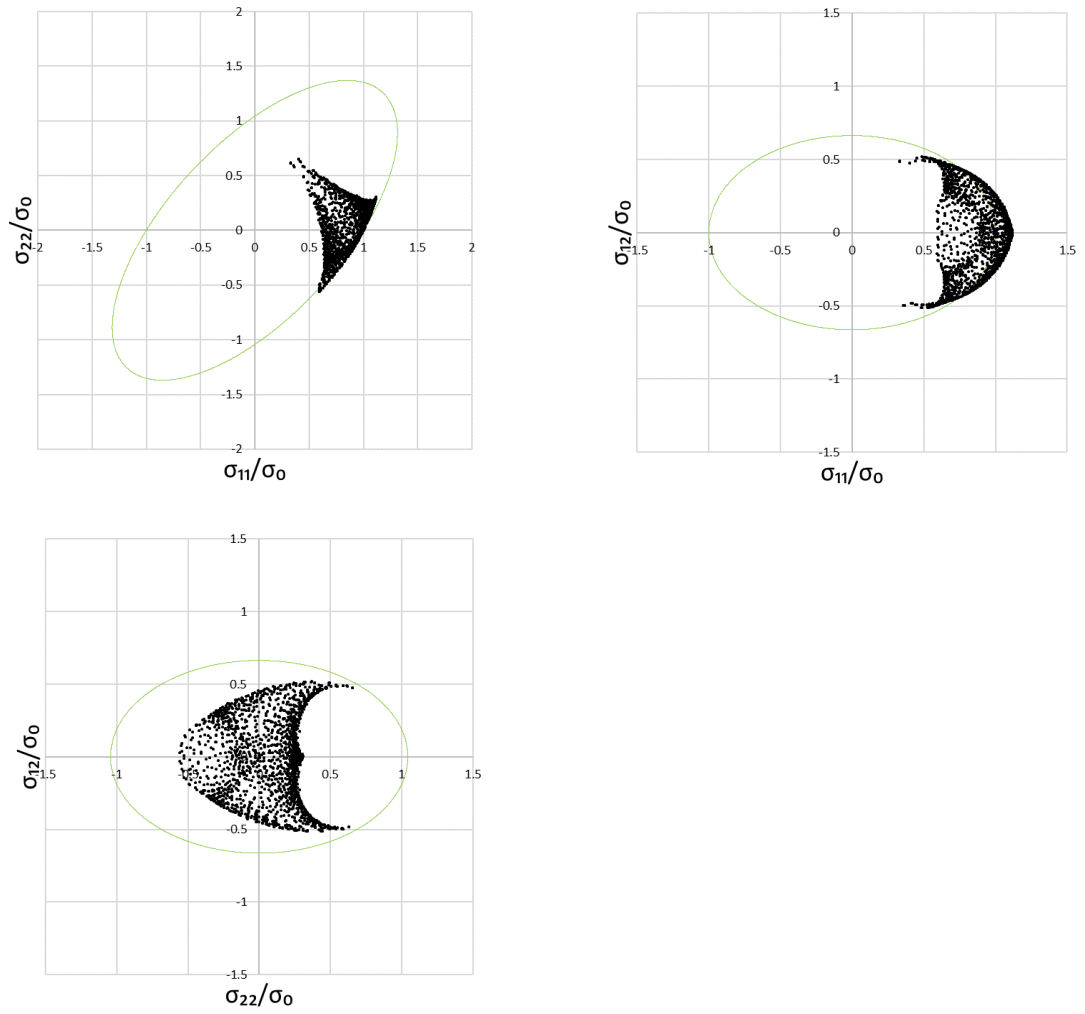


Figure 4.28 - Stress loci for the 7 mm radius

Conclusions

The main objective of this work was to study the possibilities of adopting inverse identification strategies to extract a number of constitutive parameters from a complex experiment leading to heterogeneous strain and stress fields. In fact, it has been observed that large heterogeneity and strain level provide a more complete and reliable material characterization. To this end, an indicator based on the principal strains and defined to rank different mechanical tests was introduced. The indicator was applied to the specimen with the goal of analyzing its trend with respect to the radius of the notches. The parameters formulating the indicator were individually discussed and evaluations regarding strain distributions were made in order to investigate the impact of the radius on strain heterogeneity and strain level.

Final considerations are listed in the following lines:

- The optimal design gives the best identification;
- The identification is sensitive to DIC settings, which depend on the created speckle pattern, and number of load steps;
- There is a consistency between the results from VE and AE, this means the VE is a valid alternative to the AE, meaning less experimental effort;
- Hill'48-r model accurately describes the material behavior in the vicinity of the uniaxial stress state and plane strain state for this specific test.

Based on these results, further studies could be done in the future, conducting tests on specimens with different and more complex shapes.

Bibliography

- [1] Banabic, Dorel. Sheet Metal Forming Processes. Constitutive Modelling and Numerical Simulation. Springer-Verlag, Berlin, Heidelberg 2010.
- [2] S. Cooreman. Identification of the plastic material behaviour through full-field displacement measurements and inverse methods. PhD thesis, Vrije Universiteit Brussel, Belgium, 2008.
- [3] Z. Marciniak, J.L. Duncan, S.J. Hu. Mechanics of Sheet Metal Forming. ButterworthHeinemann, Oxford, 2002.
- [4] R. Hill. A theory of the yielding and plastic flow of anisotropic metals. 1948. Proceedings of the Royal Society London A 193:281-297.
- [5] S. Cooreman. Identification of the plastic material behaviour through full-field displacement measurements and inverse methods. PhD thesis, Vrije Universiteit Brussel, Belgium, 2008.
- [6] S. Coppieters, T. Hakoyama, P. Eyckens, H. Nakano, A. Van Bael, D. Debruyne, T. Kuwabara. On the synergy between physical and virtual metal testing: calibration of anisotropic yield functions using a microstructure-based plasticity model. International Journal of Material Forming. Springer-Verlag France, 2018.
- [7] F. Barlat, J.C. Brem, J.W. Yoon, K. Chung, R.E. Dick, D.J. Lege, F. Pourboghrat, S.H. Choi, E. Chu. Plane stress yield function for aluminum alloy sheets-part I: theory. International Journal of Plasticity. 2003.
- [8] S. Avril, M. Bonnet, A-S. Bretelle, M. Grediac, F. Hild, P. Jenny, F. Latourte, D. Lemosse, S. Pagano, E. Pagnacco. Overview of identification methods of

mechanical parameters based on full-field measurements. *Experimental Mechanics*, Society for Experimental Mechanics, 2008.

[9] D. Kristof. Investigation into the plastic material behaviour up to fracture of thick HSS using multi-DIC and FEMU. PhD thesis, Katholieke Universiteit Leuven, Belgium, 2017.

[10] Simulia. Abaqus/standard, version 6.13.

[11] S. Coppeters, T. Hakoyama, D. Debruyne, S. Takahashi, T. Kuwabara. Inverse yield locus identification of sheet metal using a complex cruciform in biaxial tension and Digital Image Correlation. Proceedings of the 18th International Conference on Experimental Mechanics, Brussels, Belgium, July 1-5 2018.

[12] International Digital Image Correlation Society. A Good Practices Guide for Digital Image Correlation. Jones, E.M.C., Iadicola, M.A. 2018.

[13] D. Lecompte, H. Sol, J. Vantomme, A. Habraken. Analysis of speckle patterns for deformation measurements by digital image correlation. Proceedings of SPIE, vol. 6341, 2006.

[14] C. Niezrecki, P. Avitabile, C. Warren, P. Pingle, M. Helfrick. A Review of Digital Image Correlation Applied to Structural Dynamics. The 9th International Conference on Vibration Measurements by Laser and Noncontact Techniques and Short Course, AIP Conference Proceedings, vol. 1253, pp.219-232, 2010.

[15] J. Chen, G. Jin, L. Meng. Applications of Digital Correlation Method to Structure Inspection. Tsinghua Science and Technology, vol. 12, pp. 237-243, 2007.

[16] P. Reu. Introduction to Digital Image Correlation: Best Practices and Applications. The Art and Application of DIC. February 2012.

[17] <https://www.matchid.eu/>

- [18] G. Musotto. Digital Image Correlation: applicazione di tecniche convenzionali e sviluppo di soluzioni innovative per la stima e l'incremento dell'accuratezza. Master's thesis, Politecnico di Milano, Italy, 2012.
- [19] D. Lecompte. Elastic and Elasto-Plastic Material Parameter Identification by Inverse Modeling of Static Tests Using Digital Image Correlation. PhD thesis, Royal Military Academy & Vrije Universiteit Brussel, Brussels, Belgium, 2007.
- [20] K. Levenberg. A method for the solution of certain non-linear problems in least squares.
Quarterly of Applied Mathematics, vol. 2, pp. 164-168, 1944.
- [21] D. W. Marquardt. An Algorithm for Least-Squares Estimation of Nonlinear Parameters.
Journal of the Society for Industrial and Applied Mathematics, vol. 11, pp. 431-441, 1963.
- [22] A. Andare-Campos, S. Thuillier, P. Pilvin, F. Teixeira-Dias. On the determination of material parameters for internal variable thermoelastic-viscoplastic constitutive models.
International Journal of Plasticity, vol. 23, pp 1349-1379, 2007.
- [23] B. M. Chaparro, S. Thuillier, L. F. Menezes, P. Y. Manach, J. V. Fernandes. Material parameters identification: Gradient-based, genetic and hybrid optimization algorithms.
Computational Materials Science, vol. 44, pp. 339-346, 2008.
- [24] T. Pottier, F. Toussaint, P. Vacher. Contribution of heterogeneous strain field measurements and boundary conditions modelling in inverse identification of material parameters. European Journal of Mechanics - A/Solids, vol. 30, pp. 373-382, 2011.
- [25] M. Teaca, I. Charpentier, M. Martiny, G. Ferron. Identification of sheet metal plastic anisotropy using heterogeneous biaxial tensile tests. International Journal of Mechanical Sciences, vol. 52, pp. 572-580, 2010.

- [26] N. Souto, S. Thuillier, A. Andrade – Campos. Design of an indicator to characterize and classify mechanical tests for sheet metals. *International Journal of Mechanical Sciences*, vol. 101-102, pp. 252-271, 2015.
- [27] M.P. Bendsøe, O. Sigmund (2003). *Topology Optimization: theory, methods and applications*. Springer-Verlag, Berlin, Heidelberg, New York, 2003.
- [28] A. Andrade-Campos, S. Thuillier, N. Souto. Mechanical design of a heterogeneous test for material parameters identification. *International Journal of Material Forming*, vol. 10, pp. 353-367, Springer-Verlag, France, 2016.
- [29] M.P. Bendsøe. *Optimal shape design as a material distribution problem*. Springer, vol.1, pp. 193-202, 1989.
- [30] M. Zhou, G.I.N. Rozvany. The COC algorithm, Part II: Topological, geometrical and generalized shape optimization. *Computer Methods in Applied Mechanics and Engineering*, vol. 89, pp. 309-336, 1991.
- [31] Y.M. Xie, G.P. Steven. A simple evolutionary procedure for structural optimization. *Computers & Structures*, col. 49, pp. 885-896, 1993.
- [32] Y.M. Xie, G.P. Steven. *Evolutionary Structural Optimization*. Springer-Verlag, London, 1997.
- [33] J.A. Sethian, A. Wiegmann. Structural Boundary Design via Level Set and Immersed Interface Methods. *Journal of Computational Physics*, vol. 163, pp. 489-528.
- [34] M.Y. Wang, X. Wang, D. Guo. A level set method for structural topology optimization. *Computer methods in applied mechanics and engineering*, vol. 192, pp. 227-246, 2003.

- [35] S.Y. Wang, K.M. Lim, B.C. Khoo, M.Y. Wang. An extended level set method for shape and topology optimization. *Journal of Computational Physics*, vol. 221, pp. 395-421, 2007.
- [36] G. Allaire, F. Jouve, A.M. Toader. Structural optimization using sensitivity analysis and a level-set method. *Journal of Computational Physics*, vol. 194, pp. 363-393, 2004.
- [37] A. Tovar, N.M. Patel, G.L. Neibur, M. Sen, J.E. Renaud. Topology Optimization Using a Hybrid Cellular Automaton Method With Local Control Rules. *Journal of Mechanical Design*, 2006.
- [38] B. Bourdin, A. Chambolle. Design-dependent loads in topology optimization. *Vol. 9*, pp. 1948, 2003.
- [39] Da DC, Xia Li, Li G & Huang X. Evolutionary topology optimization of continuum structure with Smooth boundary representation. *Structural and Multidisciplinary Optimization* vol. 57, 2143-2159, 2018.
- [40] <https://www.femtools.com/>
- [41] Femtools Optimization User's Guide, version 4.0. Leuven.
- [42] O. Sigmund. A 99 line topology optimization code written in Matlab. *Structural and Multidisciplinary Optimization* vol. 21, 120-127, 1999.
- [43] <https://it.mathworks.com/products/matlab.html>
- [44] A. Khennane. *Introduction to Finite Element Analysis Using Matlab and Abaqus*. CRC Press: Taylor & Francis Group, London, New York, 2013.

[45] T. Nagayasu, S. Takahashi, T. Kuwabara. Development of compact biaxial tensile testing apparatus using conventional compression testing machine and evaluation of the results.

IDDRG 2010.

[46] ISO 16842:2014. Metallic materials – Sheet and Strip - Biaxial tensile testing method using a cruciform test piece, 2014.

[47] A. Marek, F.M. Davis, M. Rossi, F. Pierron. Extension of the sensitivity-based virtual fields to large deformation anisotropic plasticity. International journal of material forming, 2018.

